


REPORT DOCUMENTATION PAGE

Form Approved
OMB No. 0704-0188

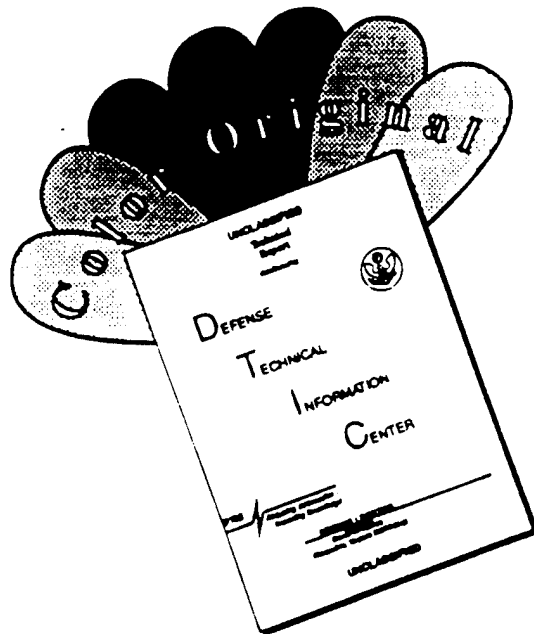
Public reporting burden for this collection of information is estimated to average 1 hour per response, including the time for reviewing instructions, searching existing data sources, gathering and maintaining the data needed, and completing and reviewing the collection of information. Send comments regarding this burden estimate or any other aspect of this collection of information, including suggestions for reducing this burden, to Washington Headquarters Services, Directorate for Information Operations and Reports, 1215 Jefferson Davis Highway, Suite 1204, Arlington, VA 22202-4302, and to the Office of Management and Budget, Paperwork Reduction Project (0704-0188), Washington, DC 20503.

1. AGENCY USE ONLY (Leave blank)		2. REPORT DATE <i>25 Oct 95</i>	3. REPORT TYPE AND DATES COVERED	
4. TITLE AND SUBTITLE <i>Synoptic and Mesoscale Forcing of Convective Activity over Cape Canaveral during Easterly Flow and Nowcasting for Space Shuttle landing at Kennedy Space Center</i>			5. FUNDING NUMBERS	
6. AUTHOR(S) <i>William H. Brauman III</i>				
7. PERFORMING ORGANIZATION NAME(S) AND ADDRESS(ES) AFIT Students Attending: <i>North Carolina University</i>			8. PERFORMING ORGANIZATION REPORT NUMBER <i>95-021D</i>	
9. SPONSORING / MONITORING AGENCY NAME(S) AND ADDRESS(ES) DEPARTMENT OF THE AIR FORCE AFIT/CI 2950 P STREET, BLDG 125 WRIGHT-PATTERSON AFB OH 45433-7765			10. SPONSORING / MONITORING AGENCY REPORT NUMBER	
11. SUPPLEMENTARY NOTES				
12a. DISTRIBUTION / AVAILABILITY STATEMENT Approved for Public Release IAW AFR 190-1 Distribution Unlimited BRIAN D. Gauthier, MSgt, USAF Chief Administration			12b. DISTRIBUTION CODE	
13. ABSTRACT (Maximum 200 words)				
				
14. SUBJECT TERMS			15. NUMBER OF PAGES <i>140</i>	
			16. PRICE CODE	
17. SECURITY CLASSIFICATION OF REPORT	18. SECURITY CLASSIFICATION OF THIS PAGE	19. SECURITY CLASSIFICATION OF ABSTRACT	20. LIMITATION OF ABSTRACT	

19951031 115

DTIC QUALITY INSPECTED 5

DISCLAIMER NOTICE



THIS DOCUMENT IS BEST QUALITY AVAILABLE. THE COPY FURNISHED TO DTIC CONTAINED A SIGNIFICANT NUMBER OF COLOR PAGES WHICH DO NOT REPRODUCE LEGIBLY ON BLACK AND WHITE MICROFICHE.

ABSTRACT

BAUMAN, WILLIAM HENRY III. Synoptic and Mesoscale Forcing of Convective Activity Over Cape Canaveral During Easterly Flow and Nowcasting for Space Shuttle Landings at Kennedy Space Center. (Under the direction of Steven Businger and Allen J. Riordan.)

Space Shuttle landings at Kennedy Space Center are subject to strict weather related landing flight rules. Landing rules demand very accurate nowcasts (short-term forecasts of less than 2 h) of cloud, wind, visibility, precipitation, turbulence, and lightning at the Shuttle launches and landings.

Challenges to U. S. Air Force forecasters at Cape Canaveral Air Station and National Weather Service/Spaceflight Meteorology Group forecasters at Johnson Space Center to nowcast for flight rules are discussed. Application of special meteorological techniques and technologies for supporting Space Shuttle landing operations are examined. Consequences of research for nowcasting convective activity in the Cape Canaveral vicinity are discussed and specifically address landing a Space Shuttle during easterly flow regimes.

During easterly flow regimes, convective activity has been particularly difficult to predict. Four days during the Convection and Precipitation/Electrification (CaPE) Experiment are investigated. Data from CaPE, operational data, satellite imagery, and numerical model analyses are used over the data-sparse region investigated in the research. Elevated moisture in the mid-troposphere above the marine boundary layer

helps distinguish convectively active and passive days. It is shown that the moisture distribution is related to upper tropospheric jet dynamics.

Satellite imagery reveal Rayleigh-Bernard cells in the marine boundary layer on each day. During active days convection is organized into bands whose axes are aligned along the wind shear in the rainband layer, consistent with a buoyancy driven mode of wave-CISK.

The Mesoscale Atmospheric Simulation System (MASS) numerical meteorological model is used to simulate meso- α scale dynamics of an upper tropospheric subtropical jet streak and associated transverse ageostrophic circulations. MASS is further used to simulate the meso- β scale water vapor distribution for application of the model to onshore flow regimes.

Finally, 3-D graphics visualization is addressed as an alternative meteorological interpretation system. The modeled data are displayed as 3-D meteorological fields and compared to conventional analysis methods..

Accession For	
NTIS GRA&I	<input checked="" type="checkbox"/>
DTIC TAB	<input type="checkbox"/>
Unannounced	<input type="checkbox"/>
Justification	
By _____	
Distribution/	
Availability Codes	
Dist	Avail and/or Special
A-1	

**SYNOPTIC AND MESOSCALE FORCING OF CONVECTIVE ACTIVITY
OVER CAPE CANAVERAL DURING EASTERLY FLOW AND NOWCASTING
FOR SPACE SHUTTLE LANDINGS AT KENNEDY SPACE CENTER**

by

WILLIAM H. BAUMAN III

A dissertation submitted to the Graduate Faculty of
North Carolina State University
in partial fulfillment of the
requirements for the Degree of
Doctor of Philosophy

DEPARTMENT OF MARINE, EARTH, AND ATMOSPHERIC SCIENCES

Raleigh

1995

APPROVED BY:

Steve E. Koch

William H. Bauman III

Michael L. Keyser

Steve E. Koch

Co-chair of Advisory Committee

Allen J. Riordan

Co-chair of Advisory Committee

DEDICATION

It would have been impossible to complete this degree program without the support of my family. They had to put up with my long hours away from home while I worked at school only to come home and continue to work until late at night. It has been a tough three years but everyone stood beside me so I could complete my degree.

To my wife, Susanna, you're patience and support has been unbelievable! I relied on you to take care of just about everything...our home, the kids, the bills, our families, the holidays, and more. You're my best friend! I can never thank you enough.

To my buddy Ryan, you're the best son a Dad could have. You've really helped me through this part of our life by letting me work when I had to. But we did have fun together at soccer, T-ball, hockey games, baseball games, and sometimes fishing! Thanks, Ryan, you're a good kid.

To my little one, Hannah, it's probably been hardest on you. You're so young you don't understand why I'm hardly at home. You sometimes made it hard for me to go to work because you would cry and ask me to stay home with you. But we had our special times and Mom was always there for you. You enjoyed going for walks with me through the neighborhood when I came home, liked to ride in "Daddy's car" to the grocery store or gas station, or just play quietly while I worked. You really impressed me when you looked at my committee chairman after my final exam and said "Now I can have my Daddy back." Now you can.

To Mom and Dad - you've been there at every turn to help my family and me. You've instilled a certain something in me that helped me continue to push myself to get done with my work. I'm proud to have parents like you...thank you for all your help.

PERSONAL BIOGRAPHY

Major William H. Bauman III is enrolled in the Ph.D. graduate program in Atmospheric Sciences through the United States Air Force Institute of Technology at North Carolina State University. He is researching methods to develop better forecast techniques during easterly flow regimes for Space Shuttle launches and landings at Kennedy Space Center, FL.

Major Bauman was born October 20, 1959, in Ossining, New York. He earned a Bachelor of Science degree in Meteorology from Lyndon State College, Lyndonville, Vermont in 1981 and in 1989 earned a Master of Science degree in Meteorology from North Carolina State University in Raleigh, North Carolina through the United States Air Force Institute of Technology.

Major Bauman's job assignments include a tour at the Air Force Global Weather Central (AFGWC) at Offutt Air Force Base, NE as Officer-in-Charge (OIC) of the Upper Air Forecast Section, OIC of the European Forecast Section, and then as a staff officer in the Current Operations division. After leaving AFGWC, he was assigned as the OIC of the Wing Weather Officers at Royal Air Force Mildenhall, UK with Detachment 15, 28th Weather Squadron where he developed a dedicated forecast section for SR-71 and RC-135 strategic reconnaissance missions. He then completed a Master of Science degree in Meteorology from North Carolina State University followed by an assignment at Patrick Air Force Base, FL as a Range Staff Meteorologist with the 45th Weather Squadron. Major Bauman provided operational weather support to ballistic missile and space launch activities at Cape Canaveral Air Force Station and to Space Shuttle operations at Kennedy Space Center (KSC) plus provided weather consultant services to the 45th Space Wing (Air Force Space Command) and KSC.

Major Bauman is the recipient of the Air Force Meritorious Service Medal, the Air Force Commendation Medal with one oak leaf cluster, and the Defense Meritorious Service Medal. He was the 2nd Weather Wing junior officer of the year for 1985, received the Air Force Space Command Meriwether Award in 1991, and was awarded the NASA Astronaut Award for excellence in support of manned space flight in 1992.

Major Bauman is married to the former Susanna M. Edgar and they have a son Ryan and daughter Hannah.

ACKNOWLEDGMENTS

First, I must thank the United States Air Force for giving me the opportunity to return to school to complete this degree and to fund my research. Particularly under the Air Weather Service (AWS)/National Center for Atmospheric Research (NCAR) Outreach Partner's Program. The Partner's Program was the key to providing funding for much of the computer hardware and software, data, communications, travel, and graphics support.

I have to extend my thanks to my advisors, Dr. Steven Businger, Dr. Allen Riordan, Dr. Steven Koch, Dr. Sethu Raman, and Dr. Michael Kaplan for their expertise and guidance in the completion of this research.

There are many other people who contributed to the successful completion of this work and they are:

Peggy Bruehl (NWS Office of Meteorology/COMET)
Emanuele Bohm (Marine, Earth & Atmospheric Sciences/NCSU)
Russ Bolton (Computer Sciences Raytheon)
Billie Boyd (45 Weather Squadron/SY)
Barabara Byrd (Physical & Mathematical Sciences/NCSU)
Michele Case (NCAR/Atmospheric Technology Division)
Joey Comeau (NCAR/Scientific Computing Division)
Gary Granger (NCAR/Research Data Program)
John Hagedorn (National Institute of Standards and Technology)
Dennis Joseph (NCAR/Scientific Computing Division)
Vickie Johnson (NCAR /COMET)
Hal Herring (Computer Sciences Raytheon)
Cathy Kessinger (NCAR /Research Applications Program)
Xiofeng Li (Marine, Earth & Atmospheric Sciences/NCSU)
John Madura (NASA/Kennedy Space Center)
John Manobianco (Applied Meteorology Unit/ENSCO)
John McGinley (National Oceanic and Atmospheric Administration/ERL)
Dale Meyer (U. S. Air Force Air Weather Service/XO)
Dick Pritchard (NOAA/Satellite Applications Lab)
Bob Rilling (NCAR/Atmospheric Technology Division)
Amy Rouse (Marine, Earth & Atmospheric Sciences/NCSU)
Joanie Splain (University of Miami)
Jerry Starr (Computer Sciences Raytheon)
Mary Stephenson (North Carolina Supercomputing Center)
Ken Waight (MESO, Inc.)
Sue Walsh (University of Miami)

DRAFT

vi

Gerald Watson (Marine, Earth & Atmospheric Sciences/NCSU)
Mark Wheeler (Applied Meteorology Unit/ENSCO)
Steve Williams (UCAR/Office of Field Project Support)
John Zack (MESO, Inc.)

And the many other people of these organizations:

Advanced Visual Systems
Kubota Graphics Corporation
National Center for Atmospheric Research
National Oceanic and Atmospheric Administration
NASA Goddard Space Flight Center
NASA Johnson Space Center
NASA Kennedy Space Center
North Carolina Supercomputing Center
University Corporation for Atmospheric Research

I must also recognize my colleagues for their support and help with computer software applications, programming, decoding, de-bugging, and just being there through many, many hours of studying, meteorological discussions, Gempakin', Zebin', Gifin', Simmin', classes, exams, Friday pizza, and occasional laughter. These very important people are:

Steve Chiswell
Bob Rozumalski
Tom Graziano
Mike Adams

TABLE OF CONTENTS

	Page
LIST OF TABLES	ix
LIST OF FIGURES	x
1. INTRODUCTION	1
1.1 Background.....	1
1.2 Nowcasting for Space Shuttle Landings.....	5
1.2.1 End-of-Mission Landing.....	8
1.2.2 Return-to-Launch Site Landing and Abort Once Around.....	12
1.3 Special Observing and Modeling Systems	14
1.4 Efforts to Improve Nowcasts During Easterly Flow	17
1.5 Research Objectives.....	18
2. DATA AND ANALYSIS METHODOLOGY.....	21
2.1 Data Sources	21
2.2 Analysis Methodology	21
2.3 Active, Passive, and Suppressed Days.....	24
2.4 Data Analysis.....	28
3. CONVECTIVE INITIATION AND RAINBAND ORGANIZATION	46
3.1 Boundary Layer Convection	46
3.1.1 Symmetric Instability.....	48
3.1.2 Inflection Point Instability	51
3.1.3 Wave-CISK	53
3.2 Static Stability	54
4. NUMERICAL SIMULATIONS.....	60
4.1 Description of the Mesoscale Atmospheric Simulation System	60
4.2 MASS Scheme for Onshore Flow	62
4.3 Course Grid Simulation Configuration	63
4.4 Course Grid Simulation Results	68
4.5 Nested Grid Simulation Configuration	76
4.6 Nested Grid Dynamics	77

	Page
4.7 Nested Grid Moisture Enhancement Sensitivity Studies.....	85
4.7.1 Enhancement with Manually Digitized Radar (MDR)	86
4.7.2 Enhancement with Infrared Satellite Imagery.....	87
4.7.3 Enhancement with Surface Based Observations.....	88
4.7.4 Moisture Enhancement of the NCSU Nest Grid.....	89
4.7.4.1 No Moisture Enhancement - Basic Run.....	90
4.7.4.2 Manually Digitized Radar (MDR) Moisture Enhancement - MDR Run.....	100
4.7.4.3 Infrared Satellite Imagery Moisture Enhancement - Satellite Run.....	105
4.7.4.4 Surface Cloud Observation Moisture Enhancement - Surface Run.....	110
4.7.4.5 MDR, Satellite, and Surface Cloud Observation Moisture Enhancement - Combined Run.....	110
4.8 Model Precipitation Results	117
5. 3-D GRAPHIC VISUALIZATION.....	122
6. SUMMARY AND CONCLUSIONS	129
7. RECOMMENDATIONS AND FUTURE RESEARCH.....	133
8. LIST OF REFERENCES.....	135

LIST OF TABLES

	Page
Table 1.1 Weather flight rules for normal end-of-mission landing at Kennedy Space Center.....	10
Table 1.2 Weather flight rules for return-to-launch-site landing at Kennedy Space Center.....	13
Table 1.3 Weather flight rules for abort-once-around and Primary Landing Site for third revolution landing at Kennedy Space Center.	14
Table 2.1 Vertical levels in the Nested Grid Model (NGM) archive data set and Global Optimum Interpolation (GOI) archive data set.	23
Table 2.2 A timeline of the forecast and observed weather at KSC prepared by U. S. Air Force forecasters for 19-22 July 1991.	26
Table 2.3 A timeline of forecast and observed weather at Melbourne, FL prepared by National Weather Service forecasters for 19-22 July 1991.....	27

LIST OF FIGURES

	Page
Figure 1.1 A depiction of three scenarios considered for landing a Space Shuttle at KSC. A normal end-of-mission landing, return-to-launch-site landing, abort-once-around landing and primary landing sites on third revolution.....	2
Figure 1.2 The Space Shuttle Endeavour makes an early morning launch from Kennedy Space Center, Florida.....	3
Figure 1.3 The Space Shuttle orbiter Discovery lands at the Shuttle Landing Facility, Kennedy Space Center, Florida.	4
Figure 1.4 Depiction of last part of a final orbit and the de-orbit burn maneuver by a Space Shuttle orbiter prior to a landing at Kennedy Space Center, Florida.	9
Figure 1.5 Map of the Cape Canaveral Air Station and Kennedy Space Center vicinity showing locations of special meteorological sensors.	16
Figure 2.1 Map of Florida and the northern Caribbean region showing locations of the hourly surface observing stations and the twice daily rawinsonde release sites. The inset map shows the locations of the special CaPE sensors.	22

	Page
Figure 2.2 Visible satellite imagery (1 km horizontal resolution) from GOES-7 for 19-22 July 1991.....	25
Figure 2.3 Surface analyses for 19-22 July 1991.....	29
Figure 2.4 700 mb analyses for 1200 UTC 19-22 July 1991.....	31
Figure 2.5 As in Fig. 2.4 except for 150 mb.....	32
Figure 2.6 The long-term mean position of the TUTT axis at 200 mb during July.....	33
Figure 2.7 Schematic diagram of an easterly jet streak.....	34
Figure 2.8 Standard skew T-log <i>p</i> diagrams of soundings for Cape Canaveral Air Station for 1015 UTC 20 and 22 July 1991.....	38
Figure 2.9 Time series of relative humidity (RH) computed from Cape Canaveral Air Station soundings from 1016 UTC 19 July 1991 (0615 L) to 0015 UTC 23 July 1991.....	39
Figure 2.10 Vertical cross section from north Florida to near Nassau, Bahamas for 1200 UTC 19-22 July 1991.....	41
Figure 2.11 Water vapor (6.7 μm band) satellite imagery (8 km horizontal resolution) from GOES-7 for 1200 UTC 19-22 July 1991.....	41

	Page
Figure 2.12 Schematic diagram of GPS meteorology.....	44
Figure 2.13 Map of Florida and the Caribbean region showing potential locations of the GPS receivers (X).....	45
Figure 3.1 Plan Position Indicator (PPI) view of reflectivity from the CP-4 Doppler radar for 1405 UTC 20 July 1991. The inset shows the rainband alignment parallel to the wind shear vector ($V_T - V_B$) in the rainband layer.	47
Figure 3.2 Vertical cross sections for 1200 UTC 20 July 1991 of (a) absolute momentum (M) and equivalent potential temperature (θ_e) in °K and (b) relative humidity (RH) and equivalent- potential vorticity (P_{θ_e}).....	50
Figure 3.3 Rotated u and v wind components from the first morning sounding at CCAS.	52
Figure 4.1 The MASS coarse mesh grid covering the southeast United States, western Atlantic Ocean, and Caribbean region with a horizontal grid resolution of 45 km.	64
Figure 4.2 NCSU nest grid covering most of Florida and the Bahama Islands with a horizontal grid resolution of 11 km.	65
Figure 4.3 AMU nest grid covering most of Florida Bahama Islands with a horizontal grid resolution of 11 km.....	66

	Page
Figure 4.4 MASS surface 12 h forecasts from the coarse grid (45 km) for 1200 UTC 19-22 July 1991.....	69
Figure 4.5 MASS 700 mb 12 h forecasts from the coarse grid (45 km) for 1200 UTC 19-22 July 1991.....	70
Figure 4.6 As in Fig. 4.5 except for 150 mb.....	72
Figure 4.7 As in Fig. 4.6 but showing divergence.....	72
Figure 4.8 MASS coarse grid 12 h forecasts of vertical cross sections for 1200 UTC 19 July 1991 and 1200 UTC 20 July 1991.....	75
Figure 4.9 As in Fig. 4.8 except for 1200 UTC 21 July 1991 and 1200 UTC 22 July 1991.....	76
Figure 4.10 MASS nested grid 6 h forecasts of vertical cross sections for 1200 UTC 19 July 1991 and 1200 UTC 20 July 1991.....	79
Figure 4.11 Visible satellite imagery (1 km horizontal resolution) from GOES-7 for 1201 UTC 19 July 1991.....	80
Figure 4.12 As in Fig. 4.11 except for 1200 UTC 20 July 1991.....	81
Figure 4.13 As in Fig. 4.10 except for 1200 UTC 21 July 1991 and 1200 UTC 22 July 1991.....	83

	Page
Figure 4.14 As in Fig. 4.11 except for 1200 UTC 21 July 1991.....	84
Figure 4.15 As in Fig. 4.11 except for 1200 UTC 22 July 1991.....	84
Figure 4.16 Manually Digitized Radar data with 40 km resolution enhanced into MASS NCSU nest run for 0635 UTC 19-22 July 1991.....	92
Figure 4.17 GOES-7 infrared satellite imagery with 4 km resolution enhanced into MASS NCSU nest run for 0600 UTC 19-22 July 1991.....	93
Figure 4.18 Surface cloud observations enhanced into MASS NCSU nest run for 0600 UTC 19-22 July 1991.....	94
Figure 4.19 GOES-7 infrared satellite imagery with 4 km resolution for 1200 UTC 19-22 July 1991.....	95
Figure 4.20 MASS 700 mb 6 h forecasts of relative humidity (RH) from the basic run (no moisture enhancement) of the NCSU nest grid for 1200 UTC 19-22 July 1991.....	98
Figure 4.21 MASS nest grid 6 h forecasts of vertical cross sections from the basic (no moisture enhancement) of the NCSU nest grid for 1200 UTC 19-22 July 1991.....	99
Figure 4.22 As in Fig. 4.20 except for the manually digitized radar (MDR) moisture enhancement of the NCSU nest grid.....	103

	Page
Figure 4.23 As in Fig. 4.21 except for the manually digitized radar (MDR) moisture enhancement of the NCSU nest grid.....	104
Figure 4.24 As in Fig. 4.20 except for the infrared satellite imagery moisture enhancement of the NCSU nest grid.	107
Figure 4.25 As in Fig. 4.21 except for the infrared satellite imagery moisture enhancement of the NCSU nest grid.	109
Figure 4.26 As in Fig. 4.20 except for the infrared satellite imagery moisture enhancement of the NCSU nest grid.	111
Figure 4.27 As in Fig. 4.21 except for the surface cloud observation moisture enhancement of the NCSU nest grid.	112
Figure 4.28 As in Fig. 4.20 except for the surface cloud observation moisture enhancement of the NCSU nest grid.	114
Figure 4.29 As in Fig. 4.21 except for the combined MDR, satellite, and surface cloud observation moisture enhancement of the NCSU nest grid.....	116
Figure 4.30 MASS 3-6 h forecasts of cumulative convective precipitation from the combined moisture enhancement (MDR, satellite, and surface observation data) of the NCSU nest grid for 09-15 UTC 19-22 July 1991.....	120

	Page
Figure 4.31 Plan Position Indicator (PPI) view of the 0.3° elevation angle scan of reflectivity from the CP-4 Doppler radar for (a) 1305 UTC 19 July 1991, (b) 1306 UTC 20 July 1991, (c) 1228 UTC 21 July 1991, and (d) 1257 UTC 22 July 1991.....	121
Figure 5.1 MASS coarse grid 12 h forecast visualized with the Application Visualization System (AVS) for 1200 UTC 20 and 22 July 1991.	124
Figure 5.2 As in Fig. 5.1 except the view is now from a higher angle looking down on the grid domain.....	125
Figure 5.3 MASS nested grid 6 h forecast visualized with the Application Visualization System (AVS) for 1200 UTC 20 and 22 July 1991.	126
Figure 5.4 As in Fig. 5.3 except the view is now from a higher angle looking down on the grid domain.....	128

1. INTRODUCTION

1.1. Background

Many problems can arise that adversely impact launch and landing operations for the Space Shuttle at Kennedy Space Center (KSC). The most common impacts to these operations include weather, ground support equipment failure, launch vehicle failure, payload failure, or not meeting other safety criteria. Nearly 70% of all Space Shuttle countdowns since 1981 were delayed or aborted, with about half of these due to weather (Hazen et al. 1995). Specific weather requirements for a potential emergency landing are the dominant cause of weather related delays to Space Shuttle launches. The focus of this paper is not on weather impacts to launch but instead the forecasts and nowcasts for landing at KSC required for three scenarios. The scenarios considered for landing a Space Shuttle at KSC are: i) normal end-of-mission landing, ii) return-to-launch-site landing and abort-once-around landing, and iii) primary landing sites on the third revolution (3rd rev PLS) (Fig. 1.1).

Space Shuttle launches from KSC (Fig. 1.2) are subject to strict weather related launch commit criteria, but the launch commit criteria will not be considered here since the focus of this research is on landing. Similarly, Space Shuttle landings at KSC's Shuttle Landing Facility (Fig. 1.3) are subject to strict landing weather flight rules. The launch commit criteria and landing weather flight rules were established by the National Aeronautics and Space Administration (NASA). The U. S. Air Force 45th Weather

Squadron at Cape Canaveral Air Station (Cape Canaveral, Florida) and the National Weather Service/Spaceflight Meteorology Group at Johnson Space Center (Houston, Texas) make recommendations regarding landing weather flight rules which have been assessed and modified by NASA during the 14 years of Space Shuttle flight from 1981 to present.

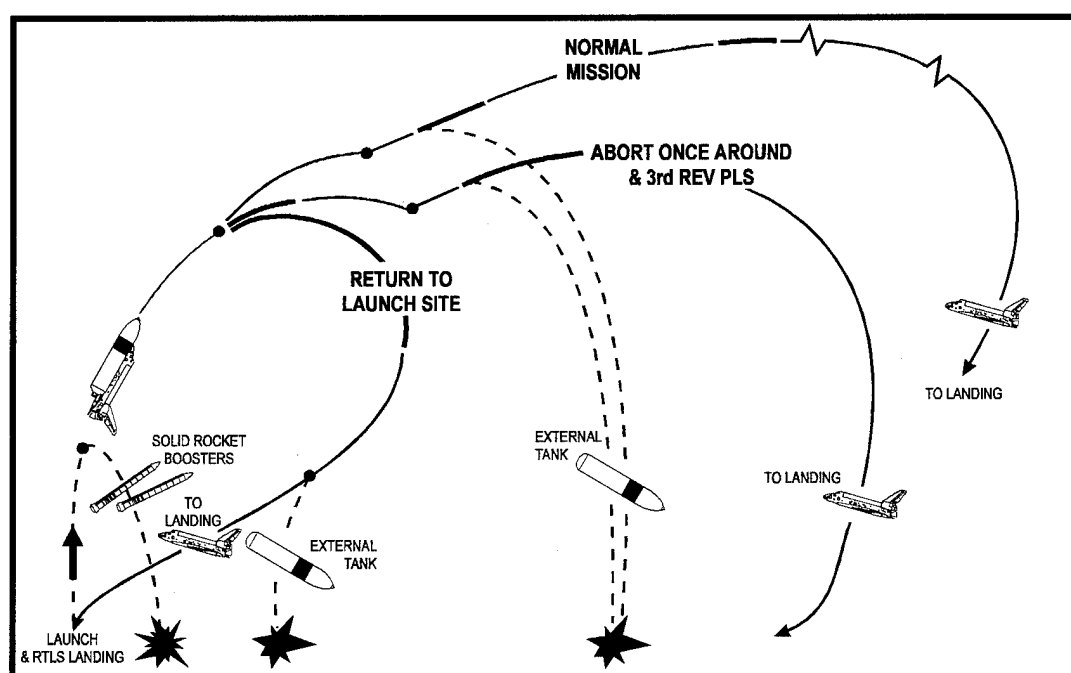


Figure 1.1. A depiction of three scenarios considered for landing a Space Shuttle at KSC. A normal end-of-mission landing, return-to-launch-site landing, abort-once-around landing, and primary landing sites on the third revolution.

Two events have led to re-evaluation and changes in weather-related rules in support of the Space Shuttle program. In 1986, the Space Shuttle Challenger exploded shortly after launch on a day in which surface air temperatures were far colder than during any previous Shuttle launch. It was determined that the exposure to these cold

temperatures contributed to the failure of the O-rings that led to the accident (report of the Presidential Commission of the Space Shuttle Challenger accident 1986). Aerodynamic pressures placed on Challenger from wind shears comparable to the largest previously encountered during launch and from vehicle response maneuvers may have contributed to the final failure of the O-ring seals (report of the Presidential Commission of the Space Shuttle Challenger accident 1986). In 1987, an unmanned Atlas-Centaur vehicle was destroyed by USAF Range Safety because of guidance system failure after the vehicle triggered a four-stroke lightning flash to ground 48 seconds after launch from Cape Canaveral Air Station during convectively active conditions.

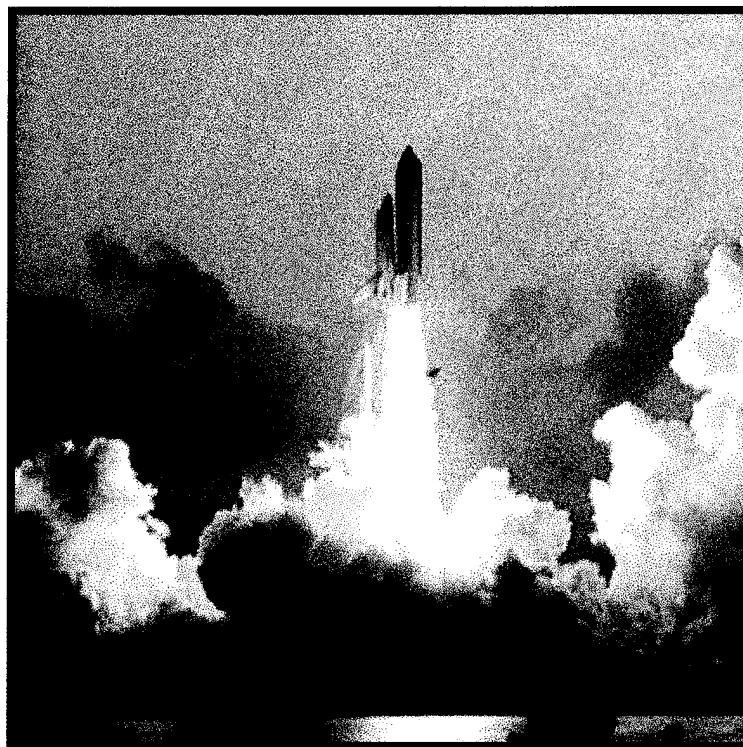


Figure 1.2. The Space Shuttle Endeavour makes an early morning launch from Kennedy Space Center, Florida.



Figure 1.3. The Space Shuttle orbiter Discovery lands at the Shuttle Landing Facility, Kennedy Space Center, Florida.

Findings from the House Committee Report on the Challenger Accident stated: *“Weather, by far, is the most significant factor governing operational decisions, orbiter damage, and landing safety. Ultra-conservative rules prevail because of the predictable unpredictability of Cape weather.”* (National Research Council 1988). One of the recommendations from the House Committee Report on the Challenger Accident was to: *“...invent new technology and techniques to learn new ways to understand the*

dynamics of Cape Kennedy weather phenomena to supplant current inadequacy to forecast two hours ahead." (National Research Council 1988).

The weather flight rules include constraints as shown in Tables 1.1, 1.2, and 1.3. A full discussion of the specifics and origin of the flight rules is beyond the scope of this research. Instead a general overview will be given, and attention will mainly focus on the nowcast problem.

1.2. Nowcasting for Space Shuttle Landings

The focus of the short term forecast problem at KSC is the impact of weather conditions at the Shuttle Landing Facility on a normal end-of-mission landing and three possible intact aborts (return-to-launch-site, abort-once-around, or 3rd Rev PLS) (Fig. 1.1). A fourth intact abort scenario, called transoceanic abort landing (TAL), can occur at one of the contingency landing sites in North Africa or Spain (this option is not considered further in this research). Unfavorable weather conditions for return to launch site and abort-once-around dominate the weather considerations for Space Shuttle launches (Hazen et al. 1995). Therefore, improvement in the KSC forecast has the potential to reduce the weather impact on Space Shuttle launches.

Both modeling and observational studies have concluded that the patterns and locations of Florida convection are directly related to the synoptic wind field (Byers and Rodebush 1948; Estoque 1962; Frank et al. 1967; Neumann 1971; Pielke 1974; Boybeyi and Raman 1992). These studies demonstrate the importance of the interaction between

the synoptic wind and the sea-breeze circulation in determining the timing and locations of convective activity across the Florida peninsula. The sea-breeze circulation and the normal patterns of Florida convection assume different characteristics depending on whether the prevailing low-level flow has an onshore, offshore, or alongshore component.

There are two basic large-scale convection-producing flow regimes over the Florida peninsula that must be considered when discussing a KSC forecast for Space Shuttle landings. Onshore (easterly) flow regimes along the Atlantic coast typically generate less vigorous convection than offshore (westerly) flow regimes (Foote 1991). Convection triggered during onshore flow is characterized by small vertical towers that most often form in the morning and produce brief showers. These showers account for fewer than 5% of the total lightning flashes in this area (Blanchard and López 1985). Onshore convection also affects ceilings, visibility, surface wind, and turbulence limits for landing.

The modeling and observational studies also show that eastern Florida generally receives rainfall earlier on days with easterly flow than on days with westerly flow. Afternoon convection at KSC due to prevailing westerly flow is more predictable than morning convection. The convection tends to move with a fairly regular motion from west to east. Locations and movement of the sea breeze fronts associated with this convection can normally be detected and monitored with Doppler radar and high resolution visible satellite imagery (Wakimoto et al. 1993). Onshore flow convection, on

the other hand, is not necessarily associated with the sea breeze front nor an overnight land breeze front (Reap 1994). The convection occurring within the prevailing deep easterly flow has been difficult to detect with satellite imagery since it is a pre-dawn phenomena and generally consists of low (warm) cloud tops, which are difficult to distinguish from background surface temperatures. Enhancement curves for infrared satellite imagery have been developed by NWS/SMG and the Applied Meteorology Unit at CCAS which have helped locate early morning convective showers. The recent deployment of the improved Geostationary Operational Environmental Satellite (GOES-8) has also helped this problem somewhat. Radar is a useful tool to monitor convection development and movement, but showers located offshore and moving towards KSC will sometimes weaken and dissipate before landfall leaving conditions safe for a Shuttle landing.

During onshore flow, clouds and precipitation may form if low level convergence and upward vertical motion are present in the morning along the east coast of Florida. However, the weather can range from widespread thunderstorms to no precipitation at all. Easterly flow regimes clearly present a special forecast challenge for Space Shuttle landing scenarios, and it is important to try to understand why convection occurs at KSC on some mornings and not on other mornings during onshore flow. A small shoreward-moving shower or thunderstorm presents a distinct hazard to an orbiter trying to land at the Shuttle Landing Facility when considering the weather flight rules as shown in Tables 1.1, 1.2, and 1.3. Safely landing an orbiter can depend on the

accuracy of the forecast, which must determine whether or not convection will be present, absent, develop over the water and move onshore, dissipate, or intensify.

In addition to safety issues, other concerns such as a 1-orbit delay to land at KSC, 24 hour delay to land KSC, or simply unacceptable weather at KSC may result in a decision to land the orbiter at Edwards Air Force Base (California) instead of at KSC. This can be a costly decision because a 24 hour landing delay costs about \$90,000 in man-hours at Johnson Space Center while an Edwards Air Force Base landing costs the Space Shuttle program about \$600,000 followed by a \$440,000 "ferry flight" of the orbiter from Edwards Air Force Base to KSC. None of these costs are incurred for an on-time landing at KSC.

1.2.1. End-Of-Mission Landing

A final go/no-go decision is made for an end-of-mission landing based on a forecast issued 90 minutes prior to landing. The end-of-mission landing occurs 60 minutes after the orbiter performs a "*de-orbit burn*" maneuver. The de-orbit burn maneuver moves the orbiter from its on-orbit spacecraft configuration into an aircraft configuration to re-enter the Earth's atmosphere and glide to a landing (Fig. 1.4).

Once the burn has occurred, the orbiter is constrained to continue on its planned trajectory to a landing at the Shuttle Landing Facility - there is no turning back. Thus an accurate forecast is critical for a safe landing. The weather flight rules for the orbiter during an end-of-mission landing are strict relative to most other aircraft, and observed

and forecast conditions for end-of-mission landing time must meet or exceed those shown in Table 1.1. If the landing weather is observed or forecast to be worse than these criteria the landing is postponed or the landing location is changed.

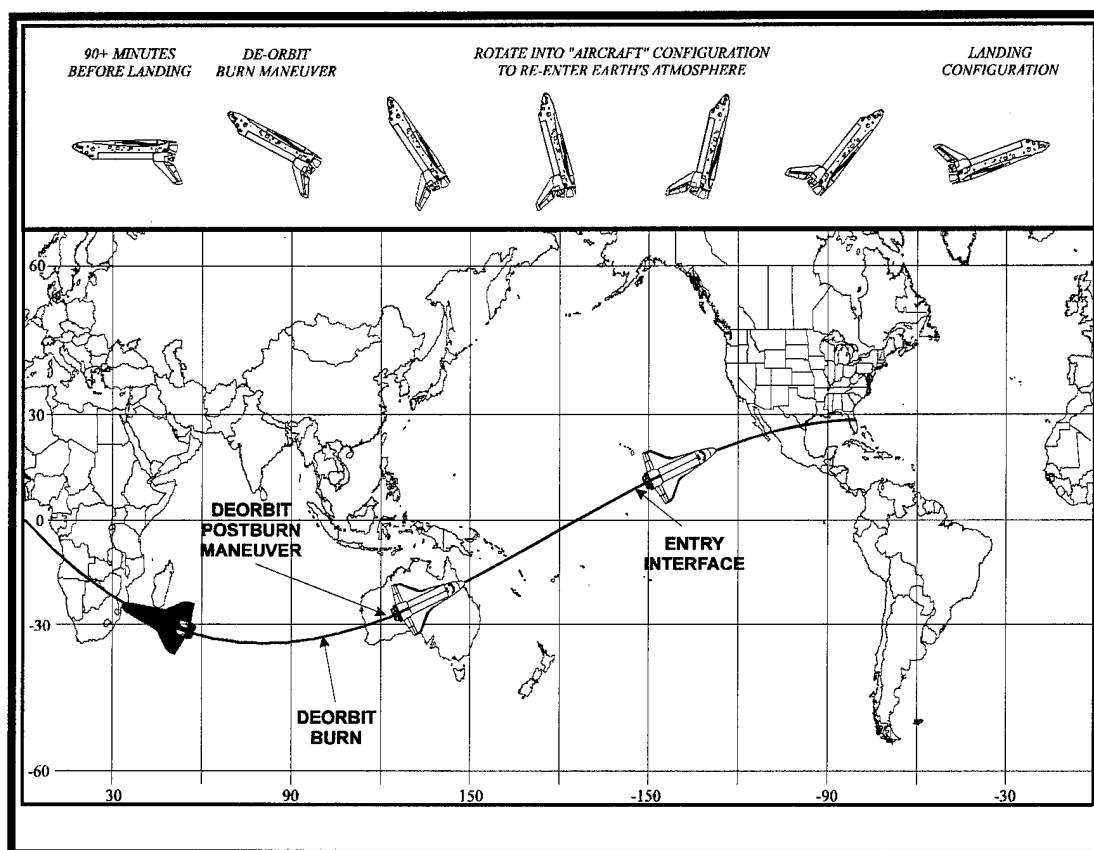


Figure 1.4. Depiction of last part of a final orbit and the de-orbit burn maneuver by a Space Shuttle orbiter prior to a landing at Kennedy Space Center, Florida.

For a normal end-of-mission, the ceiling must be greater than 10,000 ft since the orbiter can only fly in conditions better than standard visual flight rules (VFR) and is a

consideration for slant-range visibility Any type of mid- or low-level cloud produced by large-scale weather systems, even small tropical showers, can affect this flight rule.

Table 1. 1. Weather flight rules for normal end-of-mission landing at Kennedy Space Center (after Space Shuttle Operational Flight Rules, 1995).

CRITERIA	WEATHER LIMITS
CEILING	≥ 10000 FT
OBS CLDS BELOW 10000 FT	≤ 0.2
VISIBILITY	≥ 5 SM
PEAK CROSS WIND	≤ 15 KT DAY, ≤ 12 NIGHT
PEAK HEAD WIND	≤ 25 KT
AVG TAIL WIND	≤ 10 KT
PEAK TAIL WIND	≤ 15 KT
GUST	≤ 10 KT
TURBULENCE	\leq MODERATE
TSTM, PRECIP, LIGHTNING	> 30 NMI
DETACHED OPAQUE ANVIL < 3 HRS OLD	> 20 NMI

Peak cross winds of less than 12 kt (at night) and 15 kt (during day) are the limits placed on a normal landing based on orbiter design. Phenomena that generate surface wind changes which forecasters must consider in their landing forecast include synoptic scale fronts, sea breeze fronts, thunderstorm outflows, and diurnal processes. Generally the smaller the scale of the phenomenon, the more difficult it is to observe and forecast. This effect places greater emphasis on techniques to track and forecast common Florida, mesoscale phenomena that are capable of producing surface winds in excess of orbiter landing limits.

The visibility flight rule, greater than 5 statute miles, simply allows the orbiter pilot to see the runway for landing (better than VFR applies here also). Morning fog, frequently caused by a weak land breeze, is a common occurrence at the Shuttle Landing Facility and can quickly advect (< 2 hr) over KSC from the west where fog forms above wetlands.

The "no precipitation" rule is required for a number of reasons including, pilot visibility, wet (slippery) runway, damage to the orbiter tiles, and the possibility of natural or triggered lightning. Precipitation, thunderstorms, and lightning must be greater than 30 nmi from the Shuttle Landing Facility. The orbiter's flight path must have a 10 nmi horizontal clearance of lightning and 2 nmi vertical clearance of lightning. Lightning from anvil cloud less than 3 hr old is also a potential threat to the orbiter and detached opaque anvil must be greater than 20 nmi from the orbiter's flight path. Although all Space Shuttle orbiters have had extensive upgrades to decrease the stopping distance upon landing (better tires, brakes, nose wheel steering gear, and an added drag chute) the runway must be dry for a safe end-of-mission landing. Also, any precipitation striking the protective heat absorbing tiles can damage them. At normal landing speeds, even light precipitation can pit the tiles making them unusable for future flights, requiring expensive and time consuming tile repair or replacement work. The most difficult precipitation to forecast occurs from small showers and thunderstorms that can develop well within the 90 minute landing forecast period. Thus forecasters

must carefully track the development and movement of clouds, areas of low-level convergence, sea breezes, and changes in thermodynamic stabilities.

1.2.2. Return-To-Launch-Site Landing and Abort Once Around Landing

The mode of abort is normally determined by the Mission Control Center at Johnson Space Center, Houston based on the type and time of a failure. The return-to-launch-site is the quickest option and permits the orbiter to land 25 minutes after launch (Fig. 1.1). During a return-to-launch-site landing, the orbiter jettisons its solid rocket boosters and the external liquid fuel tank, flies downrange to dissipate propellant, and performs critical maneuvers under power to attain a flight path directly for KSC to land at the Shuttle Landing Facility (National Space Transportation System News reference Manual 1988). An abort-once-around allows the orbiter to fly once around the Earth then make a normal entry and landing at the Shuttle Landing Facility, Edwards Air Force Base (California), or White Sands Space Harbor (New Mexico). The abort-once-around requires ~ 90 minutes.

Shuttle Landing Facility weather conditions for return-to-launch-site (Table 1.2), abort-once-around and 3rd rev PLS (Table 1.3) are generally not as strict as the normal end-of-mission conditions. Should any of these landing weather limits be violated the launch is postponed. The ceiling rule is relaxed and allows for ceilings as low as 5,000 ft for return-to-launch-site and 8,000 ft for abort-once-around and 3rd rev PLS (instead of 10,000 ft) and the cross wind limit is 15 kt day and night for return-to-launch-site but

remains 12 kt at night for abort-once-around and 3rd Rev PLS. The limits for thunderstorms, precipitation, lightening, and anvil cloud is only reduced for return-to-launch-site as shown in Table 1.3. The weather phenomena producing these conditions is the same as for the normal end-of-mission flight rules.

It is obvious that end-of-mission, return-to-launch-site, abort-once-around, and 3rd rev PLS weather criteria demand very accurate short term forecasts of cloud, wind, visibility, precipitation, and lightning at the Shuttle Landing Facility prior to Space Shuttle launches and landings. Frequent development and dissipation of convective showers and thunderstorms, and the mesoscale impact of Cape Canaveral's geography, present a forecast challenge. A strategy to improve the short term forecasting capability at KSC has been to supplement the observing systems in the Florida region, especially in the close vicinity of KSC, to provide better mesoscale observations.

Table 1.2. Weather flight rules for return-to-launch-site landing at Kennedy Space Center (after Space Shuttle Operational Flight Rules, 1995).

CRITERIA	WEATHER LIMITS
CEILING	≥ 8000 FT
VISIBILITY	≥ 5 SM
PEAK CROSS WIND	≤ 15 KT DAY, ≤ 12 KT NIGHT
PEAK HEAD WIND	≤ 25 KT
AVG TAIL WIND	≤ 10 KT
PEAK TAIL WIND	≤ 15 KT
GUST	≤ 10 KT
TURBULENCE	≤ MODERATE
TSTM, PRECIP, LIGHTNING	> 30 NMI
DETACHED OPAQUE ANVIL < 3 HRS OLD	> 20 NMI

Table 1.3. Weather flight rules for abort-once-around and Primary Landing Site for the third revolution landing at Kennedy Space Center (after Space Shuttle Operational Flight Rules, 1995).

CRITERIA	WEATHER LIMITS
CEILING	≥ 5000 FT
VISIBILITY	≥ 4 SM
PEAK CROSS WIND	≤ 15 KT DAY & NIGHT
PEAK HEAD WIND	≤ 25 KT
AVG TAIL WIND	≤ 10 KT
PEAK TAIL WIND	≤ 15 KT
GUST	≤ 10 KT
TURBULENCE	\leq MODERATE
TSTM, PRECIP, LIGHTNING	> 20 NMI
DETACHED OPAQUE ANVIL < 3 HRS OLD	> 15 NMI

1.3. Special Observing and Modeling Systems

Data available for forecasting at KSC are derived from conventional surface observations, upper air observations, one buoy about 65 km southeast of KSC and another about 230 km east-northeast of KSC, weather radar, and satellite imagery. In addition to the conventional observational systems, forecasters have special in situ and remote sensors in the vicinity of KSC and Cape Canaveral Air Station (CCAS) to provide improved observation of mesoscale circulations and lightning activity in the vicinity of KSC. The special sensors (Fig. 5) include the KSC/CCAS wind tower mesonet (winds, temperatures, and dew points), cloud-to-ground lightning detection

(LDS) system, inter- and intra-cloud lightning detection and ranging (LDAR) system, ground-based electric field mill (GBFM) network, a 50 Mhz wind profiling radar, and 915 Mhz boundary layer profiling radars. The Doppler weather radar (WSR-88D) is located at the NWS in Melbourne.

Also available is a real-time display of the National Lightning Detection Network, direct readout and display of polar orbiter satellite imagery, and rawinsondes and Jimspheres released at CCAS as requested by the forecasters. The main meteorological data analysis and display system at CCAS and JSC is the Meteorological Interactive Data Display System (MIDDS) which is a McIDAS-based system integrated into the Range Weather Operations Facility's observing and data display systems.

Forecasting for Space Shuttle operations is a joint effort between the 45 WS meteorologists at CCAS and the NWS/SMG meteorologists at JSC. The 45 WS meteorologists at CCAS are responsible for all forecasts until the Space Shuttle launches. The NWS/SMG meteorologists are responsible for all on-orbit and landing forecasts. Although U. S. Air Force and National Weather Service meteorologists are geographically separated and have different responsibilities and customers, they must coordinate extensively to ensure forecast consistency from pre-launch operations through launch and landing with respect to weather at KSC. Meteorologists at both locations have direct access to KSC and CCAS area meteorological data and observing systems via MIDDS and the WSR-88D Doppler radar Principal User Processor.

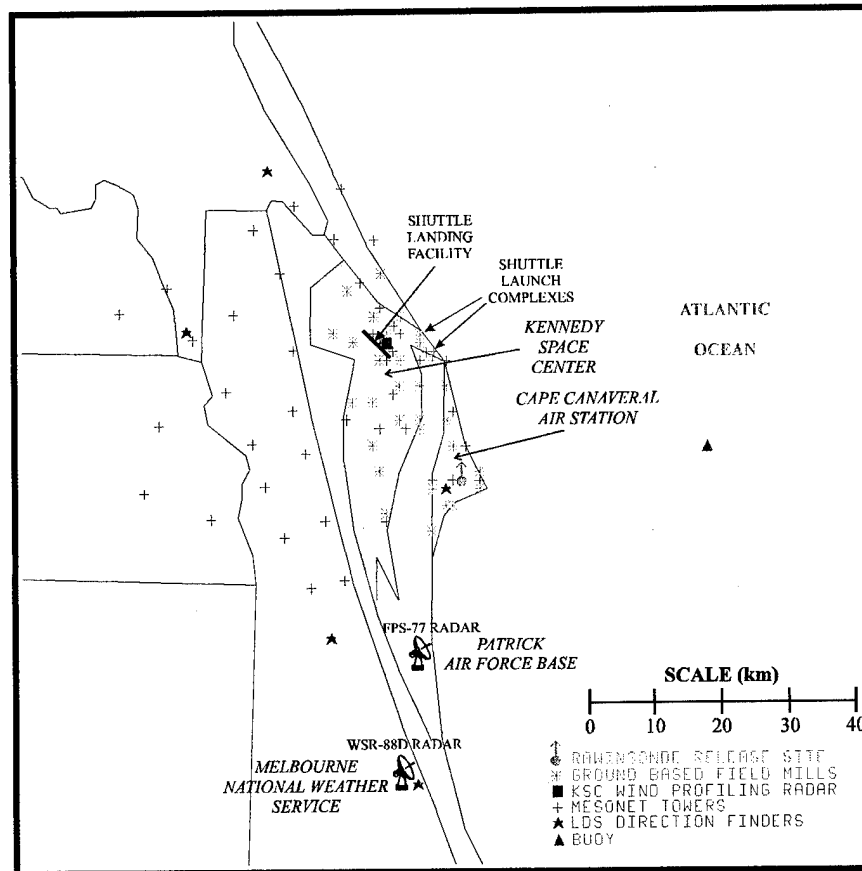


Figure 1.5. Map of the Cape Canaveral Air Station and Kennedy Space Center vicinity showing locations of special meteorological sensors.

Even with all the conventional and special observing and data display systems available to the U. S. Air Force and National Weather Service meteorologists, new technology and systems are continually being developed to improve the forecast for Space Shuttle support. In an effort improve technology transition and develop forecast techniques for the meteorologists, NASA, the U. S. Air Force, and National Weather Service developed the Applied Meteorology Unit in 1991. The Applied Meteorology Unit is co-located with Range Weather Operations at CCAS and supports the 45th

Weather Squadron, Spaceflight Meteorology Group, and National Weather Service Forecast Office (Melbourne, Florida). The Applied Meteorology Unit is managed by one NASA Chief and is staffed by five contractor personnel consisting of meteorologists and computer scientists. The Applied Meteorology Unit is responsible for evaluating, developing, and transitioning new technologies, techniques, and systems into operations to support the National Space Program.

One of the Applied Meteorology Unit's current tasks is to evaluate mesoscale models for operational use by the U. S. Air Force and National Weather Service meteorologists. The Mesoscale Atmospheric Simulation System (MASS) model is currently being run on a daily basis in real-time by the Applied Meteorology Unit, using a fine mesh grid over the Florida Peninsula which has a horizontal resolution of 11 km with 22 vertical levels. The version of MASS being evaluated and run was developed by MESO, Inc. (Kaplan et al. 1982 and Manobianco et al. 1994) and initially delivered to the Applied Meteorology Unit in March 1993. In April 1995 selected MASS model output was made available to operational meteorologists on a limited basis to evaluate the ability of MASS to predict convective initiation in support of space launch activity.

1.4. Efforts to Improve Nowcasts During Easterly Flow

Meteorologists supporting Space Shuttle operations have noted that the onset of convective activity during onshore flow is especially difficult to predict. Seemingly similar synoptic environments are present in cases that produce conditions ranging from

clear skies to heavy showers. Conditions can change from safe to hazardous within short periods (<1 hour).

A cooperative effort between the authors of this research, U. S. Air Force (45 WS), National Weather Service (Spaceflight Meteorology Group), and the Applied Meteorology Unit is currently underway to improve nowcasts for Space Shuttle landings at KSC during onshore flow. The research uses the enhanced data sets available from the Convection and Precipitation/Electrification (CaPE) Experiment (Gray 1991) to analyze and compare four days of onshore flow during which similar synoptic conditions resulted in contrasting weather in the vicinity of KSC.

The MASS model with enhanced horizontal grid resolution is being used to capture small convective features present in onshore flow regimes that cannot be resolved by current operational numerical models. Assimilation of satellite, weather radar data, and surface-based cloud observations into the MASS model is being investigated to help overcome the general lack of in situ data over the water east of Florida. Finally, 3-D visualization techniques are being examined and applied to analysis and model output to help forecasters view the data more efficiently than conventional methods. Results from these investigations will be presented in subsequent chapters.

1.5. Research Objectives

The primary objective of this research is to improve the lead time and accuracy of forecasting the onset of convective activity at KSC during onshore flow regimes. It is

therefore prudent to examine possible convection initiation and convection suppression processes to meet this primary operational objective.

i) Determine the effects of large scale forcings (meso- α and synoptic) and their role supporting convective initiation.

a) Sub-tropical jet stream dynamics

b) Interaction and proximity of the tropical upper-tropospheric trough (TUTT)

ii) Investigate physical mechanisms for mesoscale initiation and organization of rainbands.

a) Rayleigh-Bernard instability.

b) Static stability in the pre-convective environment.

c) Inertial instability.

d) Conditional symmetric instability (CSI).

e) Inflection point instability (IPI).

f) Wave-convective instability of the second kind (wave-CISK).

iii) Use the Mesoscale Atmospheric Simulation System (MASS) model to:

a) Simulate the large-scale jet streak dynamics with a “coarse mesh” (45 km) mesoscale horizontal resolution.

b) Simulate the mesoscale processes and precipitation distribution with a “fine mesh” (11 km) mesoscale horizontal resolution nested within the coarse mass domain.

c) Conduct sensitivity studies of the effects of assimilation of different moisture sources into the fine mesh domain.

iv) Use 3-D visualization techniques to interpret meteorological parameters.

2. DATA AND ANALYSIS METHODOLOGY

2.1. Data Sources

The research presented here focuses on a series of days with easterly flow during the field phase of the Convection and Precipitation/Electrification (CaPE) Experiment. CaPE was a major field program conducted in central Florida from 8 July 1991 to 18 August 1991 (Foote 1991). CaPE investigations concentrated on the area encompassing KSC and Cape Canaveral Air Station (CCAS) in part to study weather impacts to the National Space Program. The CaPE field program resources included eight instrumented research aircraft, four Doppler radars, forty seven Portable Automated Mesonet (PAM) surface stations, and six Cross-chain Loran Atmospheric Sounding Systems (CLASS) (Fig. 2.1). The CaPE data set was complimented by the KSC/CCAS observational network (wind tower mesonet, ground-based electric field mill network, and the lightning detection systems; see Fig. 1.5), and routinely available operational data (hourly surface observations, twice daily rawinsondes, buoys, ships of opportunity and satellite data).

2.2 Analysis Methodology

Easterly flow generally prevails across the Florida peninsula in the summer when the Bermuda high ridge-axis lies through central and northern Florida (Pielke 1975). However, during CaPE the prevailing flow was westerly, with only nine days classified

as easterly. Of these nine days, four, 19-22 July 1991, were contiguous with good observational coverage and are the focus of this research.

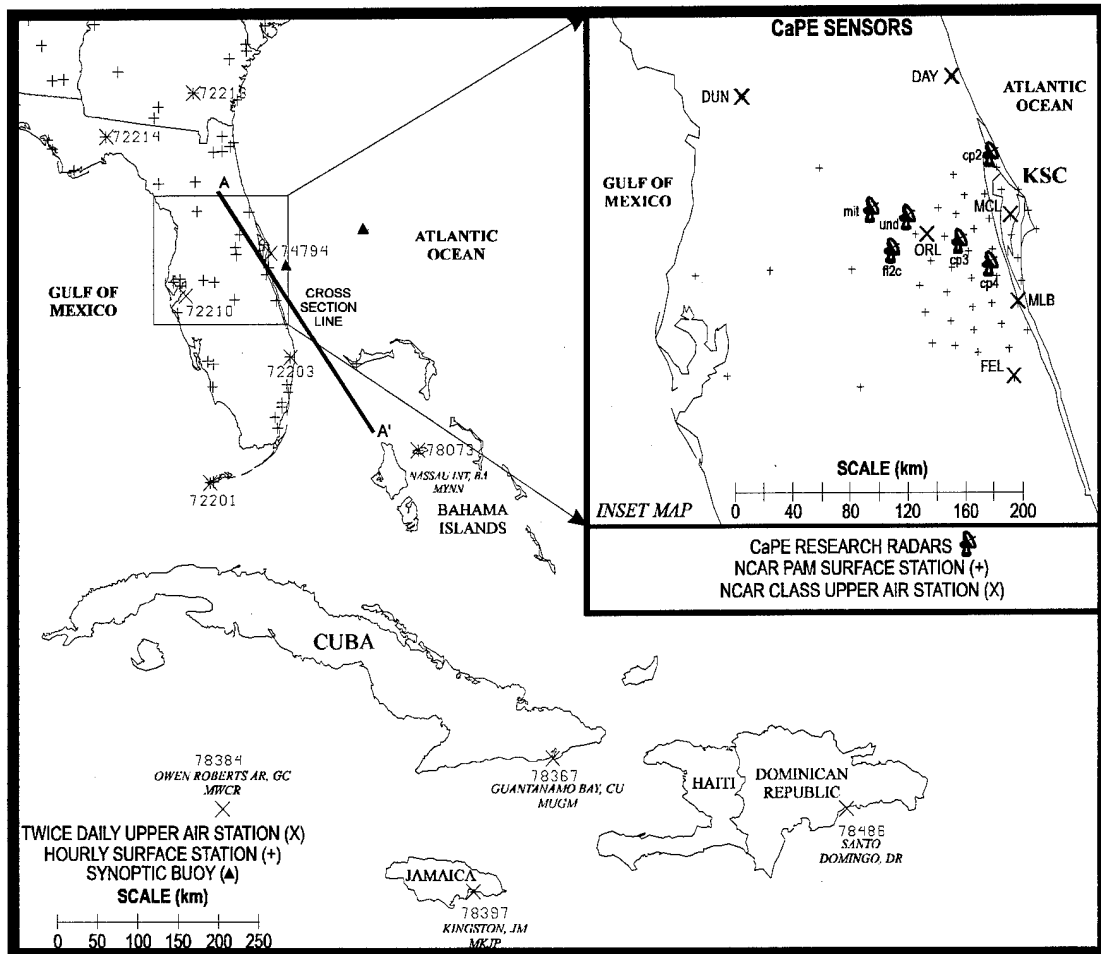


Figure 2. 1. Map of Florida and the northern Caribbean region showing locations of the hourly surface observing stations (+) and the twice daily rawinsonde release sites (X). The line labeled A to A' extending from north Florida to the Bahama Islands denotes the axis for vertical cross sections shown in section 2 of this document. The inset map shows the locations of the special CaPE sensors: the Portable Automated Mesonet (PAM) surface observing systems (+) and the Cross-chain Loran Atmospheric Sounding System (CLASS) release sites (X).

The only conventional data over water during the period of investigation were from occasional ships of opportunity and two buoys (Fig. 2.1) which reported every three hours at synoptic times. Over water analyses were constructed by merging actual rawinsonde data with "synthetic" soundings derived from the National Meteorological Center (NMC) Nested Grid Model (NGM) analyses (NOAA, 1985). The NMC Global Optimum Interpolation (GOI) spectral analysis was used as a "first guess" field for the merged rawinsonde and NGM sounding data (Table 2.1).

Table 2.1. Vertical levels in the Nested Grid Model (NGM) archive data set and Global Optimum Interpolation (GOI) archive data set. NGM archived fields include geopotential height (Φ), temperature (T), relative humidity (RH), and u and v components. GOI archived fields include mean sea level pressure (MSLP), temperature (T), and sea surface temperature (SST) at the surface and geopotential height (Φ), temperature (T), and u and v components of wind at all other levels. The GOI archived fields also include relative humidity (RH) from the surface through 300 mb.

PRESSURE LEVEL (mb)	NGM ARCHIVE GRID	GOI ARCHIVE GRID
Surface		MSLP, T, SST
1000	Φ , T, RH, u , v	Φ , T, RH, u , v
950	Φ , T, RH, u , v	
900	Φ , T, RH, u , v	
850	Φ , T, RH, u , v	Φ , T, RH, u , v
800	Φ , T, RH, u , v	
750	Φ , T, RH, u , v	
700	Φ , T, RH, u , v	Φ , T, RH, u , v
500	Φ , T, RH, u , v	Φ , T, RH, u , v
300	Φ , T, RH, u , v	Φ , T, RH, u , v
250		Φ , T, u , v
200		Φ , T, u , v
150		Φ , T, u , v

The General Meteorological Package (GEMPAK) (desJardins et al. 1992) was then used to create a sounding at each NGM and GOI grid point. The NGM soundings were merged with actual CLASS, National Weather Service, and USAF rawinsondes. The GOI sounding analyses were gridded at $0.5^{\circ} \times 0.5^{\circ}$ horizontal resolution (56 km x 56 km) and used as the first guess field for a Barnes objective analysis (Koch et al. 1983) performed on the merged NGM and rawinsonde sounding data. The resulting Gempak data arrays, which combined all available data in a 40 km x 40 km grid, were used for all the mesoscale analyses in this research.

2.3. Active, Passive, and Suppressed Days

On 19 July, convective showers are seen in the KSC area (Fig. 2.2a). These showers moved northwest and were over KSC from about 1400 UTC until 1700 UTC. By 1800 UTC an east coast sea breeze front had developed and was moving westward towards central Florida leaving the east coast of the peninsula clear. This day is classified as an "active" convective day at KSC.

20 July (Fig. 2.2b) was the most active of the four days with bands of convective showers moving onshore throughout the morning. Showers were occurring at KSC by 1200 UTC and moved out of the area by about 1700 UTC. Waterspouts were observed offshore KSC and Patrick Air Force Base (45 km south of KSC) between 1200 UTC and 1300 UTC. The convection that had moved onshore in the morning slowly merged with a developing east coast sea breeze front which helped advect the showers northwestward away from KSC.

Convection was generally suppressed on 21 July (Fig. 2.2c). One convective shower developed offshore Patrick Air Force Base, produced a waterspout from 1245 UTC until 1300 UTC, dissipated shortly thereafter as it moved across Patrick Air Force Base, and convection was suppressed for the rest of the day. Convection on 22 July (Fig. 2.2d) was suppressed all day in the KSC vicinity. Showers and thunderstorms developed during the day inland over south Florida.

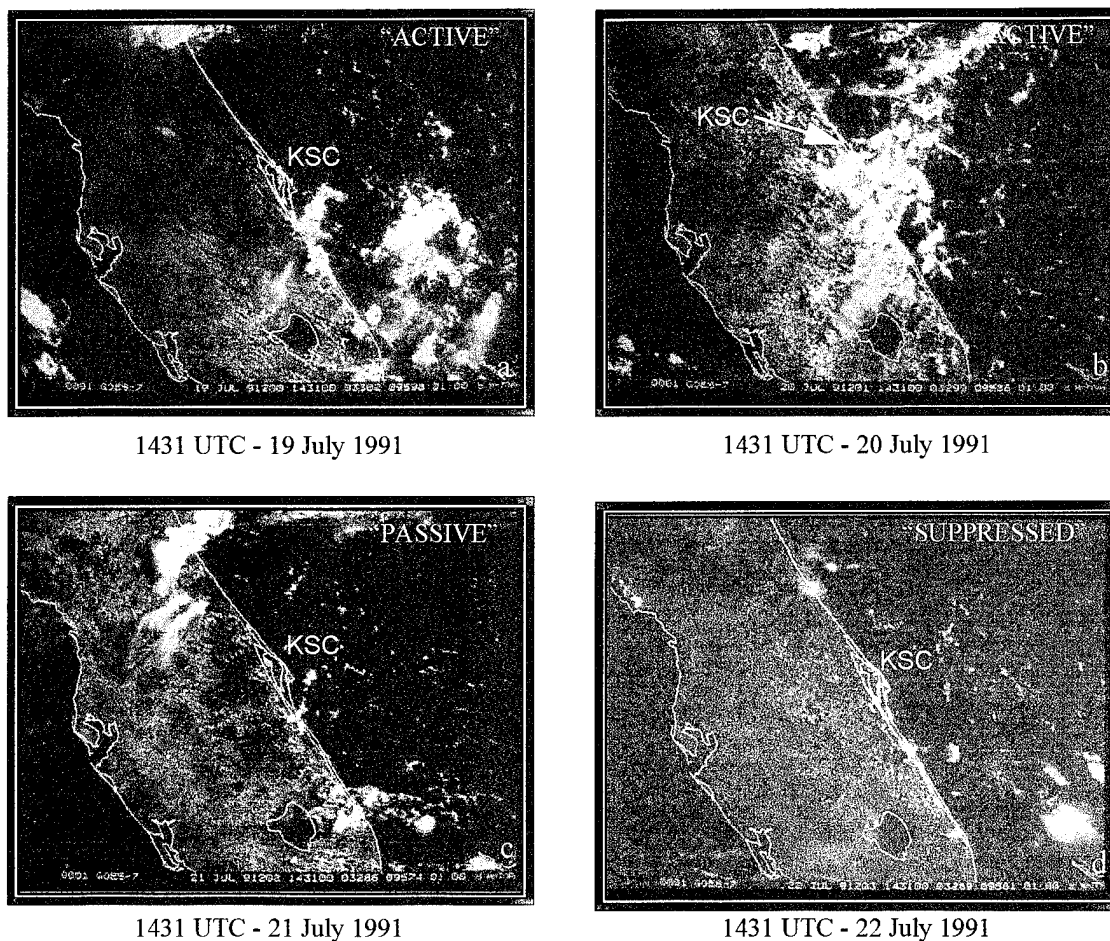


Figure 2. 2. Visible satellite imagery (1 km horizontal resolution) from GOES-7 for (a) 1431 UTC 19 July 1991, (b) 1431 UTC 20 July 1991, (c) 1431 UTC 21 July 1991, and (d) 1431 UTC 22 July 1991.

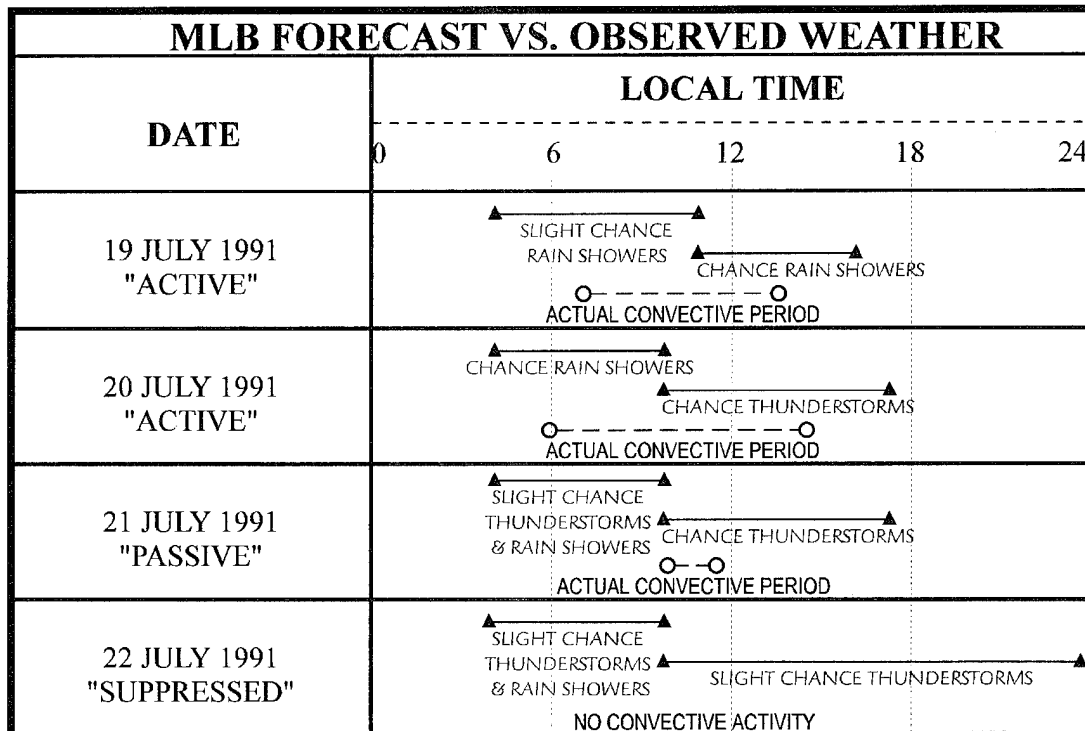
The terminal forecasts for KSC, shown in Table 2.2, demonstrate the difficulty forecasting convective activity during onshore flow. The weather at KSC was significantly different during the four days considered but the terminal area forecasts issued by U. S. Air Force Range Weather Operations forecasters each morning varied little from day-to-day.

Table 2.2. A timeline of the forecast and observed weather at KSC prepared by U. S. Air Force forecasters for 19-22 July 1991. The period in which precipitation was forecast shown by the solid lines beginning and ending with a triangle. The type of precipitation forecast is written below each solid line. The actual time when convection occurred is shown by the dashed line beginning and ending with an open circle.

KSC FORECAST VS. OBSERVED WEATHER	
DATE	LOCAL TIME
	0 6 12 18 24
19 JULY 1991 "ACTIVE"	
20 JULY 1991 "ACTIVE"	
21 JULY 1991 "PASSIVE"	
22 JULY 1991 "SUPPRESSED"	

The terminal forecasts for the same four days issued by the Melbourne National Weather Service (Table 2.3) and the actual weather observed at Melbourne were consistent with the Range Weather Operations forecasts and KSC observations.

Table 2.3. A timeline of forecast and observed weather at Melbourne, FL prepared by National Weather Service forecasters for 19-22 July 1991. The period in which precipitation was forecast shown by the solid lines beginning and ending with a triangle. The type of precipitation forecast is written below each solid line. The actual time when convection occurred is shown by the dashed line beginning and ending with an open circle.



It is clear that the forecasts changed little each day and the forecast matched the observed convective periods well on 19 and 20 July (the "active" days). However, on 21 July (a "passive" day) a few weak showers moved onshore and were in the KSC

vicinity for less than two hours, yet the forecast called for isolated thunderstorms and rain showers in the KSC vicinity from 0400 to 2400 local. On 22 July (a "suppressed" day) east-central Florida was devoid of convection yet the KSC forecast called for early morning rain showers offshore KSC with a change to rain showers at KSC and thunderstorms offshore the KSC vicinity from 0900 to 2400 local. Clearly, the forecasters did not recognize a change in the weather pattern and incorrectly forecast the precipitation on the passive and suppressed days.

2.4 Data Analysis

The surface analyses are typical for summer with a ridge of the Bermuda high extending westward to the southeast United States (Fig. 2.3). Surface pressures rise up to 4 mb over the southeast United States between 19 and 20 July as the surface ridge builds westward. Beyond 20 July at 1200 UTC (Fig. 2.3b) surface pressures remain fairly constant as the ridge becomes quasi-stationary. Without close scrutiny, the surface pattern appears "similar" on all four days, especially over east-central Florida. But closer inspection reveals the surface winds in east Florida are very light with a prevailing easterly component yet show a tendency to shift from southeast early in the period to northeast by the end. The slight change in wind direction is a subtle hint of a total column mass adjustment. Although the surface ridge does not build significantly after 1200 UTC 20 July (Fig. 2.3b), it does become cut-off with a weak closed circulation by

1200 UTC 21 July (Fig. 2.3c). This is an indication of subsidence and low-level divergence which extends southward to central Florida.

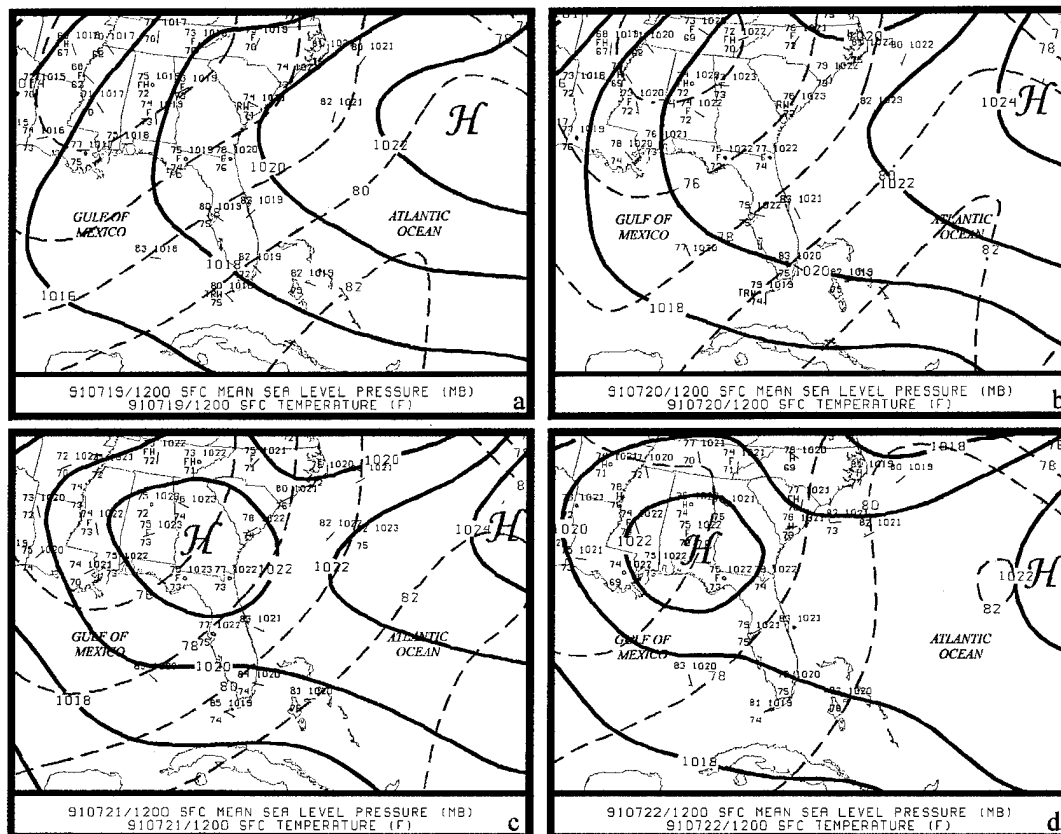


Figure 2.3. Surface analysis for (a) 1200 UTC 19 July 1991, (b) 1200 UTC 20 July 1991, (c) 1200 UTC 21 July 1991, and (d) 1200 UTC 22 July 1991. Solid contours denote mean sea level pressure at 2 mb intervals. Dashed contours denote temperature at 2 °F intervals. Surface observations are plotted as: temperature (°F) to the upper left of the station, weather using conventional abbreviations to the left, dew point temperature (°F) to the lower left, mean sea level pressure (mb) to the upper right, and wind barbs where a half (full) barb equals 5 ms⁻¹ (10 ms⁻¹).

850 mb analyses (not shown) and 700 mb analyses (Fig. 2.4) show high geopotential heights dominating the southwestern Atlantic and southeastern United States with anticyclonic curvature over Florida. The ridge axis is located across central Florida at 1200 UTC 19 July (Fig. 2.4a) and slowly migrates northward until a closed-high develops by 1200 UTC 21 July over Georgia (Fig. 2.4c). The high center migrates west and is located over Alabama by 1200 UTC 22 July (Fig. 2.4d). Heights rise an average of 40 m over the southeast United States throughout the period. The building high at 850 mb and 700 mb is consistent with a developing area of low-level divergence over the southeast United States helping to suppress convection later in the period over east-central Florida.

The next series of figures examines the pattern at 150 mb. It was found to be the level which controlled the large scale dynamics over the four days investigated. The 150 mb analyses (Figs. 2.5a, b, c, and d) show a trough dominating the southwestern Atlantic Ocean and Caribbean region through the period with a closed low moving westward from east of the Bahama Islands at 1200 UTC 19 July (Fig. 2.5a) to just south of Florida by 1200 UTC 22 July (Fig. 2.5d). The trough in this region is typical of a summertime tropical upper-tropospheric trough (TUTT) and is normally present in the North Atlantic, South Atlantic, North Pacific, and South Pacific (Fitzpatrick et al. 1995). It is a cold-core trough which is found in the subtropical and tropical Atlantic region (Whitfield and Lyons 1992). The climatological study by Fitzpatrick et al. (1995) shows that closed circulations called cold lows or TUTT cells form within the tropical upper-

tropospheric trough and move south and west along the TUTT axis throughout the summer. The long-term mean position of the TUTT axis at 200 mb during July is shown in Fig. 2.6 (after Whitfield and Lyons 1992).

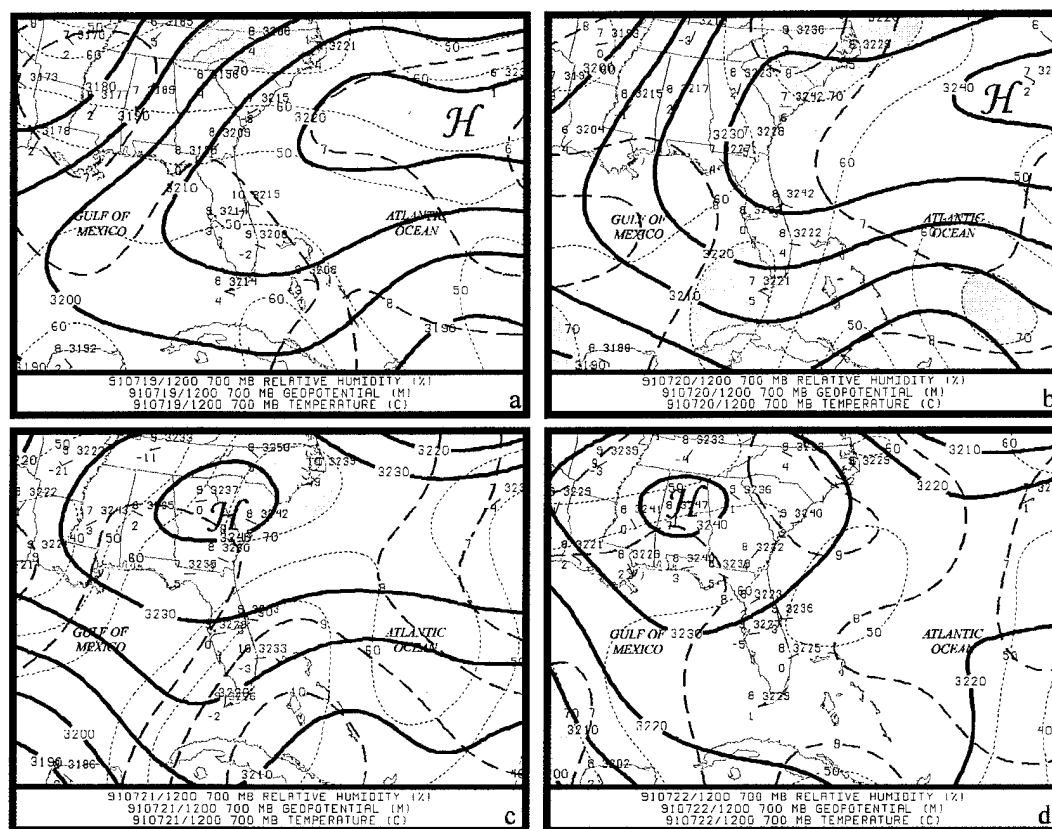


Figure 2.4. 700 mb analysis for (a) 1200 UTC 19 July 1991, (b) 1200 UTC 20 July 1991, (c) 1200 UTC 21 July 1991, and (d) 1200 UTC 22 July 1991. Solid black contours denote geopotential heights at 10 m intervals. Large dashed red contours denote temperature at 1 $^{\circ}$ C intervals. Small dashed black contours denote relative humidity (RH) and green shading indicates RH \geq 70%. Station observations are plotted as: temperature ($^{\circ}$ C) to the upper left of the station, dew point temperature ($^{\circ}$ C) to the lower left, geopotential height (m) to the upper right, and wind barbs where a half (full) barb equals 5 ms^{-1} (10 ms^{-1}).

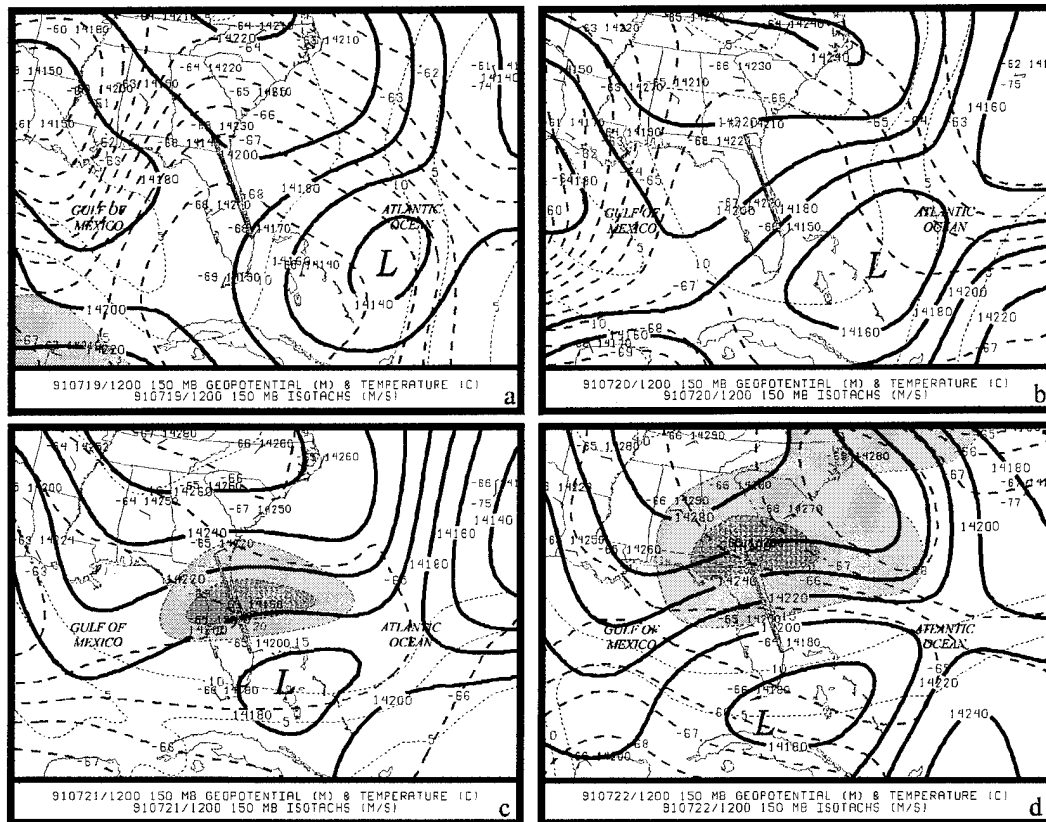


Figure 2. 5. As in Fig. 2.4 except for 150 mb and small dashed blue lines depict isotachs (ms^{-1}) that are shaded at 5 ms^{-1} intervals beginning at 15 ms^{-1} . Solid black contours denote geopotential heights at 20 m intervals.

A cold low observed at 150 mb from 19-22 July plays a crucial role in the dynamics of the situation as it tightens the 150 mb pressure gradient over Florida and the Georgia on 21 and 22 July (Fig's. 2.5c and d). To uncover this feature, in a summer, subtropical environment, it was necessary to analyze the height lines every 20 m in Fig. 5, instead of the conventional 120 m interval. The movement of the low tightens the

pressure gradient creating a weak (20 ms^{-1}) jet streak by 1200 UTC 22 July (Fig. 2.5d), also captured through an unconventional analysis.

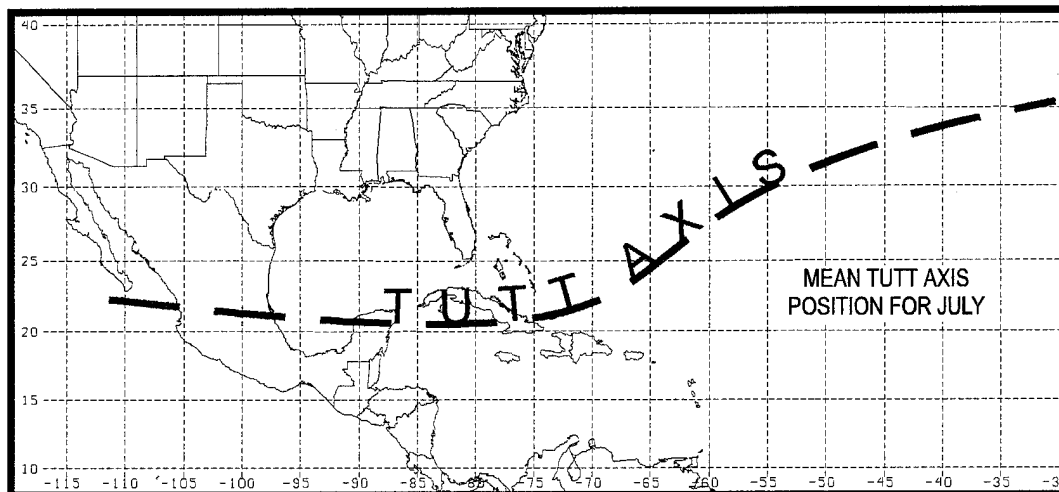


Figure 2. 6. The long-term mean position of the TUTT axis at 200 mb during July (after Whitfield and Lyons 1992).

The dynamics of the developing subtropical jet streak closely follow the jet streak model presented by Uccellini and Johnson (1979). A schematic diagram of an easterly upper tropospheric jet streak, associated transverse circulations, and vorticity patterns are shown in Figs. 2.7a, b, and c. In the entrance region of the upper tropospheric jet streak (east side), confluence and an increase in the geostrophic wind downstream (westward) are associated with ageostrophic motion (v_{ag}) toward the cyclonic (south) side of the jet streak. In the jet streak exit region (west side), diffluence and a decrease in the geostrophic wind downstream (westward) are associated with ageostrophic motion (v_{ag}) toward the anticyclonic (north) side of the jet streak (Fig. 2.7a).

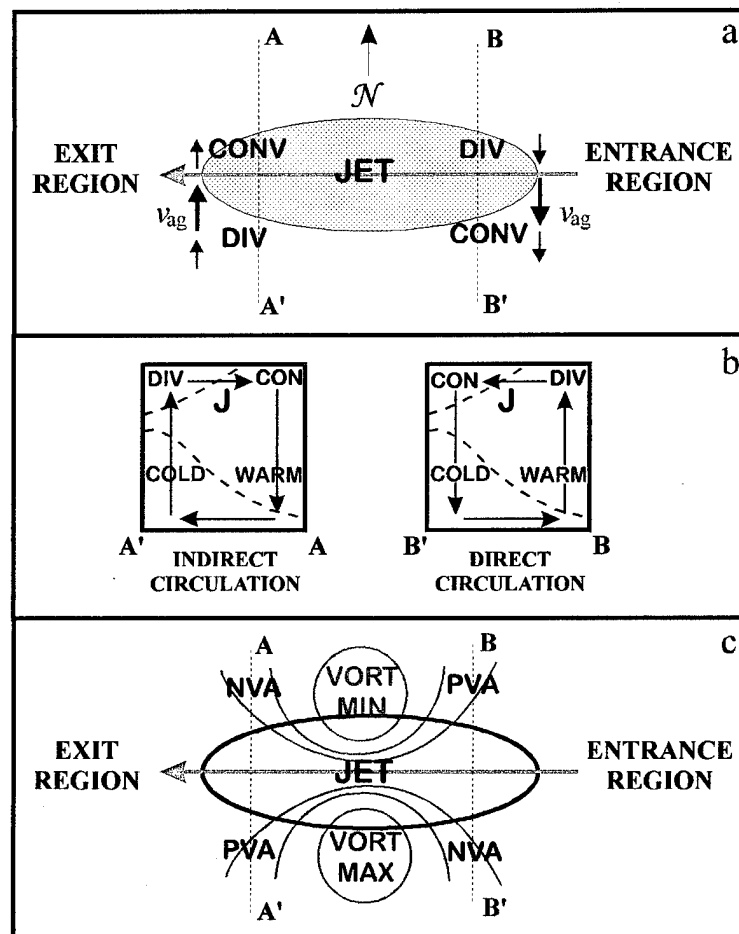


Figure 2. 7. Schematic diagram of an easterly jet streak showing (a) the transverse ageostrophic component (v_{ag}) and patterns of divergence and convergence associated with jet entrance and exit region, (b) vertical cross sections orthogonal to jet streak axis (J) illustrating vertical motion and horizontal ageostrophic wind component within the plane of the cross section, and (c) maximum and minimum relative vorticity centers and associated positive vorticity advection (PVA) and negative vorticity advection (NVA) patterns. (After Kocin and Uccellini 1990)

The vertical cross section through the jet exit region (Fig. 4.7b) shows the upper tropospheric ageostrophic motion transporting mass toward the anticyclonic (north) side

of the jet streak. The mass flux convergence on the anticyclonic side and mass flux divergence on the cyclonic (south) side increases the pressure beneath the north side and decreases the pressure beneath the south side. The mass adjustments concurrently force development of an isallobaric wind that constitutes a return branch of the direct circulation (Uccellini and Johnson 1979).

Horizontal shears generated by the jet streak will produce a vorticity maximum on the cyclonic (south) side of the jet streak and a vorticity minimum on the anticyclonic (north) side of the jet streak (Fig. 2.7c). Positive vorticity advection (PVA) will exist in the left (south) exit region and right (north) entrance region of the jet streak while negative vorticity advection (NVA) will occur in the right exit and left entrance regions, respectively.

The implications of this jet streak model are that convection would be enhanced in the left (south) exit region of the jet where upper-level divergence and PVA are occurring and convection would be suppressed in the left (south) entrance region of the jet where upper-level convergence and NVA are occurring. Testing this model against the 150 mb analyses (Figs. 2.5a, b, c, and d) reveals very good agreement. On 19 and 20 July (Figs. 2.5a and b), the flow over central Florida is weak and diffluent. The jet streak is still off the east coast of Florida and is not evident in the analyses (probably due to lack of observations over the water). However, based on the position of the jet streak and the cold low on the next two days (Figs. 2.5c and d) it can be assumed that the exit region of the jet streak is affecting the Florida weather by 20 July (the most convectively

active). On 21 July, the jet streak is centered over east central Florida indicating a transition from left (south) exit region to left entrance region in the KSC vicinity. This would correctly explain the occurrence of weak convection early in the morning changing to more suppressed conditions later in the morning. Finally, on 22 July, the jet streak has moved north and west leaving the KSC area under the influence of the left entrance region of the jet streak and, according to the model, suggests upper level convergence and downward vertical motion that would suppress convection.

The first morning soundings at CCAS are released daily at ~ 1015 UTC (0615 LST) and are representative of the pre-convective environment and background state in the KSC vicinity on days with onshore flow and morning shower activity. A series of early morning soundings analyzed show similar temperature profiles and more contrasting moisture profiles.

Early morning soundings for 20 and 22 July (Fig. 2.8a and b) reveal a contrast between the environments of the active and suppressed days. Deep easterlies were present each day with mostly weak southeasterly flow from the surface through 730 mb on 20 July (Fig. 2.8a) while the southeasterlies were confined to levels below 850 mb on 22 July (Fig. 2.8b).

The temperature profile in each sounding is similar with slightly colder temperatures aloft on the active day, 20 July (Fig. 2.8a). The 500 mb temperatures were about 3°C colder on both active days as compared to the passive and suppressed days of

21 and 22 July. This provided a slightly more unstable environment during the first two days.

Of more significance is the moisture difference seen in the dew point profiles on the two days. The 20 July sounding (Fig. 2.8a) shows a deep moist layer from the surface to over 500 mb. The 22 July sounding (Fig. 2.8b) is decidedly drier, with a very shallow moist layer from the surface to about 900 mb and then dry above. The synoptic analysis for 1200 UTC on 22 July (Fig. 2.5d) shows the 150 mb low south of Florida with a jet streak in north Florida which may account for much of the convergence aloft and subsidence evidenced in this sounding. Model results that are presented in Section 4.4, Coarse Grid Simulation Results, support this observation. The soundings on 19 and 21 July (not shown) displayed very similar characteristics in both temperature and moisture. The difference in weather can be attributed to the approach of the 150 mb low and dynamics associated with the jet streak.

Fig. 2.9 is a relative humidity (RH) time-series constructed from CCAS soundings. Note that on all four days the 850 mb RH (green line) remains above about 68%, a level typical of the summer time tropical Florida air mass. However, the 700 mb RH (blue line) shows rapidly increasing RH values on the first active day (19 July) with a maximum of 76% on 20 July during the most convectively active period and then decreasing sharply during the passive day (21 July) and remaining below 45% on the suppressed day (22 July).

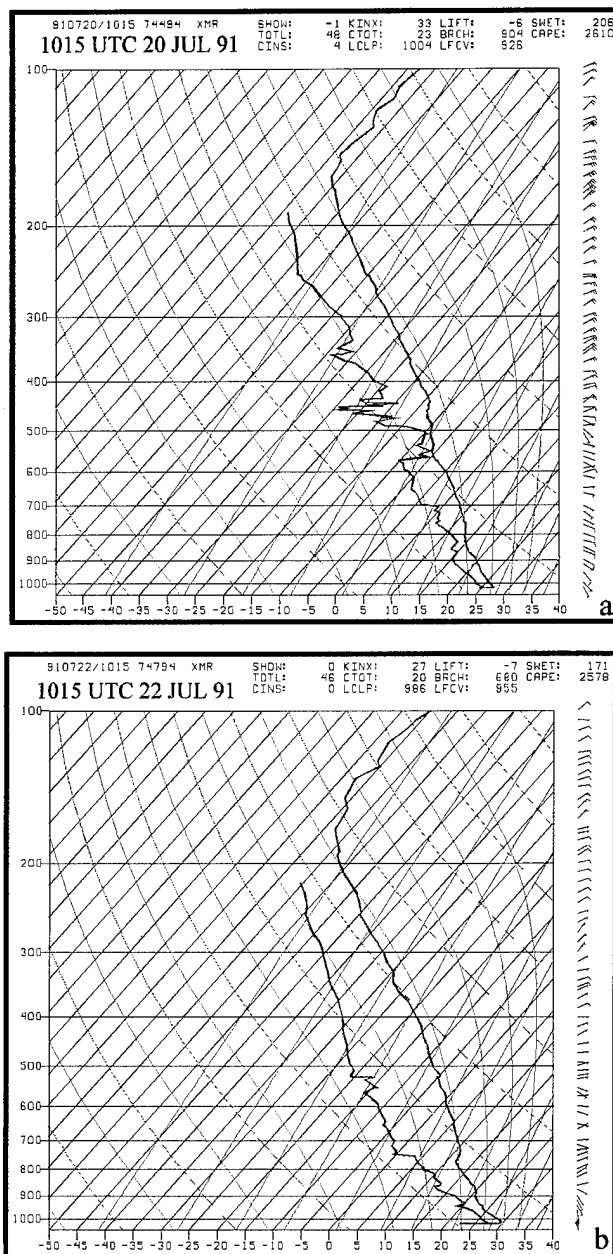


Figure 2.8. Standard skew T-log p diagrams of soundings for Cape Canaveral Air Station at (a) 1015 UTC 20 July 1991 and (b) 1015 UTC 22 July 1991. Wind barbs shown where a half (full) barb equals 5 ms^{-1} (10 ms^{-1}).

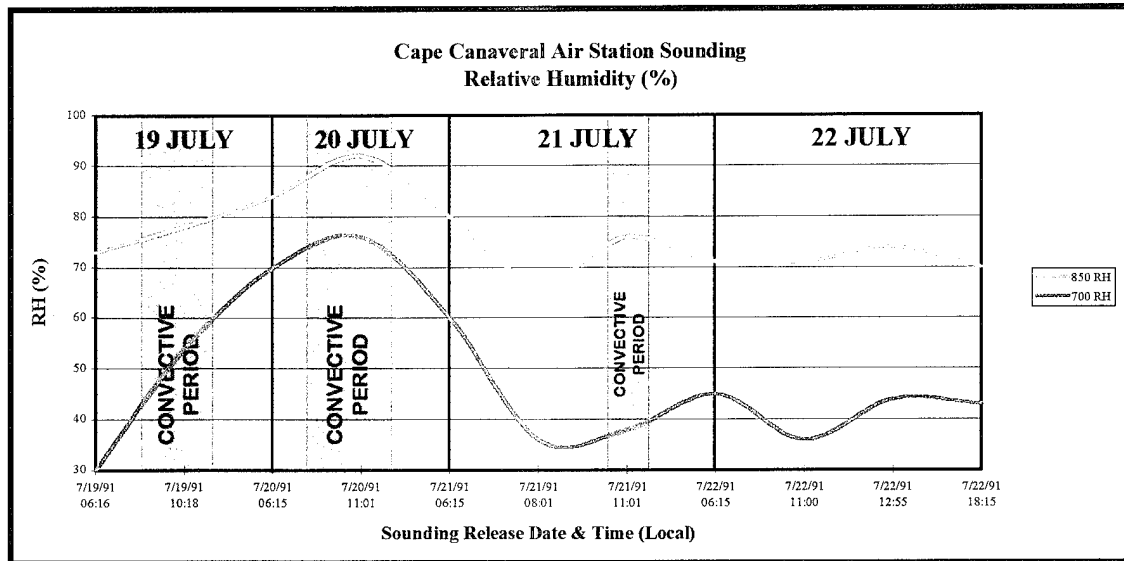


Figure 2.9. Time series of relative humidity (RH) computed from Cape Canaveral Air Station soundings from 1016 UTC 19 July 1991 (0615 L) to 0015 UTC 23 July 1991 (2015 L 22 July 1991). The convective periods in the vicinity of Kennedy Space Center are shaded. The green line denotes 850 mb RH and the blue line denotes the 700 mb RH.

To infer more information about the water vapor distribution and static stability, vertical cross sections of relative humidity and equivalent-potential temperature were produced. The cross sections are based on the combined observational and numerical model analysis grids constructed for this research (see section 2). Each cross section was drawn approximately perpendicular to the convective rainbands (refer to Fig. 2.1 for location). Relative humidity begins to increase and deepen between 1200 UTC 19 July and 1200 UTC 20 July (Fig. 2.10a and b). Deep moisture from KSC southeastward into the Bahamas is evident at 1200 UTC 20 July. The vertical extent of higher relative humidities begins to decrease at 1200 UTC 21 July (Fig. 2.10c) and then remains

relatively shallow through 1200 UTC 22 July (Fig. 2.10d), providing qualitative agreement with the convective activity.

Fig. 2.11 shows GOES-7 water vapor imagery in the 6.7 μm band. The 6.7 μm imagery is most sensitive to moisture and clouds in the middle and high layers (Scofield and Purdom 1993) with a maximum sensitivity near 400 mb (Weldon and Holmes 1986). Thus, this wavelength is appropriate for helping define, qualitatively, the mid and upper level moisture patterns.

The most prevalent feature in the water vapor images is the dark region extending across central Florida at 1200 UTC 21 and 22 July (Figs. 2.11c and d). The dark area extending parallel to the 150 mb wind maxima (see Fig. 2.5) strongly suggests drying of the air column associated with the vertical circulation induced by the jet streak (Anderson et al. 1982, Durran and Webber 1988).

The drying associated with the wind maxima is consistent with the suppression of convection on 21 and 22 July and supports the importance of the dynamics in the upper troposphere in correctly forecasting the convective activity. Water vapor imagery and data from the advanced instrument package on the new GOES-8 satellite is an important tool to investigate in application to the problem of nowcasting convective activity over Cape Canaveral.

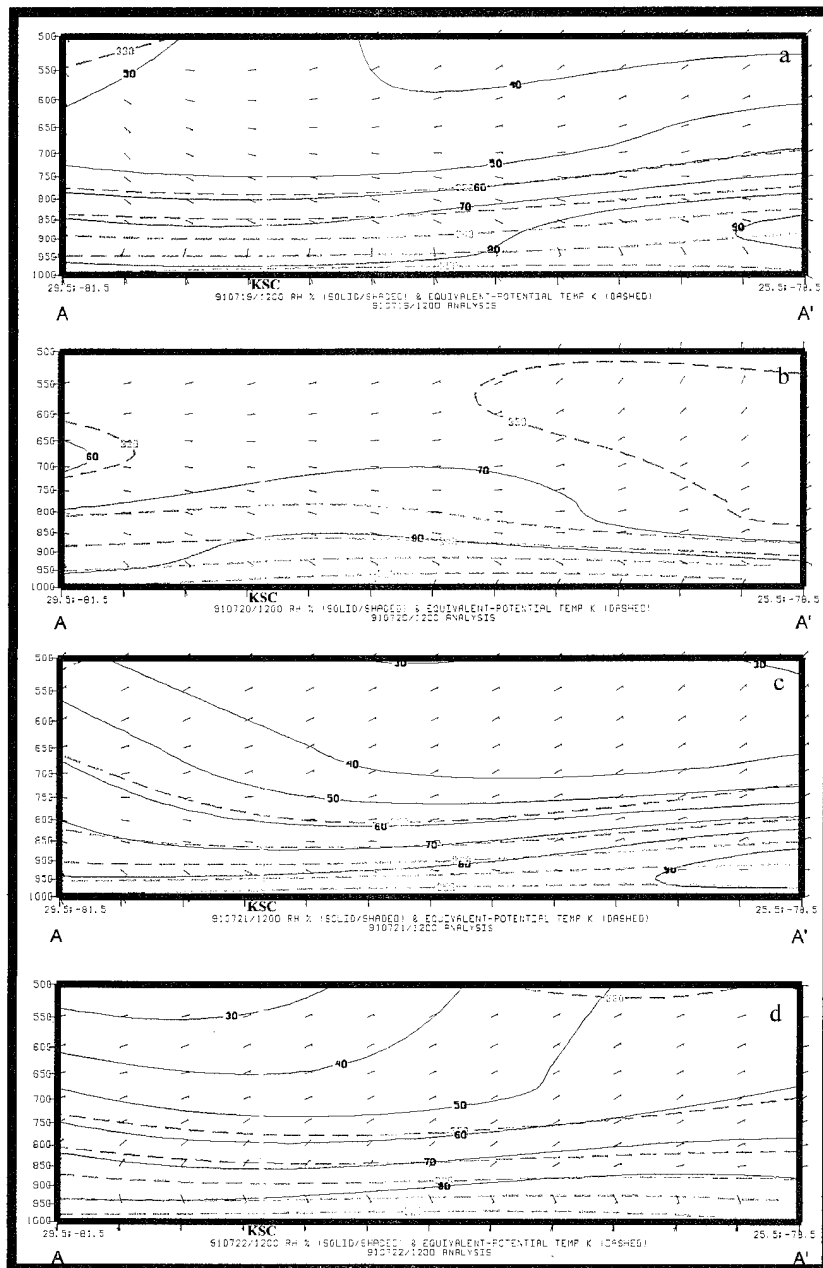


Figure 2.10. Vertical cross section from north Florida to near Nassau, Bahamas for (a) 1200 UTC 19 July 1991, (b) 1200 UTC 20 July 1991, (c) 1200 UTC 21 July 1991, and (d) 1200 UTC 22 July 1991. Solid black contours and green shaded regions denote relative humidity at 10% intervals (shaded above 70%). Red dashed contours denote equivalent-potential temperature at 5 °K intervals. Wind barbs shown where a half (full) barb equals 5 ms⁻¹ (10 ms⁻¹). The location of Kennedy Space Center is shown by the vertical cyan line.

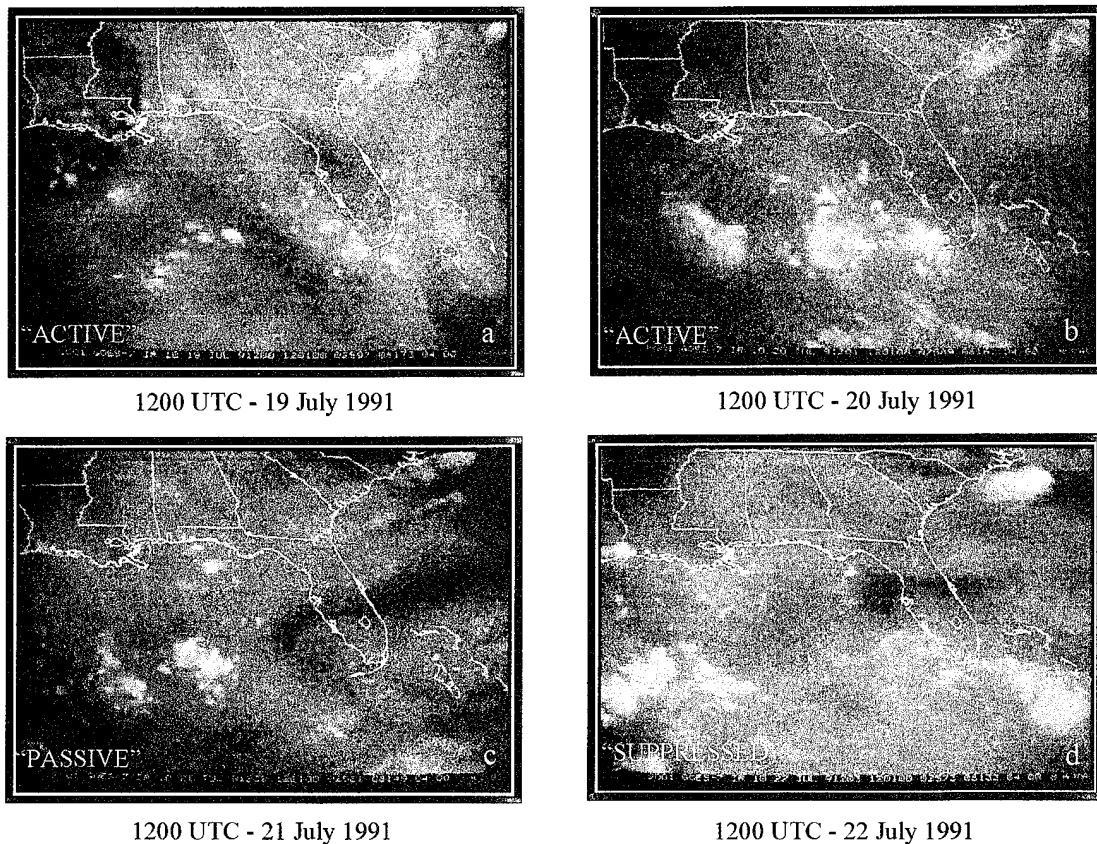


Figure 2. 11. Water vapor ($6.7 \mu\text{m}$ band) satellite imagery (8 km horizontal resolution) from GOES-7 for (a) 1200 UTC 19 July 1991, (b) 1200 UTC 20 July 1991, (c) 1200 UTC 21 July 1991, and (d) 1200 UTC 22 July 1991.

More frequent access to water vapor information with a higher horizontal resolution would greatly improve the chances of a successful forecast during onshore flow. To improve water vapor observations, Chiswell et al. (1995) suggest utilizing the Global Positioning System (GPS) to provide accurate all-weather measurements of atmospheric water vapor. Ground-based GPS receivers can provide precipitable water vapor measurements as often as every 30 minutes.

Currently, GPS consists of a configuration of 24 satellites transmitting radio signals to ground based GPS receivers. GPS signals transmitted by satellites towards the ground are delayed and refracted by atmospheric water vapor (Fig. 2.12). Water vapor is responsible for a signal delay which is nearly proportional to the quantity of water vapor integrated along the signal path. If the ground based GPS receiver is stationary and its position accurately known then measurements of the signal delay due to atmospheric water vapor can be used to estimate the vertically integrated water vapor above the receiver. Only surface pressure measurements, GPS observations, and GPS satellite orbits are required to estimate vertically integrated water vapor (Businger et al., 1995). During the GPS-STORM project (May 1993), Chiswell et al. (1995), demonstrated the utility of using GPS data in meteorological analysis. The inclusion of GPS derived precipitable water vapor (PWV) data was able to enhance the analysis of severe weather environments. The GPS derived PWV was compared to measurements made by co-located water vapor radiometers during GPS-STORM. Chiswell et al. (1995) found GPS measurements of PWV to be considerably more reliable than the co-located water vapor radiometers, especially when there was liquid water on the radiometer (due to rain, fog, or dew).

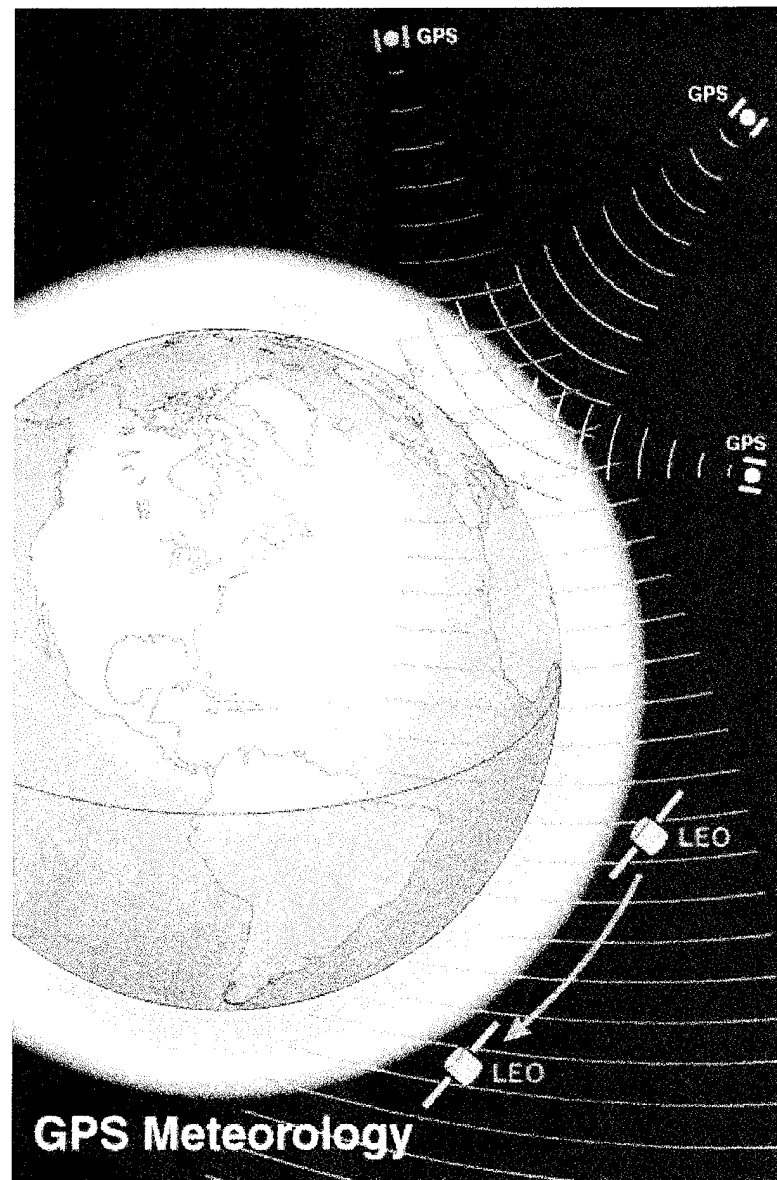


Figure 2. 12 Schematic diagram of GPS meteorology showing GPS signals passing from GPS satellites, orbiting at heights of ~20,000 km, through the intervening Earth's atmosphere to ground-based receivers, and to a low earth orbit (LEO) satellite orbiting at a height of ~775 km. The delay of signals arriving at ground based receivers is proportional to the intervening water vapor. Signals propagating from the GPS satellite to the LEO satellite are refracted by the Earth's atmosphere during the ~60 second period before the signal is occulted by the Earth, providing a refractivity profile of the atmosphere. (After Businger et al. 1995).

Since water vapor distribution appears critical to forecasting convective rainband activity at KSC during onshore flow, GPS could provide an alternate method of extracting PWV to compliment conventional rawinsonde observations. GPS receivers placed at locations along the Florida east coast, stationary buoys, the Bahama Islands, Cuba, and the Dominican Republic (Fig. 2.13) would vastly improve water vapor analyses during onshore flow.

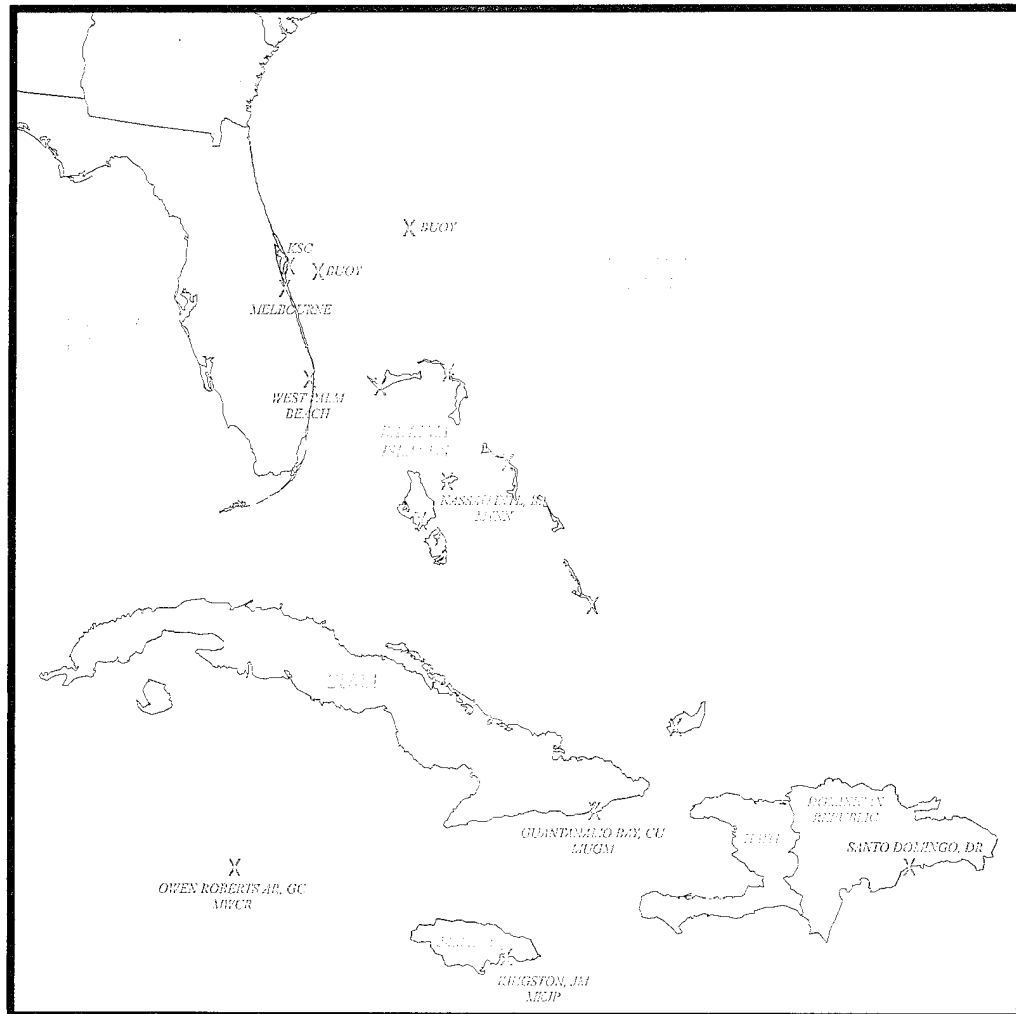


Figure 2. 13. Map of Florida and the Caribbean region showing potential locations of the GPS receivers (X).

3. CONVECTIVE INITIATION AND RAINBAND ORGANIZATION

3.1 Boundary Layer Convection

In the absence of in situ data east of Florida, radar and satellite data provide the mesoscale information needed over the water to observe the structure of the convection. Visible satellite imagery reveal open cellular convection in the marine boundary layer on each of the four days (Fig. 2.2), indicating upward surface heat fluxes leading to Rayleigh-Bernard cellular convection (Emanuel 1994). During active days convection is observed to trigger at the apex of intersecting cells, with new convection triggered by outflow boundaries. Subsequently, convection is organized into rainbands.

Radar observations were taken during CaPE, with single-Doppler scans from NCAR's CP-4 radar reaching up to 120 km offshore. The CaPE radars were turned on at ~1100 UTC each day; too late to see precipitation development for this case, but in time to observe rainband alignment and movement. The axes of the rainbands in the radar reflectivity scans all four days are aligned along the wind shear in the layer above the boundary layer. A radar reflectivity plot from the CP-4 Doppler radar for 20 July at 1405 UTC is shown in Fig. 3.1. On this day, the bases of the convective rainbands were about 925 mb and the tops were about 535 mb. The Fig. 3.1 inset shows one of the rainbands from the radar reflectivity plot. The rainband is oriented with its length parallel to the wind shear over the depth of the rainband (longitudinal mode). Also, the rainbands moved perpendicular to the wind shear over the depth of the rainband. Both

of these observations have implications for the type of instability present each day which is discussed in the upcoming sections.

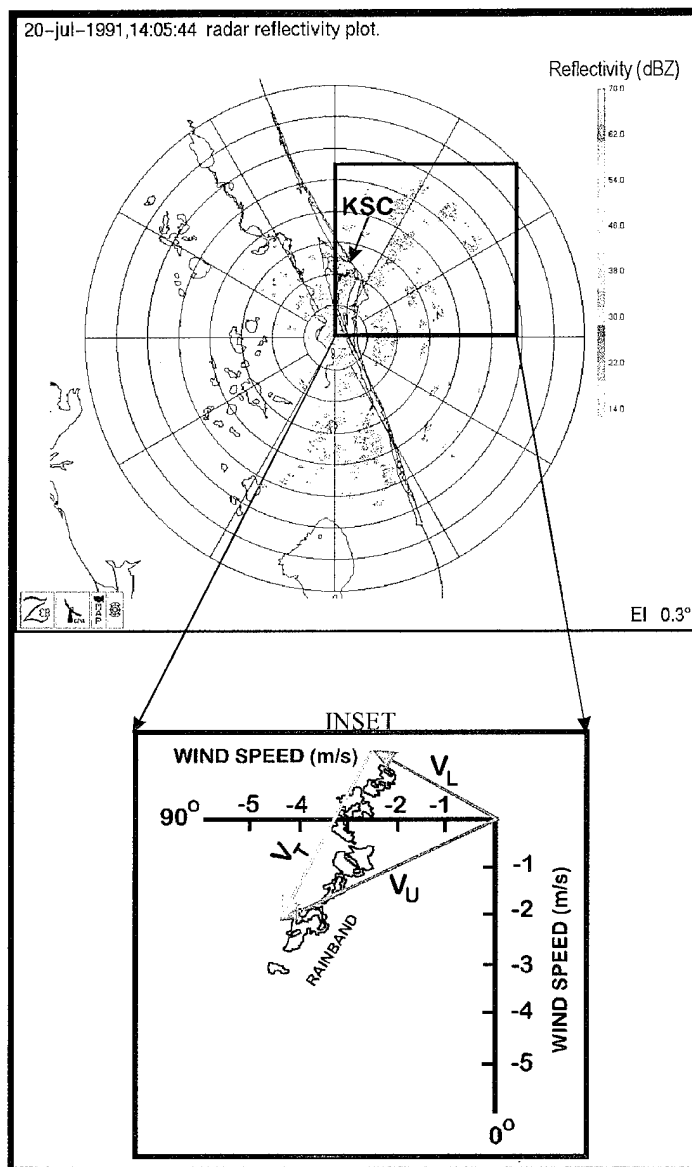


Figure 3.1. Plan Position Indicator (PPI) view of reflectivity from the CP-4 Doppler radar for 1405 UTC 20 July 1991. The inset shows the rainband alignment parallel to the wind shear vector ($V_T - V_B$) in the rainband layer where V_T is the wind vector at the top of the rainband layer (535 mb) and V_B is the wind vector at the bottom of the rainband layer (925 mb).

Based on previous research (Emanuel 1994) four convection initiation processes were considered to explain the organization of the convection into rainbands. These include CSI, IPI, wave-CISK, conventional static stability and the effects of moisture distribution on suppressing convection initiation. A trigger mechanism must be present during the convective periods that occurred between 19 and 22 July. But an available trigger mechanism may not be limited to only the convective periods - one may be present during the passive or suppressed periods as well.

3.1.1 Symmetric Instability

The role of CSI was examined relative to production and maintenance of rainbands. Vertical cross sections of constant angular momentum (M) and equivalent potential temperature (θ_e) can be used to determine whether regions of the atmosphere are unstable to moist symmetric overturning (Emanuel 1994). Houze (1993) states that CSI exists when the temperature lapse rate of a moist but unsaturated environment is conditionally unstable on a surface of constant M (the slope of the M surface must be less than the slope of the θ_e surface). Theory for symmetric instability predicts the rainbands should be oriented parallel to the thermal wind in the overturning layer.

CSI is derived by first computing absolute momentum on an equivalent-potential temperature surface:

$$\frac{dv}{dt} = -f \left(f - \frac{\partial u_g}{\partial y} \right)_{\theta_e} \delta y = -f \left(\frac{\partial M}{\partial y} \right)_{\theta_e} \delta y \quad (3.1)$$

Where the flow is inertially unstable if:

$$\left(\frac{\partial M}{\partial y}\right)_{\theta_e} < 0 \text{ which implies } \frac{dv}{dt} > 0 \quad (3.2)$$

and parcel continues to accelerate in the direction it was initially moved.

Negative equivalent-potential vorticity (moist potential vorticity) must meet necessary criteria for CSI (Bennetts and Hoskins, 1979). Regions of negative equivalent-potential vorticity (P) will be unstable to moist-symmetric overturning a condition that can be shown by evaluating potential vorticity on an equivalent-potential temperature surface:

$$P_{\theta_e} \propto g \frac{\partial \theta_e}{\partial z} (\zeta_{\theta_e} + f). \quad (3.3)$$

If $\frac{\partial \theta_e}{\partial z} > 0$ then the atmosphere is buoyantly stable and P_{θ_e} is negative because ζ_{θ_e} is negative which indicates inertial instability.

Theory for symmetric instability predicts the rainbands should be oriented parallel to the thermal wind in the overturning layer. These bands align in a configuration called “longitudinal roll convection” (Businger and Walter, 1988). The rainbands observed over the Atlantic Ocean offshore KSC on all four days were oriented parallel to the thermal wind, consistent with CSI (Snook 1992). However, vertical cross sections of equivalent-potential vorticity (P_{θ_e}) and M versus θ_e were constructed for 0000 UTC and 1200 UTC each of the four days. In all cases, P_{θ_e} was negative where θ_e increased with

height (a necessary condition for CSI) (Bennetts and Hoskins 1979). However, the slope of the M surfaces was greater than the slope of the θ_e surfaces, a condition indicating CSI was not responsible for the convective rainbands. An example of a cross section for 20 July is shown in Fig. 3.2.

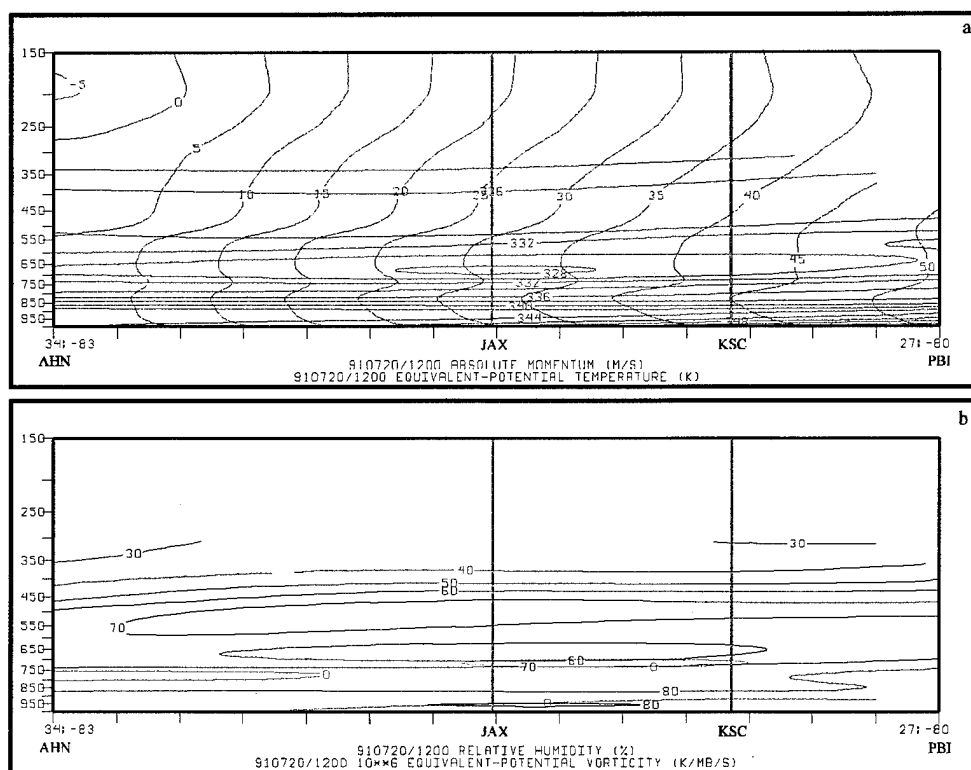


Figure 3.2. Vertical cross sections for 1200 UTC 20 July 1991 of (a) absolute momentum (M) in ms^{-1} (blue lines) and equivalent potential temperature (θ_e) in $^{\circ}\text{K}$ (red lines) and (b) relative humidity (RH) in % (black lines) and equivalent-potential vorticity (P_{θ_e}) in K/mb/s (green lines) from Athens, GA (AHN) to West Palm Beach, FL (PBI).

3.1.2 Inflection Point Instability

IPI is a mechanism for roll formation in which the wind profile exhibits an inflection point or shear in the cross-roll direction (Lilly, 1966; LeMone, 1973; Brown 1980). Local relative vorticity maxima are located at these inflection points. The fluid is unstable and the flow adjusts to remove this instability. IPI theory predicts the wavelength of convective rolls is $\sim 2\pi$ times the height of the inflection point and the convective rolls move with the wind speed perpendicular to the band at the height of the inflection point. In an unstable boundary layer, the IPI mechanism would be suppressed and a parallel instability mechanism would continue to operate.

The CCAS soundings were used to produce profiles of the mean winds parallel (along-roll) and perpendicular (cross-roll) to the orientation of the rainband. The x-axis (u -wind component) was rotated to be aligned parallel to the convective rainbands each day (Fig. 3.3). An inflection point is observed at about 2000-2500 m each day in the rotated u -component plot (along-roll). Since the inflection point is in the along-roll direction it is not probable that IPI is responsible for rainband development or alignment.

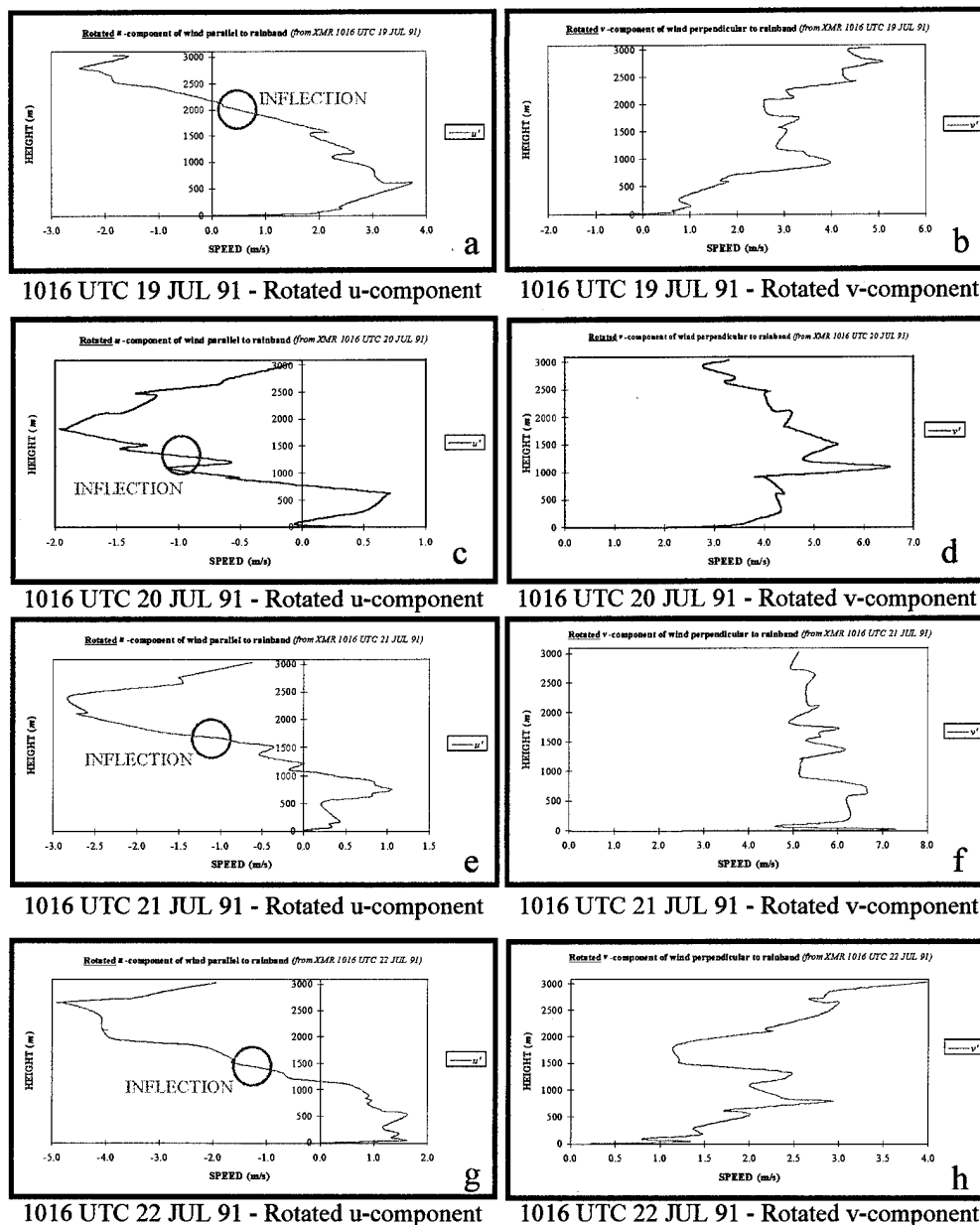


Figure 3.3. Rotated u and v wind components from the first morning sounding at CCAS. The x-axis is wind speed (m s^{-1}) and the y-axis is height (m). The u -component is aligned parallel to the convective rainband and the v -component is orthogonal to the convective rainband. Inflection point shown by blue circle.

Also, examination of CP-4 Doppler radar imagery for 19-22 July indicates the propagation velocity of the convective rainbands were about about 3 to 4 m s⁻¹ faster than the actual wind speed at the height of the inflection point. This fact also discounts the likelihood that IPI organized the rainbands. Since an inflection is observed in the along-roll profile each day, the IPI could be responsible for spacing of the convective cells along the rainbands.

3.1.3. Wave-CISK

CISK as defined by Lindzen (1974) is attained when a low-level convergence field associated with a large-scale meteorological system lifts surface air to some critical height (z_c) where cumulonimbus convection sets in. Latent heat released in the cumulus convection, in turn, forces the large-scale motion whose low-level convergence gave rise to the convection. Furthermore, Lindzen (1974) defines wave-CISK as motions that do not require Ekman pumping in order to produce CISK. This class of motions include those associated with internal waves such as gravity, Kelvin, mixed gravity-Rossby, and Rossby. Sun (1978) included latent heat effects in linear models following the wave-CISK hypothesis proposed by Lindzen. These effects were of latent heat being released in vertical columns in proportion to low-level moisture convergence and evaporative cooling when low-level moisture was divergent. Sun determined that the orientation and speed of the rainbands varied based on the dominance of buoyancy generated heat release or the conversion of kinetic energy from the mean flow. If buoyancy dominates,

then the rainbands are oriented parallel to the wind shear in the layer and remain stationary relative to the mean flow in the rainband layer. This minimizes the tendency of the shear to suppress convection. As previously discussed, the rainbands were oriented parallel to the wind shear in the layer but they also were stationary relative to the mean flow as the buoyancy mode of wave-CISK would suggest. Therefore, it is likely that wave-CISK played a role in development, maintenance, and propagation of the convective rainbands investigated here. Since the large-scale flow remained mostly unchanged during the period investigated it is most likely that wave-CISK was a dominant process aiding in production and maintenance of these rainbands.

3.2. Static stability

All CaPE and conventional soundings were analyzed for convective available potential energy (CAPE), convective inhibition energy (CINE), and convective stability indices (Lifted Index, Showalter Index, Vertical Totals Index, Cross Totals Index, Total Totals Index, K-index)¹.

CCAS soundings were chosen to represent the instabilities presented because the rawinsondes had good exposure to onshore flow, good temporal resolution, and this is the primary sounding used by the forecasters. The energy realized when conditional instability is released is CAPE (according to parcel theory) and is written as:

$$CAPE = \int_{LFC}^{EL} g \frac{T_v^{parcel} - T_v^{env}}{T_v^{env}} dz \quad (3.4)$$

¹ Refer to Pepler (1988) for a description and discussion of each of these indices and their applications.

CAPE shows the integrated buoyant energy of moist air and represents the positive area on a sounding where LFC is level of free convection, EL is the equilibrium level (neutral buoyancy level), T_v^{parcel} is the virtual temperature of the parcel and T_v^{env} is the virtual temperature of the environment. CAPE was first computed by using a surface mixing ratio and then by using a mean mixing ratio in the lowest 100 mb. Both methods yielded wildly varying values of CAPE. The "best" results were obtained using a mean mixing ratio, yet CAPE ranged from a minimum of 1100 J kg^{-1} to a maximum of 4500 J kg^{-1} and both occurred on the suppressed day, 22 July. Otherwise, CAPE varied between 1800 J kg^{-1} and 2900 J kg^{-1} for all other times with no correlation to the convective activity.

Williams and Renno (1993) completed a climatological study of conditional instability related to CAPE for tropical sounding locations around the globe. They indicate stored energy on the order of 1000 J kg^{-1} is present over large areas of the tropics and is sustained day and night. They showed that CAPE is very sensitive to the equivalent-wet bulb potential temperature (θ_w) of the layer from which a parcel is initially lifted. They also conducted a θ_w climatology related to CAPE for the tropical sounding locations and found a zero-CAPE intercept (θ_{wc}) where CAPE vanishes. The θ_{wc} was found to be narrowly distributed from $22\text{-}23^\circ \text{C}$. They showed that for tropical boundary layers with θ_w larger than 23°C , CAPE increases (on average) at a rate of about $1000 \text{ J kg}^{-1} \text{ }^\circ \text{C}^{-1}$ of θ_w (based on the assumption of lifting from the surface). All tropical stations analyzed in their study show systematic increases in CAPE for θ_w values

larger than the equilibrium θ_{wc} , suggesting tropical convection is generally unable to maintain an equilibrium CAPE atmosphere. For each CCAFS sounding investigated, θ_w was calculated (Wallace and Hobbs 1977) and was larger (the minimum was 22.7° C) than the threshold value of about 23° C. This indicates finite CAPE was present on each of the four days, yet there is no discernible pattern to CAPE or θ_w and the corresponding convective periods.

Since CAPE was present each day yet convection was not always initiated, there must be a process or processes inhibiting release of the stored energy. A typical barrier to look for would be a pronounced capping inversion. The convective inhibition energy (CINE) was examined for each CaPE sounding. CINE indicates the integrated buoyant energy needed to lift a surface parcel to the level of free convection and represents the negative area on a sounding between the surface (SFC) and LFC and is calculated by:

$$CINE = \int_{SFC}^{LFC} g \frac{T_v^{parcel} - T_v^{env}}{T_v^{env}} dz \quad (3.5)$$

CINE is a measure of “cap” or “lid” strength. Typical tropical values of CINE range from 0 J kg⁻¹ to 200 J kg⁻¹ with a mean value of 20 J kg⁻¹ (Williams and Renno 1993). Although CINE values are climatologically much smaller than tropical CAPE values, a parcel velocity of 4.5 m s⁻¹ is required to overcome a negative area of only 10 J kg⁻¹ and a parcel velocity of 20 m s⁻¹ is required to overcome a negative area of 200 J kg⁻¹ ($w = \sqrt{2 \cdot CINE}$). Very small values of CINE (about 2-8 J kg⁻¹) were observed on the

two active days (19 and 20 July) and the passive day (21 July) indicating little resistance to a parcel rising from the boundary layer. On the suppressed day (22 July) CINE jumps to near 57 J kg^{-1} by the 1255 L sounding which requires parcel velocities of 10.7 m s^{-1} . One can conclude that CINE, is more applicable than CAPE, as a predictor for convective activity during these four days. But it cannot be CINE alone suppressing convection since the amount of convective activity that occurred on 19, 20, and 21 July varied significantly from strong on 20 July to almost non-existent on 21 July. Also, CINE was only 2 J kg^{-1} (requiring $w = 2 \text{ m s}^{-1}$) during the morning of 22 July and there was no convection at all. This would suggest another hindrance to convection (at least on 22 July and part of 21 July). Besides the large-scale dynamics present due to upper-level convergence from the 200 mb low, it is possible that an entrainment process acting on the small Rayleigh-Bernard cells may supply neutral buoyancy and suppress convection in the lowest levels of the atmosphere.

Convective stability indices are used daily by forecasters supporting space launch activities and indicate the overall stability of a sounding expressed as a single value (Peppler 1988). Indices of this type have the advantage of ease of computation, flexible choice of the layer most pertinent to the particular problem or area, and a numerical form convenient for ready use in objective studies and operational forecasting. On the other hand, important details of the lapse-rate structure may be smoothed or completely missed in these indices, even when the index is carefully chosen and evaluated. Indices

are most useful only when combined, either objectively or subjectively, with other data and considerations.

The static stability analyses indicate that the single most important factor affecting development and maintenance of the convective showers is distribution of water vapor. Of the convective stability indices investigated (Lifted Index, Showalter Index, Vertical Totals Index, Cross Totals Index, Total Totals Index, K-index), only the Cross Totals and K-Index showed a correspondence with the active, passive, and suppressed convective events. Of these the K-Index showed the best ability to discriminate the convective activity, but neither parameter provided a clear indication of level of convective activity. The critical factor is 700 mb dew point depression as used in the K-Index. Cross Totals was only marginally effective because it only addresses water vapor at 850 mb. The K-Index time-series for the CCAS sounding (Fig. 3.4) shows a fair correspondence to the most convectively active periods, with a maximum of 35°C during the most active period on 22 July. It does marginally well during the other two convectively active periods, but the K-Index remains relatively high on 22 July. K-Index probably works best on 20 July because the vertical extent of the moisture was significant through the 700 mb level. But it fails to adequately differentiate between active and suppressed days because the 850 mb moisture was consistently high on each day, resulting in an elevated K-Index. The RH signal in the CCAFS soundings (Fig. 2.8) suggest a modification to the CT, K-Index and (possibly) TT to more accurately reflect

the water vapor distribution at levels above the usually moist 850 mb during the Florida summer.

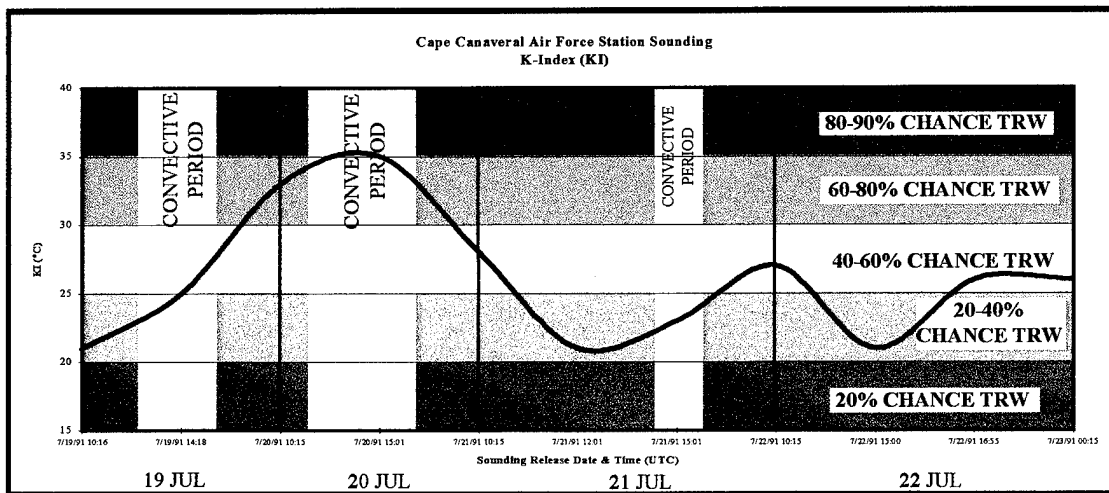


Figure 3. 4. Time series of K-Index (KI) computed from Cape Canaveral Air Station soundings from 1016 UTC 19 July 1991 (0615 L) to 0015 UTC 23 July 1991 (2015 L 22 July 1991). The probability of thunderstorms is shown by the horizontal shading. The convective periods in the vicinity of Kennedy Space Center labeled. The black line denotes the KI.

4. NUMERICAL SIMULATIONS

4.1 Description of the Mesoscale Atmospheric Simulation System

All numerical simulations used the Mesoscale Atmospheric Simulation System (MASS) which is a hydrostatic atmospheric model based on a set of equations consisting of 7 prognostic variables: temperature, water vapor mixing ratio, x-space u -wind component, y-space v -wind component, surface pressure, cloud water/ice mixing ratio, and rainwater/snow mixing ratio (MESO, Inc. 1995). The original version of MASS used in this research was developed by Kaplan et al. (1982) as the Goddard Mesoscale Atmospheric Simulation System (GMASS) and described by Manobianco et al. (1994). The version of MASS used in this research was developed by MESO, Inc. and includes a prognostic grid-scale moisture scheme, an enhanced surface energy budget, a modified Kuo cumulus parameterization scheme that included convective scale downdrafts, and a more comprehensive long and short wave radiation scheme (Zack et al., 1991). Additional improvements to the MASS convective parameterization and surface physics were made during 1992 and the early portion of 1993, followed by replacing the objective analysis scheme (Barnes 1964) with a three-dimensional multivariate optimal interpolation (3-D OI) scheme in 1995 which has resulted in MASS version 5.8 (MASS 5.8) that is used in this research.

The 3-D OI scheme will estimate the value of a set of gridded variables at a set of grid points that can be created from a set of meteorological observations distributed

irregularly throughout the analysis domain by forming an optimal linear combination of the observations closest to the grid point (MESO, Inc. 1995). This results in an analyzed value at the grid point (A_i) from:

$$A_i = B_i + \sum_{k=1}^K w_k \frac{rms_i}{rms_k} [O_k - B_k] \quad (4.1)$$

Where K is the total number of observations allowed to influence the grid point i , the subscript k refers to observation locations, w_k is the weight associated with observation k , rms_i is the root mean square observational error for variables of the same type as observation k , B is the first guess value, and O is the observed value (MESO, Inc. 1995).

MASS is intended for short-term simulations (0-48 h) over modest size domains with a horizontal grid resolution of 10 km to 50 km (MESO, Inc. 1995). Recent developments in computer capability have made it possible to execute MASS simulations over a limited area for real-time applications on moderately-priced high performance desktop computer workstations.

MASS was chosen to model onshore flow regimes at Kennedy Space Center (KSC) for a number of reasons. First of all, the Applied Meteorology Unit (AMU), which is co-located with Range Weather Operations at Cape Canaveral Air Station (CCAS), has been evaluating MASS since it was delivered from MESO, Inc. in March 1993 for application as a real-time forecasting tool for use by Range Weather Operations in support of all space launch activity from KSC and CCAS. As of April 1995, MASS

was being used on a limited operational basis by Range Weather Operations forecasters while AMU evaluation continues. Second, MASS was ported to a Kubota Graphics 3400 desktop computer workstation with a DEC Alpha AXP processor which was purchased to run MASS locally at North Carolina State University. This would help simulate computational conditions for running MASS at CCAFS for operational applications. Finally, the onshore flow regime forecast problem required a model that could simulate the atmosphere over modest size domains with a horizontal grid resolution of 10 km and a relatively short time period (0-6h). Zack et al. (1988 and 1991) showed the effectiveness of MASS in simulating convective cloud systems over Florida and in forecasting thunderstorms at KSC.

4.2 MASS Scheme for Onshore Flow

MASS 5.8 was run at North Carolina State University (NCSU) in a mode as similar as possible to the way it is run daily at CCAS for "operational consistency". Because the AMU had significant experience configuring MASS to run specifically for Space Shuttle support in the Florida environment it was decided to match their coarse mesh setup exactly and then conduct sensitivity tests using a fine mesh (nest) designed specifically for the onshore flow regime. The nested MASS model grids used in this research are similar to the AMU's but the areal coverage is larger, especially to the east of Florida.

The coarse mesh grid covered the southeast United States, western Atlantic Ocean, and Caribbean region with a horizontal grid resolution of 45 km (Fig. 4.1). After the coarse mesh was run, a series of nests were run with the grid covering most of Florida and the Bahama Islands with a horizontal grid resolution of 11 km (NCSU grid) (Fig. 4.2). The NCSU grid domain is larger than the one used operationally at the AMU (Fig. 4.3) because the Kubota Graphics workstation has more computational power than the AMU's computer and there was no operational time constraint on the research model simulations. It should be noted, however, that a 12 hour nest simulation took 4.2 hr to run on the Kubota Graphics workstation which (by current standards) has a relatively slow processor and modest amount of RAM. Computers with 275 megahertz Alpha AXP processors and 128 megabytes of RAM are available for about the same cost of the Kubota Graphics workstation when purchased in 1993. Computers with this capability could run the larger fine mesh grids quickly enough for operational use.

4.3 Coarse Grid Simulation Configuration

The observation-based objective analyses generated for 19-22 July 1991 were done using a 43 km horizontal grid resolution. This was the smallest grid resolution that could be appropriately used given the spacing of the observations in the data set. The coarse MASS grid was run with 45 km horizontal resolution (true at 27.5° N) with 22 vertical sigma levels (identical to the AMU coarse setup). The coarse simulations were

run once for each of the four days to determine if they could duplicate the dynamics observed in the analyses and could be used as a first guess for 24 nested simulations.

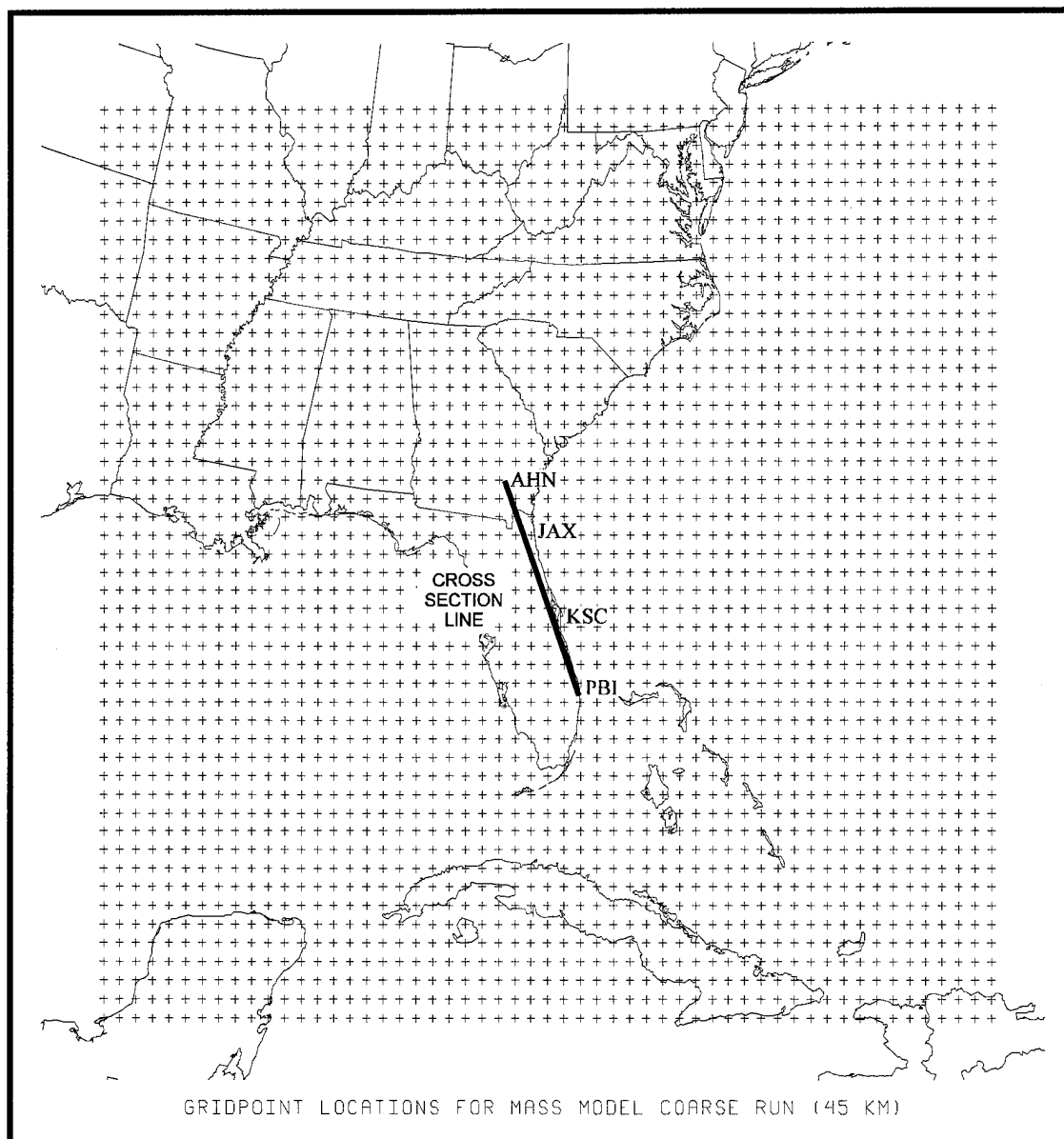


Figure 4. 1. The MASS coarse mesh grid covering the southeast United States, western Atlantic Ocean, and Caribbean region with a horizontal grid resolution of 45 km. The line extending from Athens, GA (AHN) to West Palm Beach, FL (PBI) denotes the axis for MASS coarse grid vertical cross sections.

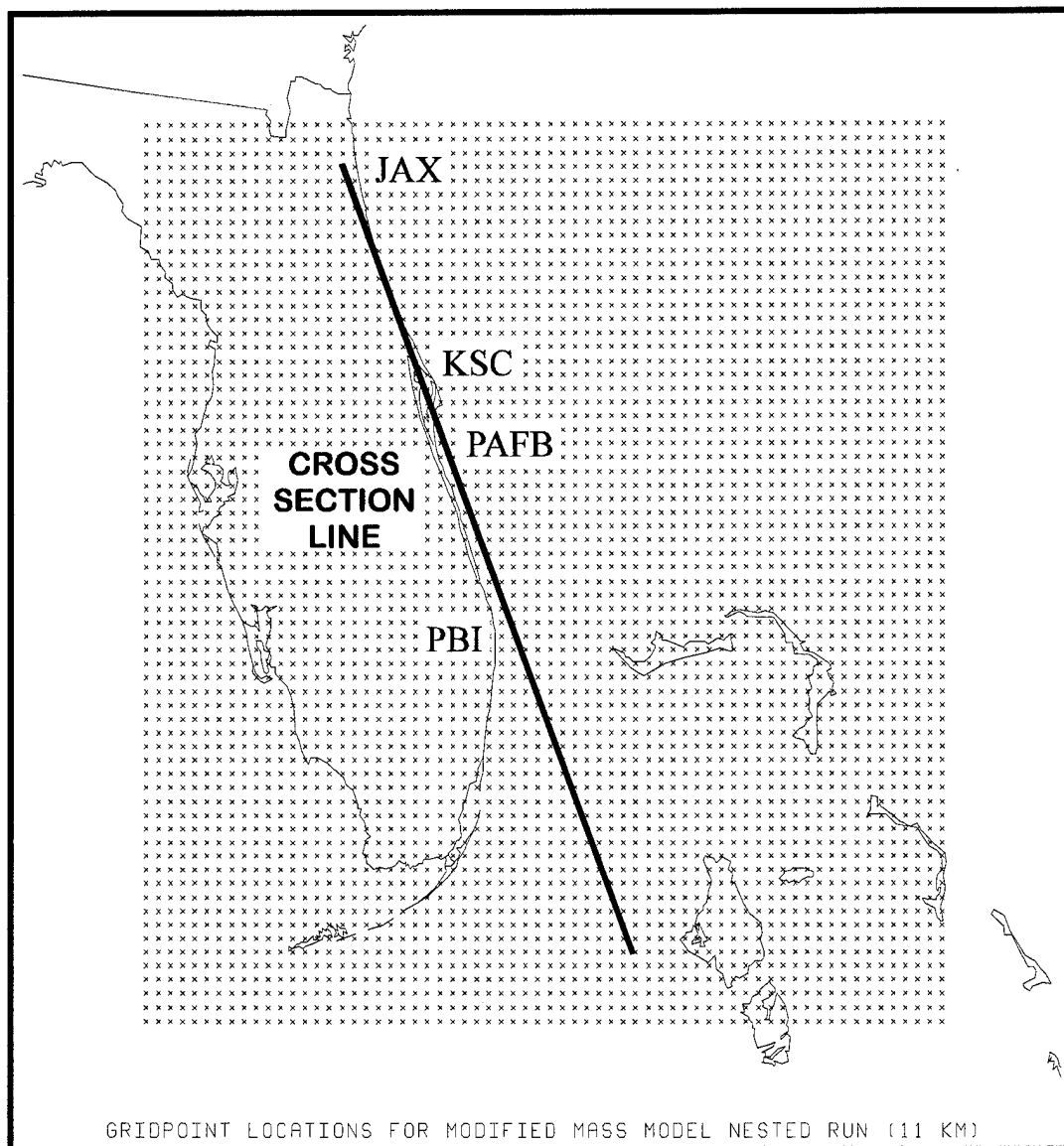


Figure 4. 2. NCSU nest grid covering most of Florida and the Bahama Islands with a horizontal grid resolution of 11 km. The line extending from Jacksonville, FL (JAX) to just west of the Bahama Islands denotes the axis for MASS nest grid vertical cross sections.

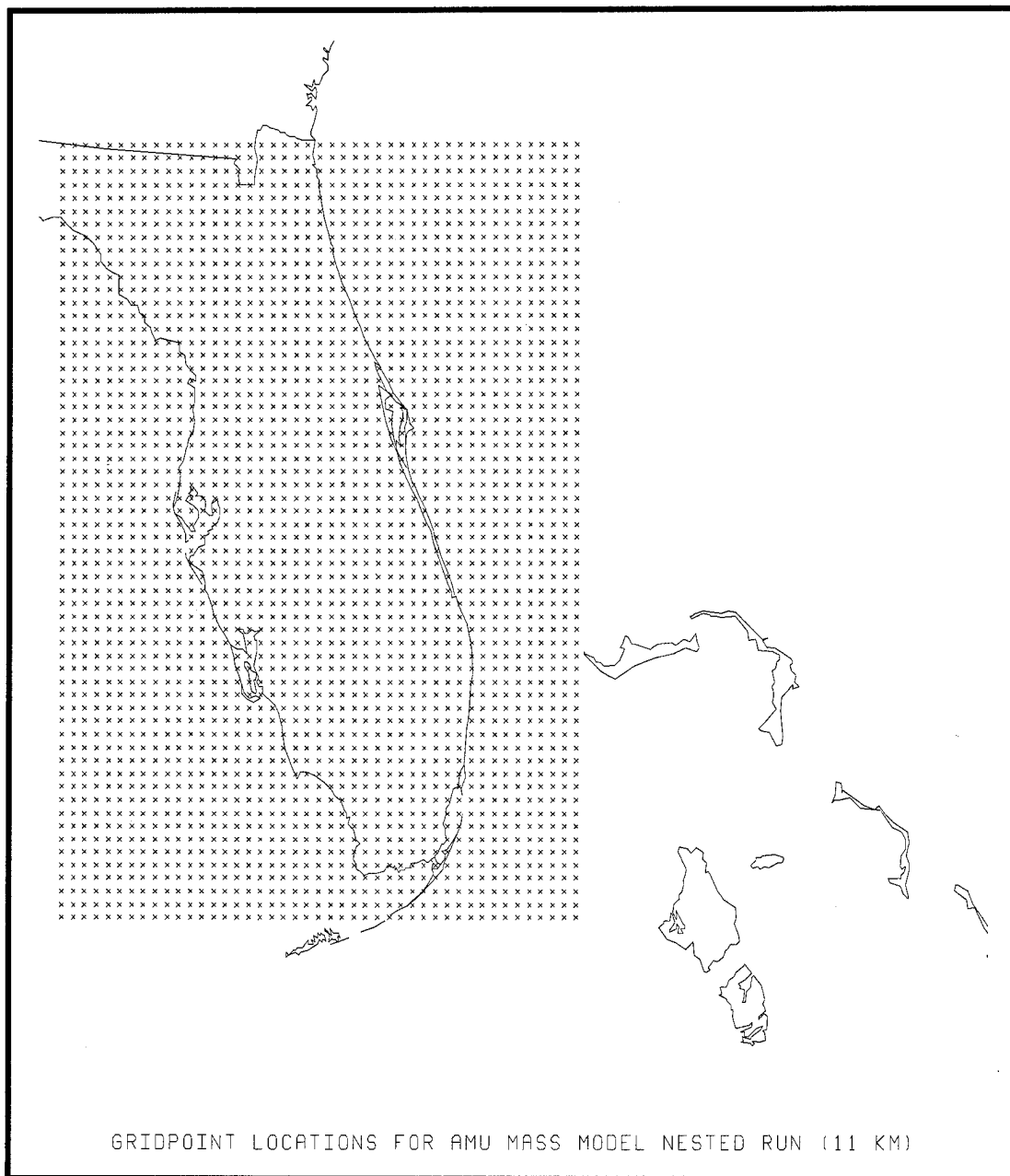


Figure 4.3. AMU nest grid covering most of Florida Bahama Islands with a horizontal grid resolution of 11 km.

Operationally, the AMU uses the operational Nested Grid Model (NGM) as the first guess data source and boundary condition source. The operational NGM has 80 km horizontal grid resolution with data available to 50 mb. For this research, archived Global Optimum Interpolation (GOI), with (2.5° x 2.5°) resolution, was used as the first guess data source and boundary condition source. Archived NGM data with 190 km horizontal grid resolution was not used because the data was only available up to 300 mb and was not suitable as a first guess data source nor boundary condition source. The other data sources used were the same as the AMU and included National Meteorological Center TTAA/TTBB/PPBB format rawinsondes and surface observations (consisting of MIDDs land report format conventional hourly surface observations, KSC tower mesonet, and KSC buoy and ship report format).

Two changes to the model parameters that differ from the AMU setup were the inclusion of high resolution (9 km) weekly averaged sea surface temperatures (SST) and the use of prognostic moisture physics in the microphysics scheme (the AMU uses diagnostic moisture physics due to computational restrictions). If any of the high resolution SST data were missing, then the climatological SST data were used in their place. In the diagnostic moisture scheme, no liquid or frozen water is retained in the atmosphere while the prognostic moisture scheme incorporates prediction equations for cloud water and cloud ice and rain water and snow. The prognostic moisture scheme models the atmospheric water cycle in greater detail than the diagnostic moisture scheme but is much more computationally intensive.

4.4 Coarse Grid Simulation Results

One coarse grid simulation was run for each of the four days. The initialization time was 0000 UTC and the model ran for 24 hours with output at 1 hour intervals. The analysis of model output concentrated on 1200 UTC each day to match the observational analyses times. A series of upper-level and surface maps were produced and compared to the analyses. The model surface analyses (Figs. 4.4a, b, c, and d) were compared to the surface analyses shown in Fig. 2.3. MASS clearly builds the surface high pressure ridge westward as in the analysis and develops a closed high by 1200 UTC 22 July (Fig. 4.4d).

MASS does a good job representing the geopotential height field at 700 mb (Figs. 4.5a, b, c, and d) compared to the 700 mb analyses shown in Fig. 2.4. Anticyclonic curvature prevails over Florida with the ridge axis slowly migrating northward until a closed high develops at 1200 UTC 21 July (Fig. 4.5c). Similarly to the analyses, heights from the MASS output rise an average of 40 m over the southeast United States through the period. This height increase is consistent with development of regional low-level divergence which helps to suppress convection later in the period. There is some difference between the analyses and the MASS output that can be seen in the relative humidity. Areas of high relative humidity ($> 70\%$ shaded in both sets of figures) are more prevalent in the MASS output, but careful inspection reveals the basic patterns of relative humidity on all four days matches well. However, the observed data

analyses and the MASS output from the coarse grid suffers from a lack of data correctly show the water vapor distribution which resulted in the different weather at KSC on each day.

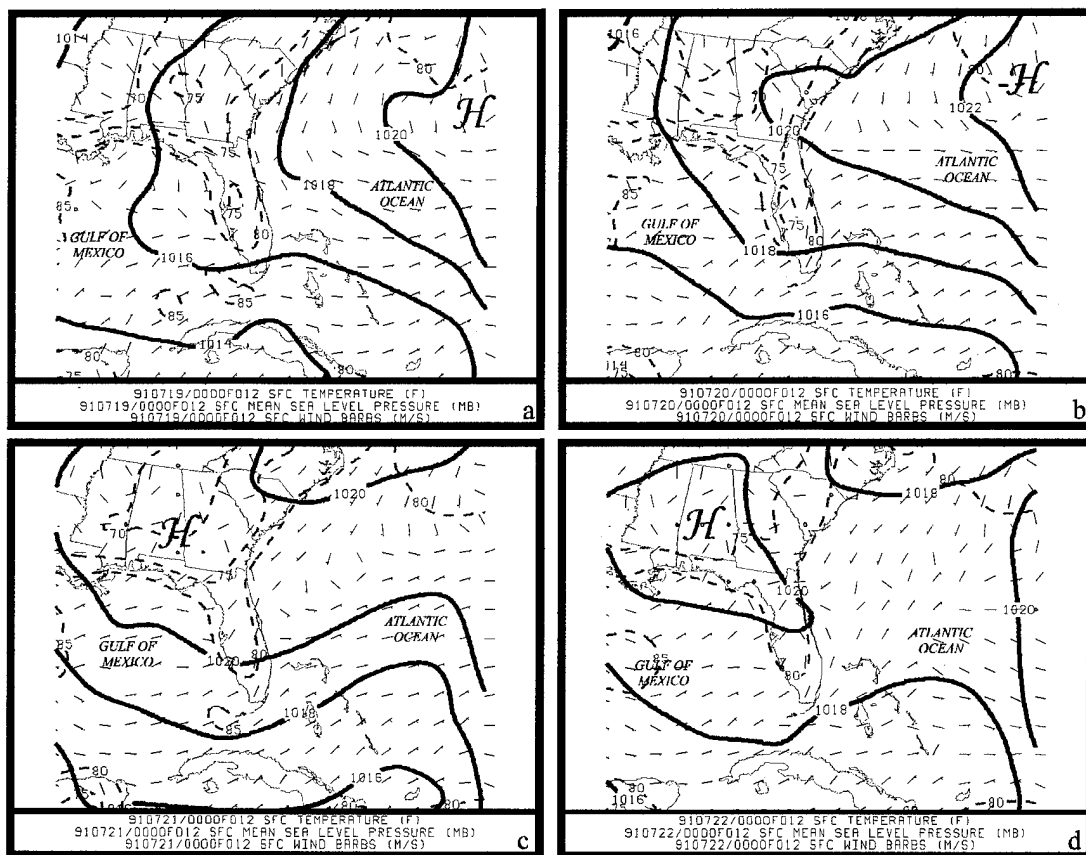


Figure 4.4. MASS surface 12 h forecasts from the coarse grid (45 km) for (a) 1200 UTC 19 July 1991, (b) 1200 UTC 20 July 1991, (c) 1200 UTC 21 July 1991, and (d) 1200 UTC 22 July 1991. Solid contours denote mean sea level pressure at 2 mb intervals. Dashed contours denote temperature at 5 °F intervals. Wind barbs indicate a half (full) barb equals 5 ms⁻¹ (10 ms⁻¹).

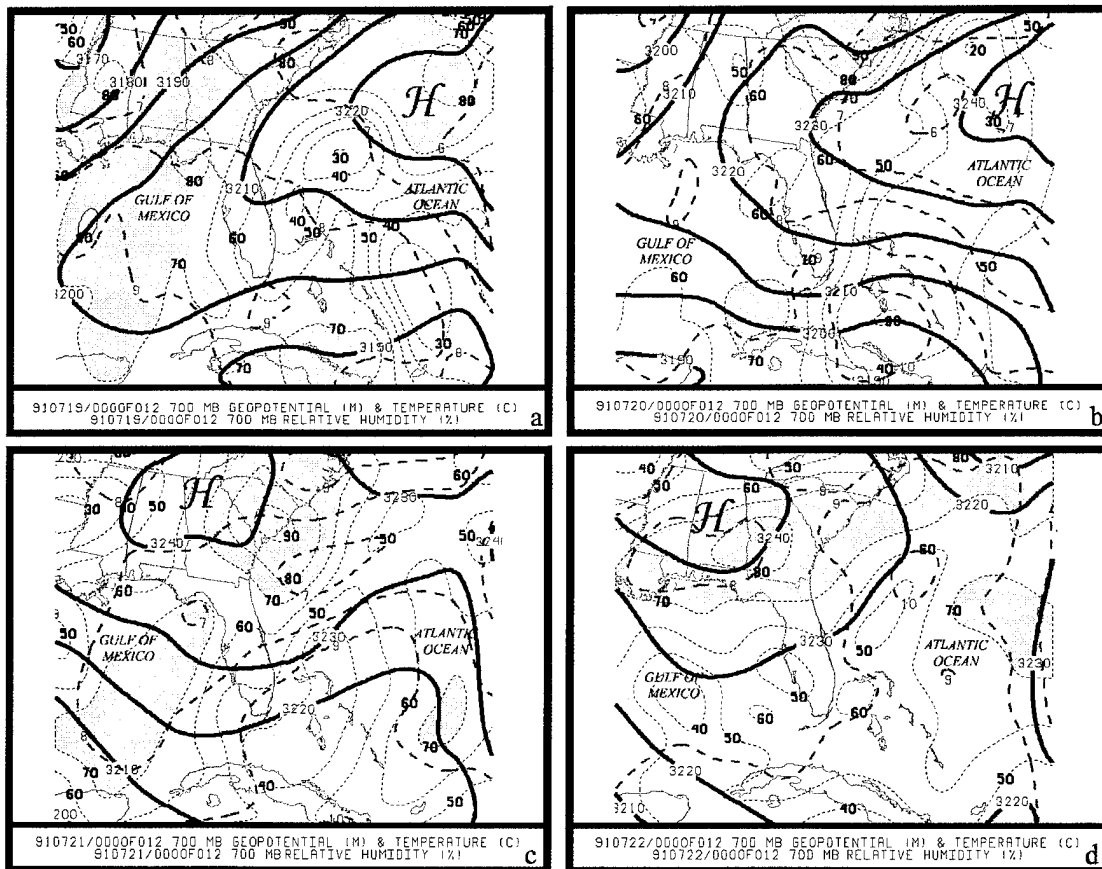


Figure 4.5. MASS 700 mb 12 h forecasts from the coarse grid (45 km) for (a) 1200 UTC 19 July 1991, (b) 1200 UTC 20 July 1991, (c) 1200 UTC 21 July 1991, and (d) 1200 UTC 22 July 1991. Solid black contours denote geopotential heights at 10 m intervals. Dashed red contours denote temperature at 1 °C intervals. Wind barbs indicate a half (full) barb equals 5 ms⁻¹ (10 ms⁻¹). Dashed thin black lines show relative humidity at 10% intervals and areas > 70% are shaded green.

At 150 mb, the general position of the 150 mb tropical upper-tropospheric trough (TUTT) was simulated well by MASS. The cold low associated with the TUTT

was placed too far north by MASS on 19 July (Fig. 4.6a). The diffluent area over northern Florida and southern Georgia should have been over central Florida as shown in the 150 mb analysis (Fig. 2.5a). The error in correctly positioning the low may have resulted in an incorrect simulation of the omega fields generated by MASS which will be shown in the vertical cross sections. On 20 and 21 July (Figs. 4.6b and c), the low position was well simulated as it moved through the Bahama Islands. More importantly, the position of the jet streak is very good at these times and helps explain the dynamics controlling the patterns of convection. On 22 July (Fig. 4.6d), MASS placed the low too far north and west of the analyzed position and resulted in the jet streak farther north and west than in the analysis. But the position of the jet streak was in enough agreement with the analysis to show confluent regime in the KSC vicinity in the left entrance region of the jet streak. The jet streak which developed in northern Florida on 21 and 22 July was captured well by MASS (Figs. 4.6c and d). The geopotential height gradient from the model output matched the analyses very well and hence, the model developed a 20 ms^{-1} jet streak appropriately. The jet dynamics and the movement of the cold low throughout the model simulations depicts the change from 150 mb divergence early in the period to convergence later. The upper-tropospheric divergence pattern on 20 July shows divergence at 150 mb close to the jet streak left exit region in the KSC vicinity (Fig 4.7a). In contrast, the suppressed day (21 July) shows convergence in the KSC vicinity associated with the left entrance region of the jet streak (Fig. 4.7b).

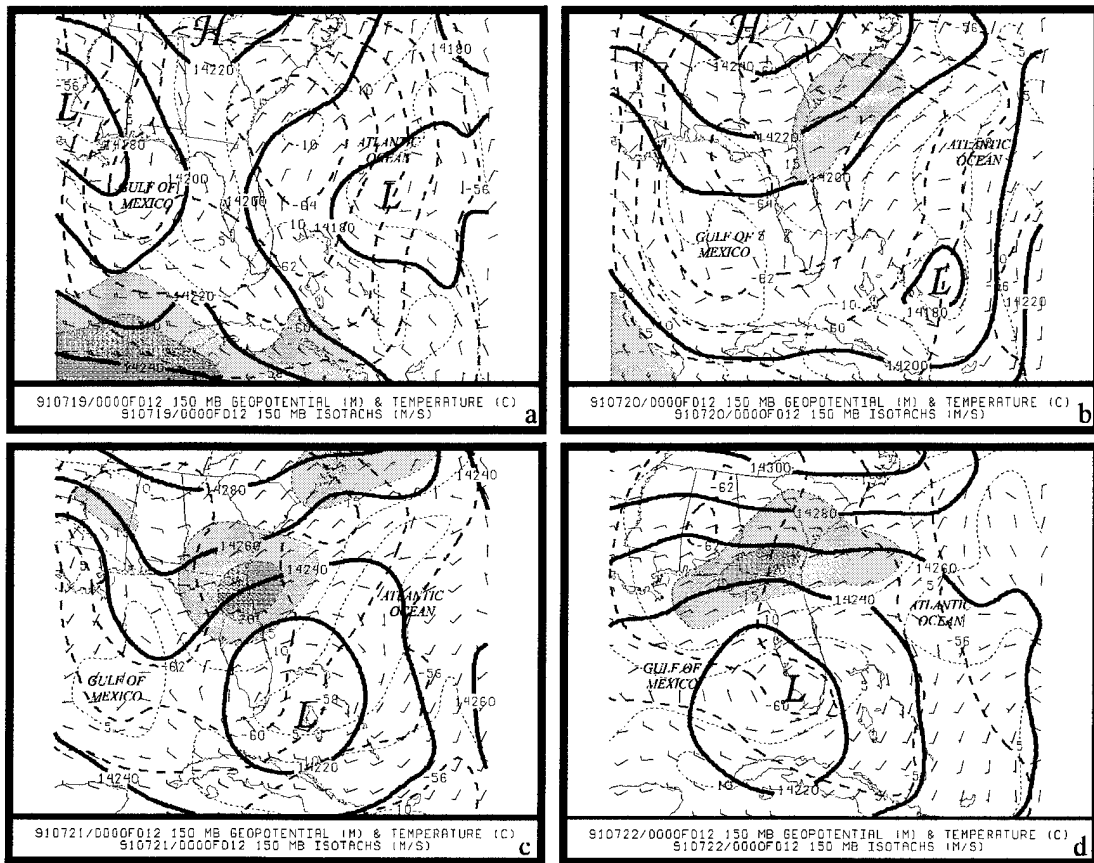


Figure 4. 6. As in Fig. 4.5 except for 150 mb depicting isotachs (ms^{-1}) shaded at 5 ms^{-1} intervals beginning at 15 ms^{-1} and solid contours denoting geopotential heights at 20 m intervals.

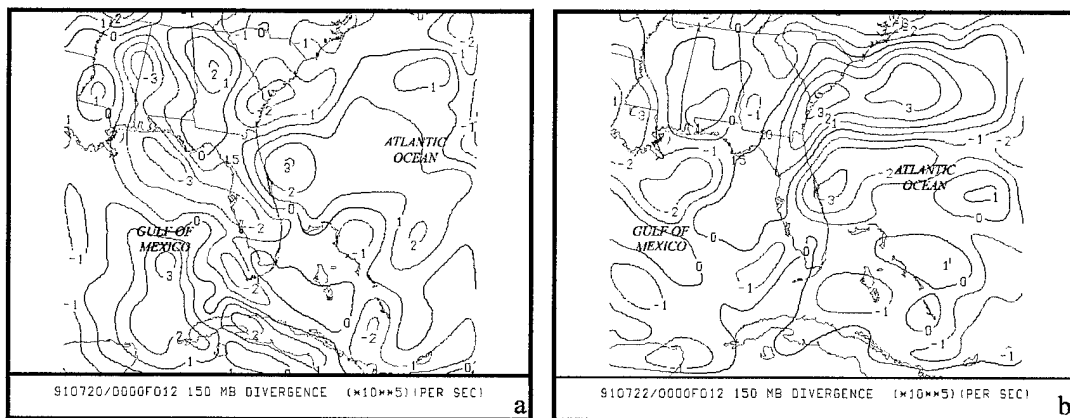


Figure 4. 7. As in Fig. 4.6 but showing divergence (10^5 s^{-1}). Red contours denote divergence and blue contours denote convergence.

The jet streak dynamics simulated by MASS and discussed in Section 2.4 (Data Analysis) can be investigated by looking at vertical cross sections orthogonal to the jet as it develops and moves westward across Florida. The cross sections were taken from Athens, GA (AHN) to West Palm Beach, FL (PBI) and the cross section line is shown on the coarse grid in Fig. 4.1. The cross section for 19 July (Fig. 4.8a) shows little organization to the circulation and no jet streak is evident. On 20 July (Fig. 4.8b), the cross section shows the jet entrance region centered at 200 mb over Jacksonville, FL (JAX). The ageostrophic motion is rightward (northward) directed in the upper troposphere as expected in this region of the jet streak. The transverse circulation throughout the troposphere shows downward vertical motion near AHN associated with the right exit region of the jet and upward vertical motion from KSC south to PBI in the left exit region of the jet. The position of the jet streak and transverse circulation support the convection observed on 20 July. On 21 July, the center of the jet streak is located between KSC and JAX (Fig. 4.9a). The jet exit region is now west of KSC and the entrance region is east of KSC. The KSC weather was defined as passive since weak convection was observed early in the morning giving way to more suppressed conditions later in the morning. The transition of the weather from active to suppressed closely parallels the movement of the jet streak across the KSC area. By late morning, KSC weather was beginning to be influenced by the left entrance region of the jet streak (cyclonic side) resulting in upper-level convergence and downward motion south of the jet streak. By 22 July, the KSC area weather is completely under the influence of the left

entrance region of the jet streak as it has moved north of JAX (Fig. 4.9b) and into northern Florida and Georgia (see Fig. 4.6d). The transverse circulation shows leftward (southward) directed motion in the upper troposphere and a return flow northward at lower levels. The MASS coarse grid vertical cross sections support the analysis and jet streak model previously discussed and indicate the model captured the dynamics very well.

As shown in the observational analysis, water vapor distribution is related to the large scale dynamics and low-level wave-CISK instability was an available trigger mechanism each day. The water vapor distribution probably played an instrumental role in the convective activity each day. The resulting observed convective rainbands had wavelengths on the order of 14 km to 20 km which is too small for the MASS coarse grid to resolve. So, a higher resolution nest was run to evaluate the capability of MASS to simulate water vapor distribution.

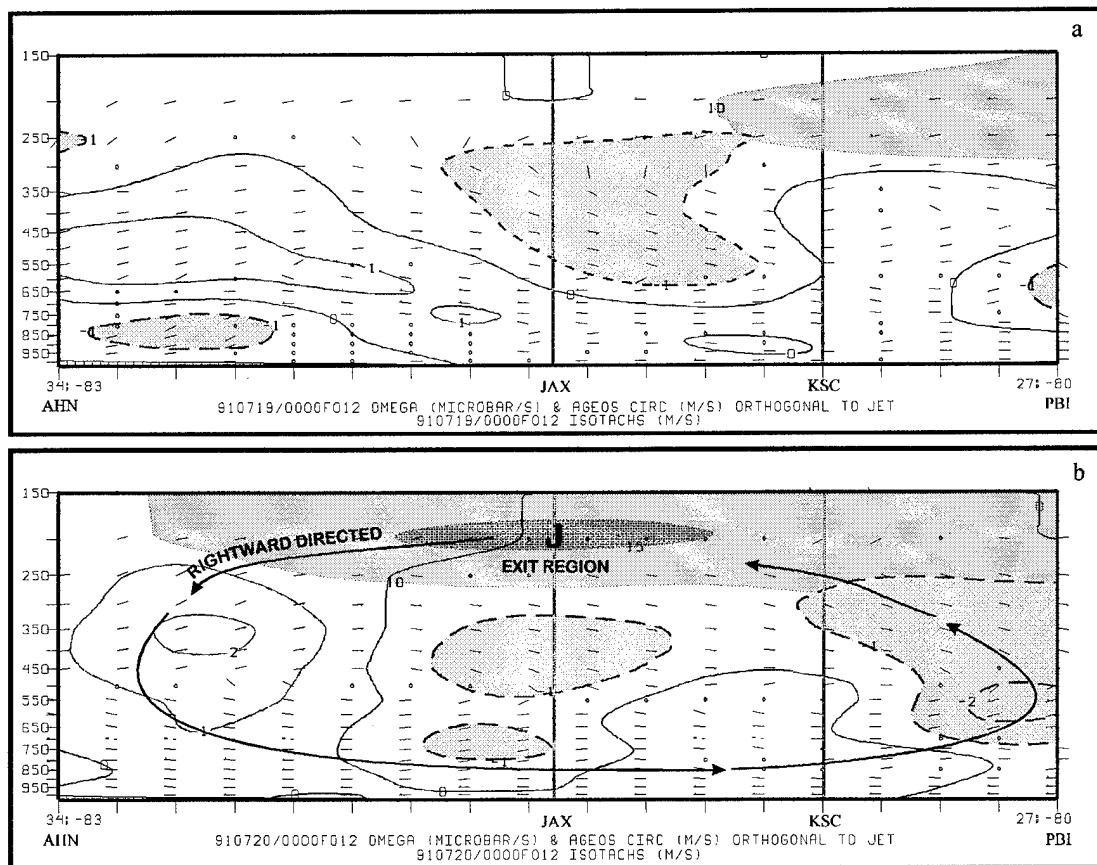


Figure 4.8. MASS coarse grid 12 h forecasts of vertical cross sections for (a) 1200 UTC 19 July 1991 and (b) 1200 UTC 20 July 1991. The cross sections were taken from Athens, GA (AHN) to West Palm Beach, FL (PBI) orthogonal to the 150 mb jet streak. Red shaded areas show areas of negative kinematic omega (upward motion) and the solid blue lines indicate areas of positive kinematic omega (downward motion). Isotachs are shaded in gray every 5 ms^{-1} beginning at 10 ms^{-1} and they indicate flow out of the page. Wind barbs indicate the cross stream ageostrophic circulation where a half (full) barb equals 5 ms^{-1} (10 ms^{-1}). Solid black lines with arrows indicate general circulation pattern. Large "J" shows location of wind maximum.

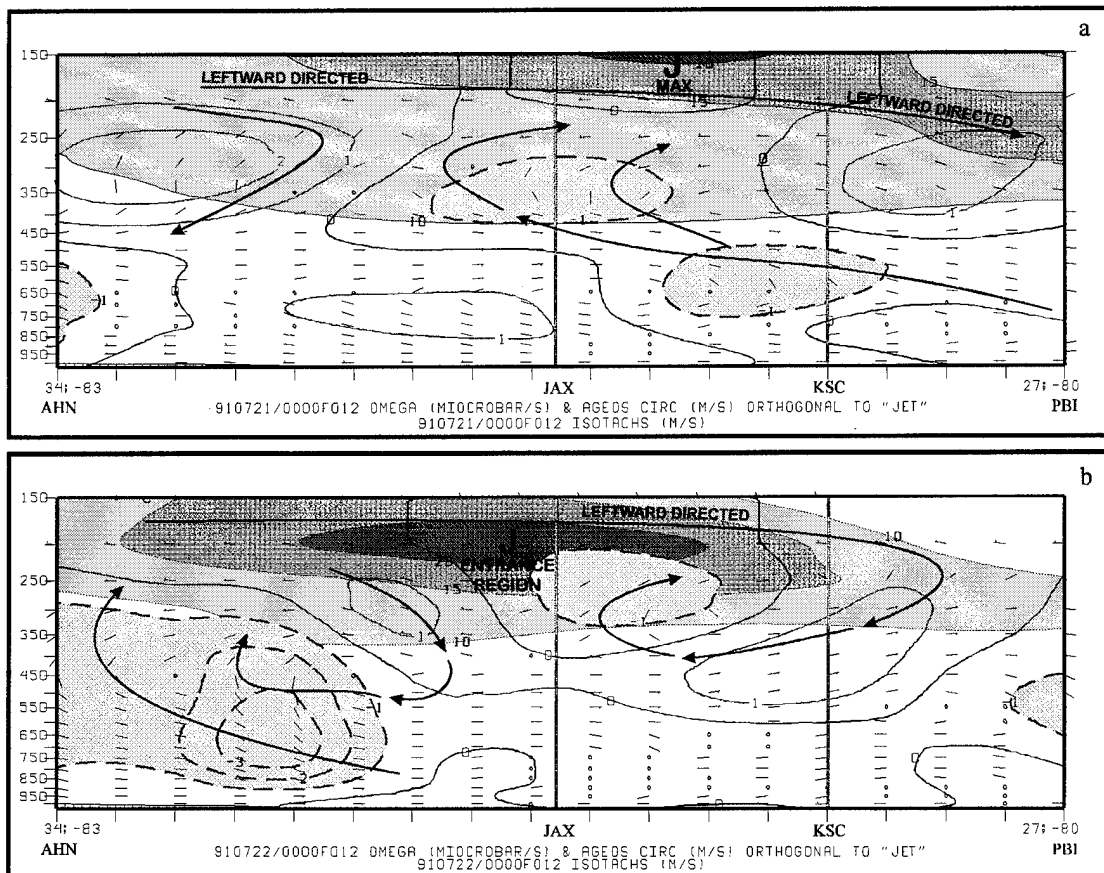


Figure 4.9. As in Fig. 4.8 except for (a) 1200 UTC 21 July 1991 and (b) 1200 UTC 22 July 1991.

4.5 Nested Grid Simulation Configuration

The nested MASS grid was run with 11 km horizontal resolution with 22 vertical sigma levels (identical to the AMU coarse setup). The nested simulations were run six times for each of the four days to determine if they could duplicate the water vapor distribution observed in the analyses. The MASS coarse grids were used as the first guess fields for the 24 nested simulations. The main differences between setup of the

AMU nest and the NCSU nest were the grid domain size (Figs. 4.3 and 4.2, respectively) and the use of high resolution (9 km) SST in this research. Because onshore flow is the focus of this work, the nested grid was expanded eastward by 297 km and southward by 77 km and reduced on the west side by 66 km and the north side by 22 km (Fig. 4.2). The grid domain was 66 x 66 grid points (in x and y) compared to 55 x 50 grid points used by the AMU. The initialization time was 0600 UTC and the model ran for 12 hours with output at 1 hour intervals. The analysis of model output concentrated on 1200 UTC each day to match the observational analyses times and the coarse grid analysis. The initialization data sources were the same as the coarse grid except rawinsonde data was not included since none was available at 0600 UTC.

4.6 Nested Grid Dynamics

Vertical cross sections were constructed from the nested grid similar to those from the coarse grid to determine if the higher resolution grid could show the structure of the rainbands and the mesoscale dynamics acting to enhance or suppress the convection. The cross sections were taken approximately orthogonal to the rainbands from near Jacksonville, FL (JAX) through KSC and Patrick Air Force Base (COF) to just west of the Bahama Islands and the cross section line is shown on the NCSU nested grid in Fig. 4.2.

The MASS nested grid 6 h forecast vertical cross section for 1200 UTC 19 July (Fig. 10a) shows little organization in the circulation and vertical motion fields. As in

the coarse grid simulation and observational analyses, the upper level jet streak has not developed at this time and probably accounts for the lack of widespread convection. Visible satellite imagery for this time (Fig. 4.11) shows a few convective showers southeast of KSC that are beginning to organize into rainbands parallel to the wind shear in the rainband layer. The infrared (IR) satellite image from 1200 UTC (Fig. 4.19a) provides a wider view of the area and the general lack of organization of convection between Florida and the Bahama Islands. As shown in the analysis, wave-CISK was a likely trigger mechanism in the low-levels which initiated convection on this day and aligned the rainbands as previously discussed. However, as shown in the cross section (Fig. 4.10a) the upper level dynamics were weak (which agrees with the analyses and coarse grid output) and the convection on this day was relatively weak. Of the two convectively active days, this was the weakest with a more random distribution of the convection. The nested grid omega shown in the cross section is relatively weak with a rather random pattern of upward and downward vertical motion which generally agrees with the convective pattern seen in the satellite image.

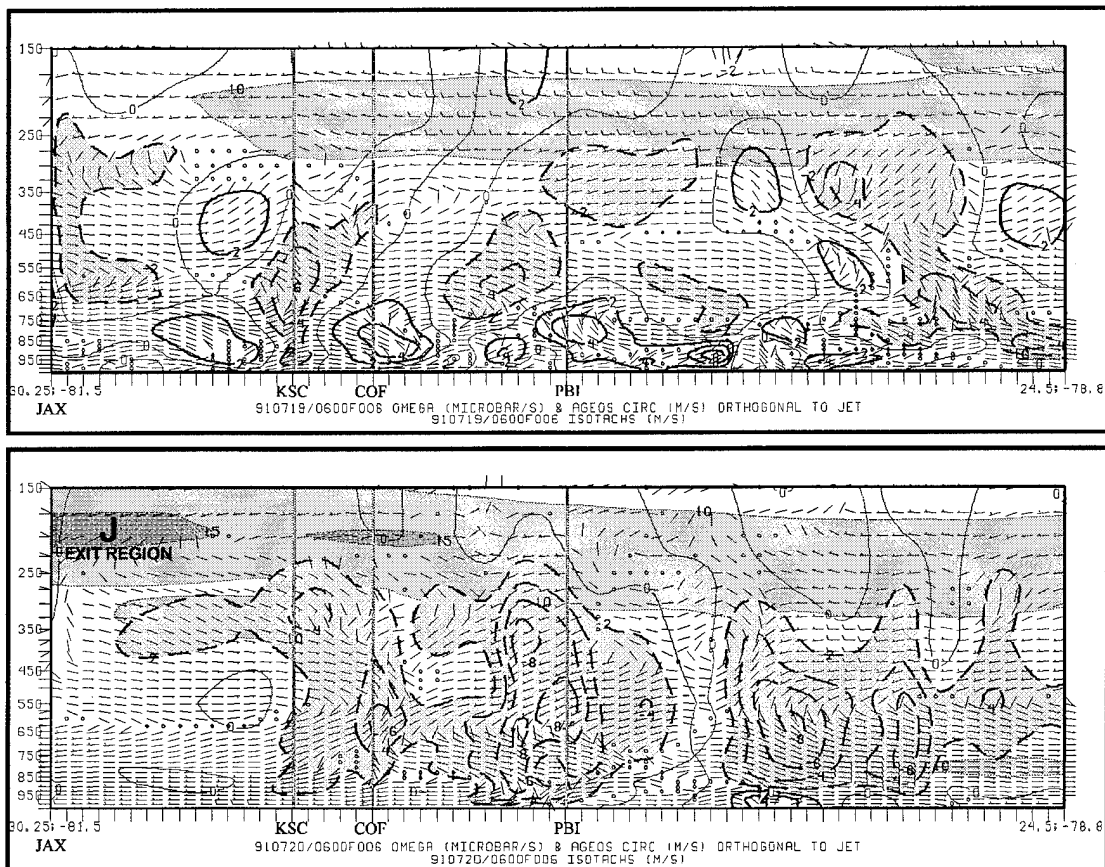


Figure 4.10. MASS nested grid 6 h forecasts of vertical cross sections for (a) 1200 UTC 19 July 1991 and (b) 1200 UTC 20 July 1991. The cross sections were taken from Jacksonville, FL (JAX) through KSC, Patrick Air Force Base (COF), and West Palm Beach, FL (PBI) to just west of the Bahama Islands orthogonal to the 150 mb jet streak and convective rainbands. Red shaded areas show areas of negative kinematic omega (upward motion) and the solid blue lines indicate areas of positive kinematic omega (downward motion). Isotachs are shaded in gray every 5 ms^{-1} beginning at 10 ms^{-1} and they indicate flow out of the page. Wind barbs indicate the cross stream ageostrophic circulation where a half (full) barb equals 5 ms^{-1} (10 ms^{-1}). Large “J” shows location of wind maximum.

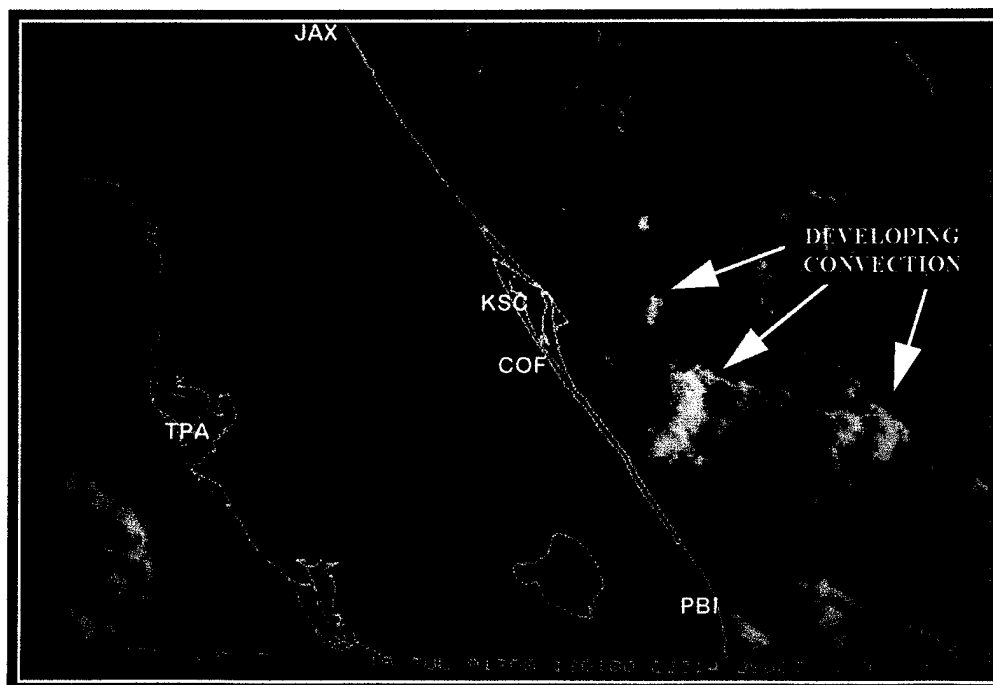


Figure 4.11. Visible satellite imagery (1 km horizontal resolution) from GOES-7 for 1201 UTC 19 July 1991.

More organized convection developed on 20 July and the MASS nested grid 6 h forecast vertical cross section for 1200 UTC shows the strongest upward vertical motion is located under the left exit region of the now developed jet streak as shown in the observational analyses, coarse grid simulation, and now the nested grid simulation (Fig. 4.10b). The upward vertical motion is the strongest and deepest at this time compared to the other three days and appears organized with a banded structure. The visible satellite imagery (Fig. 4.12) shows four developing convective rainbands. One is just northeast of KSC, one offshore and adjacent to COF, and two other southeast of COF. Although the wavelength of the rainbands simulated by MASS is not identical to those

seen in the satellite image, the model still does a good job indicating the existence of the rainbands through the vertical motion fields. Furthermore, the vertical cross section indicates a substantial region of upward vertical motion south of PBI which is most likely associated with the area of convection that can be seen on the IR satellite image (Fig. 4.19b). The cross section shows the jet streak in about the same position as the coarse grid simulation (near JAX and at about 200 mb). Although the flow is disrupted by the vertical motions, it is still generally leftward throughout the jet-level region that indicates divergence at the upper levels enhancing convection that was most likely triggered by the low-level wave-CISK.

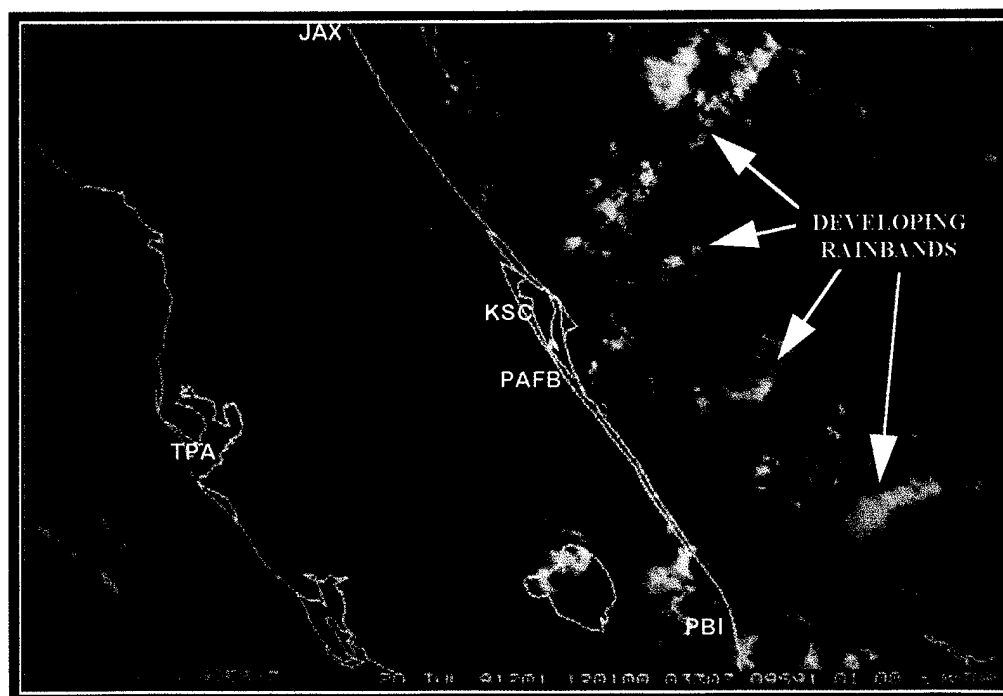


Figure 4.12. As in Fig. 4.11 except for 1200 UTC 20 July 1991.

On 21 July, the convection was considerably weaker than either 19 or 20 July. One rainband developed near and offshore COF and moved into the KSC vicinity about 1500 UTC. The MASS nested grid 6 h forecast vertical cross section for 1200 UTC 21 July (Fig. 4.13a) shows the center of the jet streak has propagated to northeast Florida (Fig. 4.6c). The weather in KSC vicinity is transitioning to a more suppressed state due to the influence of the left entrance region of the jet streak. During this transition, convection in the KSC vicinity is most likely to occur before the arrival of the jet streak left entrance region. The satellite image for this time (Fig. 4.14) shows some small showers north of KSC but in much of the region convection is suppressed except for the low-level Rayleigh-Bernard cells in the boundary layer. The small convective rainband that moves into the KSC vicinity about 1500 UTC quickly dissipates at that time and convection offshore and near KSC is suppressed for the rest of the day. Some weak convection is evident south of PBI in and between the Bahama Islands and southeast Florida (Fig. 4.19c) that may be related to the weak area of upward vertical motion shown in the vertical cross section south of PBI.

On 22 July, the MASS nested grid 6 h forecast vertical cross section for 1200 UTC the jet streak at about 200 mb (Fig. 4.13d) and can be seen in northwest Florida at 150 mb (Fig. 4.6d). The jet streak entrance region is now affecting the KSC weather by producing upper level convergence and subsidence. Although little downward vertical motion is seen in the cross section, the upward vertical motion is considerably weaker than on previous days and covers a much smaller area. The visible satellite image for

this time (Fig. 4.15) shows only the Rayleigh-Bernard boundary layer convection present with the suppressed conditions. The strongest upward motion is at the southern most part of the cross section where strong thunderstorms were occurring at this time (Fig. 4.19d) and were associated with the upper-level cold-core low.

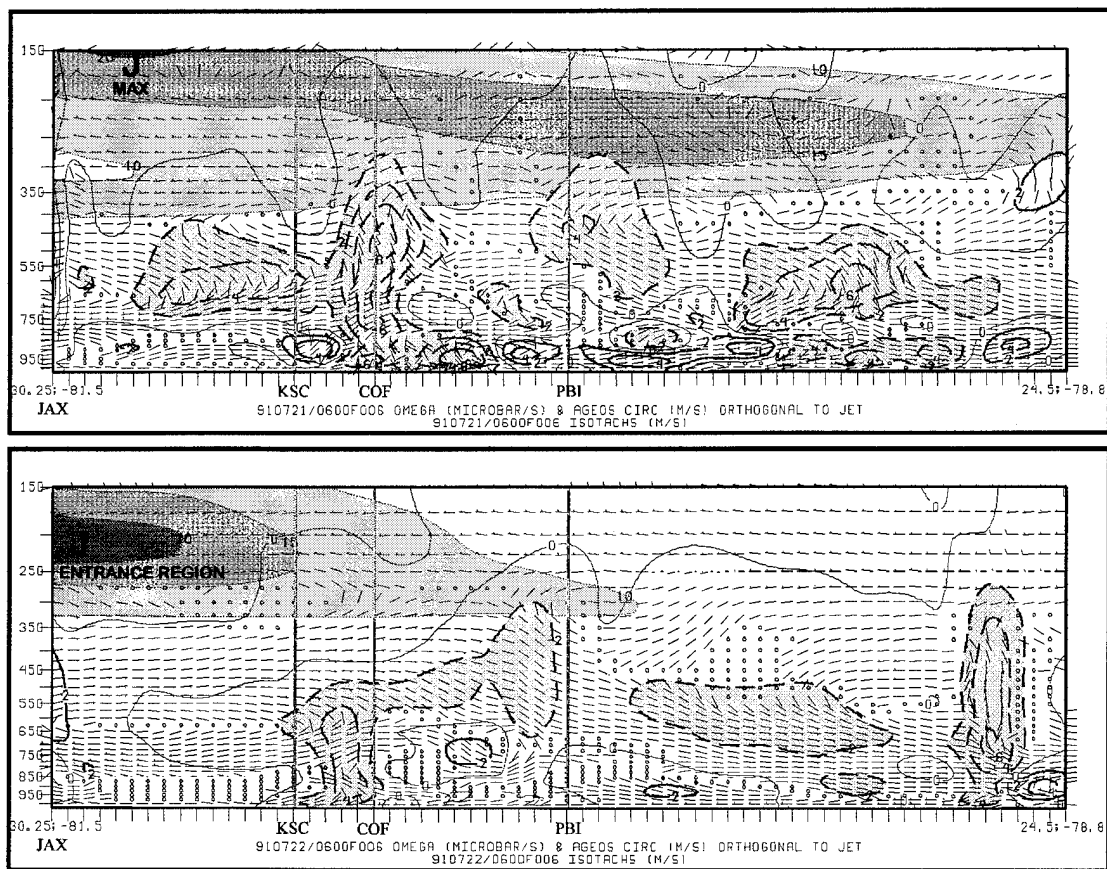


Figure 4.13. As in Fig. 4.10 except for (a) 1200 UTC 21 July 1991 and (b) 1200 UTC 22 July 1991.

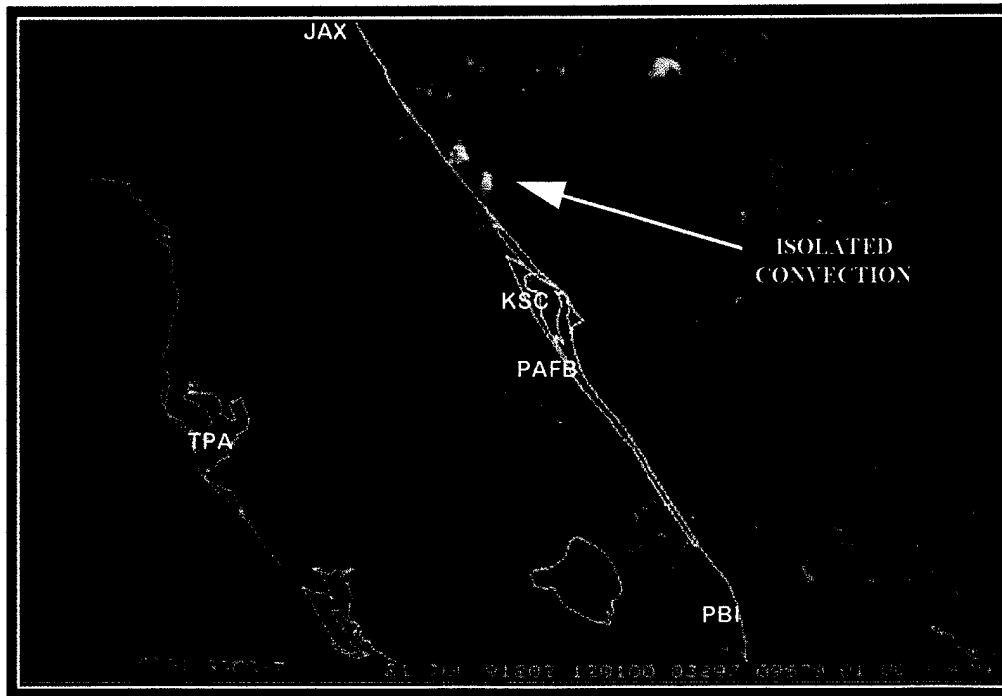


Figure 4.14. As in Fig. 4.11 except for 1200 UTC 21 July 1991.

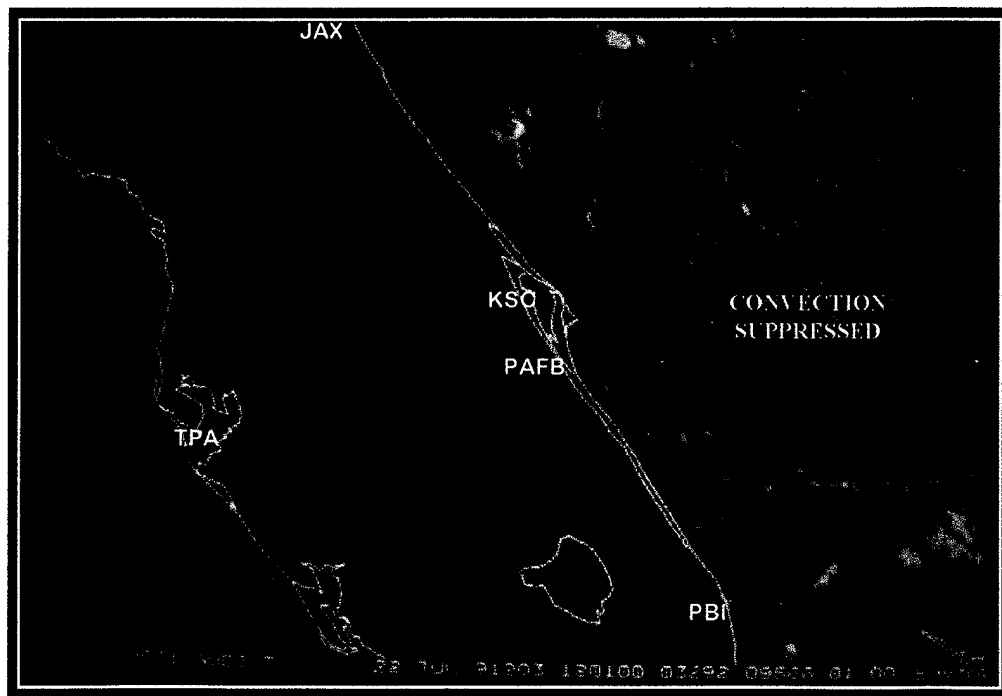


Figure 4.15. As in Fig. 4.11 except for 1200 UTC 22 July 1991.

4.7 Nested Grid Moisture Enhancement Sensitivity Studies

Rawinsonde observations are normally the prime source of water vapor measurements ingested into numerical models. These observations are of poor quality for initialization of a mesoscale model. First, the horizontal spacing between rawinsonde observations averages about 400 km while most mesoscale models have a horizontal resolution on the order of tens of km. Second, accurately measuring the relative humidity at a particular level depends on whether the sonde passes through a cloud or an adjacent cloud-free region. Third, rawinsonde moisture sensors can have a slow response to saturated layers that leads to an underestimation of relative humidity. Finally, rawinsondes can underestimate moisture when areas of small scale precipitation (convection) are located between rawinsonde release sites.

The representation of relative humidity in MASS is critical for determining how well the model can forecast water vapor distribution during onshore flow. Since rawinsonde data is not a sufficient source of moisture for MASS, the model allows for enhancement of synthetic moisture in the initialization. The MASS synthetic relative humidity scheme (MESO, Inc. 1995) allows for enhancement of manually digitized radar data, satellite imagery, and visual observations of clouds (surface observations). Since these synthetic sources of data do not measure or report relative humidity values, the vertical profile of relative humidity must be inferred at a given location. This information is then used to enhance the rawinsonde data for use in the model.

To insert these moisture sources into MASS, one of the MASS modules ingests a model-ready initialization file and changes the relative humidity field based on the information inferred from the three sources of moisture data. The module then outputs a new initialization file containing the updated relative humidity fields but leaves all other variables unchanged.

4.7.1 Enhancement with Manually Digitized Radar (MDR)

When the manually digitized radar (MDR) data is enhanced into MASS the areal coverage reported by each radar site and the echo level are analyzed onto the model grid. Gridded analyses of areal coverage of precipitation and the radar VIP levels (National Oceanic and Atmospheric Administration 1982) provide estimates of rainfall rates for MASS. The VIP levels are assigned a value at the nearest MDR grid point (having 40 km horizontal resolution). To help reduce the spreading of isolated convection on the grid and before the values are assigned to the MASS grid, the data is processed to set $VIP = 0$ when VIP levels ≤ 2 surround convective cores with $VIP \geq 4$ and are adjacent to a grid point with $VIP = 0$. To estimate cloud tops when infrared satellite imagery data is unavailable, MASS will use the MDR data and the relationship:

$$\sigma_{top} = 0.7 - 0.11(VIP)^{0.91} \quad (4.2)$$

where σ_{top} is the top of the model domain or 100 mb (MESO, Inc. 1995).

4.7.2 Enhancement with Infrared Satellite Imagery

The infrared (IR) satellite imagery is used to determine the amount of cloud cover in each grid box. The scheme incorporated in MASS is a simplified version of the one used by Hamill et al. (1992) where a cloud is detected if:

$$\Delta T_{obs} = T_{clr} - T_{obs} \geq T_{thresh} \quad (4.3)$$

where T_{clr} estimates the temperature which the satellite would observe under clear skies, T_{obs} is the IR temperature the satellite observes, and T_{thresh} is an uncertainty in the estimate of T_{clr} and because T_{obs} is likely to be large when clouds are present in a relatively dry, unstable atmosphere (MESO, Inc. 1995). With use of the IR data, the height of the top-most cloud layer is calculated by matching cloud top temperatures with atmospheric temperatures from the rawinsonde analysis. The cloud base in one of two ways. If surface data is available and the cloud coverage is $\geq 80\%$, MASS assumes the cloud base coincides with the highest broken or overcast cloud base at the nearest surface station. If surface data is unavailable or cloud coverage is $< 80\%$, MASS assumes the cloud base to be 500 m below cloud top (MESO, Inc. 1995). The satellite imagery can also dry cloud-free areas. This is a critical procedure that significantly affected the results of moisture enhancement in this work and will be discussed later. The maximum relative humidity is set to 75% above cloud tops. Any point where the satellite determined cloud fraction is $< 100\%$ but $> 5\%$ the relative humidity at any given level cannot exceed the value calculated from:

$$RH = \frac{(3.0 + C^{0.33})}{4.0} \quad (4.4)$$

where C is the areal cloud coverage (between 0 and 1.0) and RH is the relative humidity ($RH = 1$ at saturation). At any point having a satellite-determined cloud fraction of $< 5\%$, the relative humidity at any given level cannot exceed the mean plus one standard deviation of the relative humidity from the clear skies category in the statistical database (MESO, Inc. 1995). The final part of the satellite data enhancement is a scheme after Adler and Negri (1988) to locate convective towers. This scheme in MASS finds all of the IR temperature minima and then calculates a slope parameter for each. Each convective tower is assumed to represent a 64 km^2 saturated region.

4.7.3 Enhancement with Surfaced Based Observations

Surface observations are placed into cloud/weather categories based on the height of each cloud layer, the cloud coverage, and the preceding hours' weather. Cloud bases < 1250 m above ground level are classified as low cloud, cloud bases ≥ 1250 m and ≤ 4700 m above ground level are classified as middle cloud, and cloud bases > 4700 m above ground level are classified as high cloud. The cloud coverage is classified as scattered, broken, or overcast. The weather is also classified into three categories: either precipitation, no precipitation, or fog. After the surface observation is classified, the relative humidity in a co-located sounding is interpolated to 32 levels starting at the surface and incremented every 25 mb. Datasets were created and used to derive the

statistical prediction equations of relative humidity values for each level in each cloud/weather category. A root mean square error is used to identify levels which have a satisfactory correlation and when the error is $< 15\%$, the levels meeting the criteria are blended into the rawinsonde analysis using the Barnes (1964) analysis scheme (MESO, Inc. 1995).

4.7.4 Moisture Enhancement of the NCSU Nest Grid

Sensitivity studies were conducted using the nested grid and were based on moisture enhancement from three different sources using five different schemes. First, a baseline nest was run using the AMU grid and parameters with no moisture enhancement. The baseline run was compared to a basic (no moisture enhancement) run using the NCSU nested grid which included high resolution (9 km) SST data. The AMU baseline run and the NCSU basic run water vapor distribution agreed quite well when comparing relative humidity and average convective precipitation output. Relative humidity at 700 mb was nearly identical over Florida but the AMU baseline missed some higher values just east of Florida, an omission that is probably due to smaller grid domain used in the AMU baseline. The AMU baseline run produced less precipitation (averaged over 6 h) than the NCSU basic run but generally placed it in the same region.

The rest of the NCSU nested runs consisted of adding one moisture source at a time to each simulation and then adding all moisture sources to the last simulation. The moisture sources that were introduced include the MDR data with 40 km resolution,

GOES-7 infrared satellite imagery with 4 km resolution, and cloud observations from conventional surface observations. Fig. 16a, b, c, and d shows the MDR data that was enhanced into the nest, Fig 17a, b, c, and d shows the satellite data, and Fig 18a, b, c, and d shows the surface observations.

To gauge the effects of moisture enhancement into MASS, the model-generated 700 mb 6h forecast of relative humidity (RH) was compared to the 4 km IR satellite images valid at the same time (not shown). Although comparing the 700 mb RH and IR satellite imagery is not the ideal way to evaluate the model forecast, it is the best method available since the 700 mb RH analyses are too coarse to show the small scale water vapor distribution from the MASS nested grid.

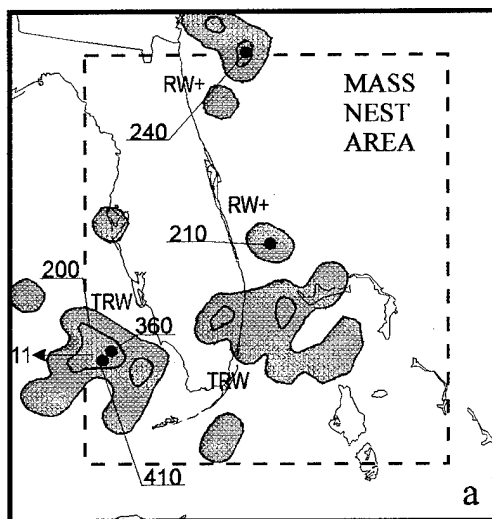
4.7.4.1 No Moisture Enhancement - Basic Run

The first nest was run without any moisture enhancement (basic run) and the 6 h forecast for 19, 20, 21, and 22 July (valid at 1200 UTC) is shown in Figs. 4.20a, b, c, and d. The only moisture sources for the basic run were from the MASS coarse grid first guess fields and the 0600 UTC surface observations (not the surface cloud observation scheme as previously described).

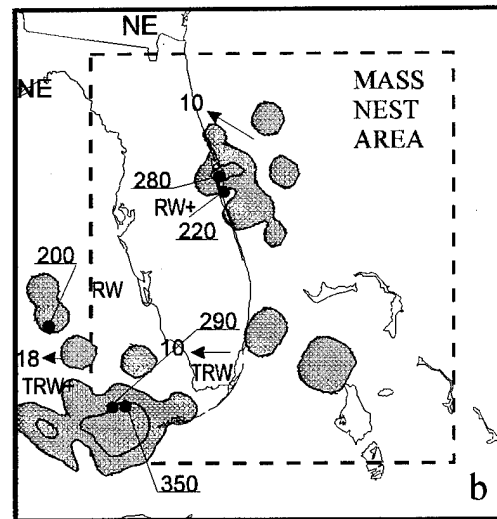
On 19 July, a region of convection can be seen in the satellite imagery from south of KSC to the Bahama Islands in Fig. 4.19a which is well represented by the high RH values in Fig. 4.20a in the same vicinity. Another convective area is seen in Fig. 4.19 southeast and south of Florida which the model represented quite well with the RH field. The satellite image also shows convection off the southwest coast of Florida which the model did not simulate in the RH field.

On 20 July, the developing rainbands of this active day in the KSC vicinity can be seen east of Florida in the satellite imagery (Fig. 4.19b). There is also convection south of West Palm Beach (PBI) and near Key West (EYW) off the southwest coast of Florida. The basic run (Fig. 4.20b) has high RH values associated with the rainbands near KSC and the convection off the southwest coast of Florida. The model did not simulate the high moisture south of PBI evident in the satellite imagery.

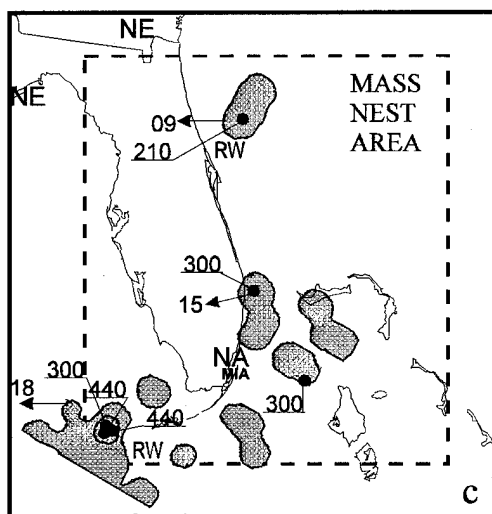
On 21 July, the satellite imagery reveals a general high moisture region in the southern part of the nest domain from the Bahama Islands westward to south of EYW (Fig. 4.19c). MASS did not simulate high moisture in the RH field anywhere in the southern part of the nest domain (Fig. 4.20c). MASS did produce high RH values along the Florida east coast near KSC and north of PBI. Although not resolvable by the satellite image, some very small showers occurred near Patrick Air Force Base around 1200 UTC which is just south of KSC and also just north of KSC.



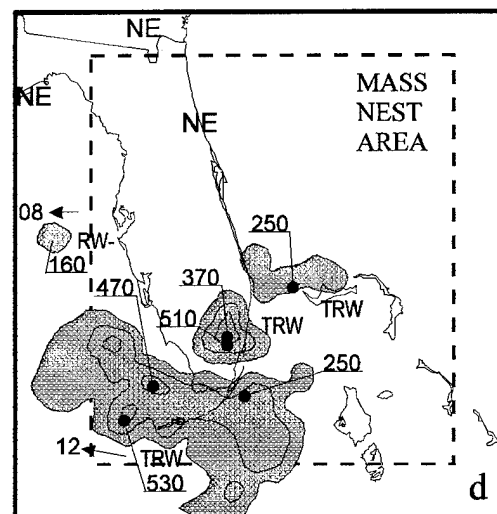
910719/0635 MANUALLY DIGITIZED RADAR



910720/0635 MANUALLY DIGITIZED RADAR



910721/0635 MANUALLY DIGITIZED RADAR



910722/0635 MANUALLY DIGITIZED RADAR

Figure 4.16. Manually Digitized Radar data with 40 km resolution enhanced into MASS NCSU nest run for (a) 0635 UTC 19 July 1991, (b) 0635 UTC 20 July 1991, (c) 0635 UTC 21 July 1991, and (d) 0635 UTC 22 July 1991. Nest grid domain is shaded light yellow. MDR reflectivity echoes gray shaded and outlined. MDR reflectivity echoes, tops, and movement as shown in National Weather Service Radar Code User's Guide, Federal Meteorological Handbook No. 7 (National Oceanic and Atmospheric Administration 1982).

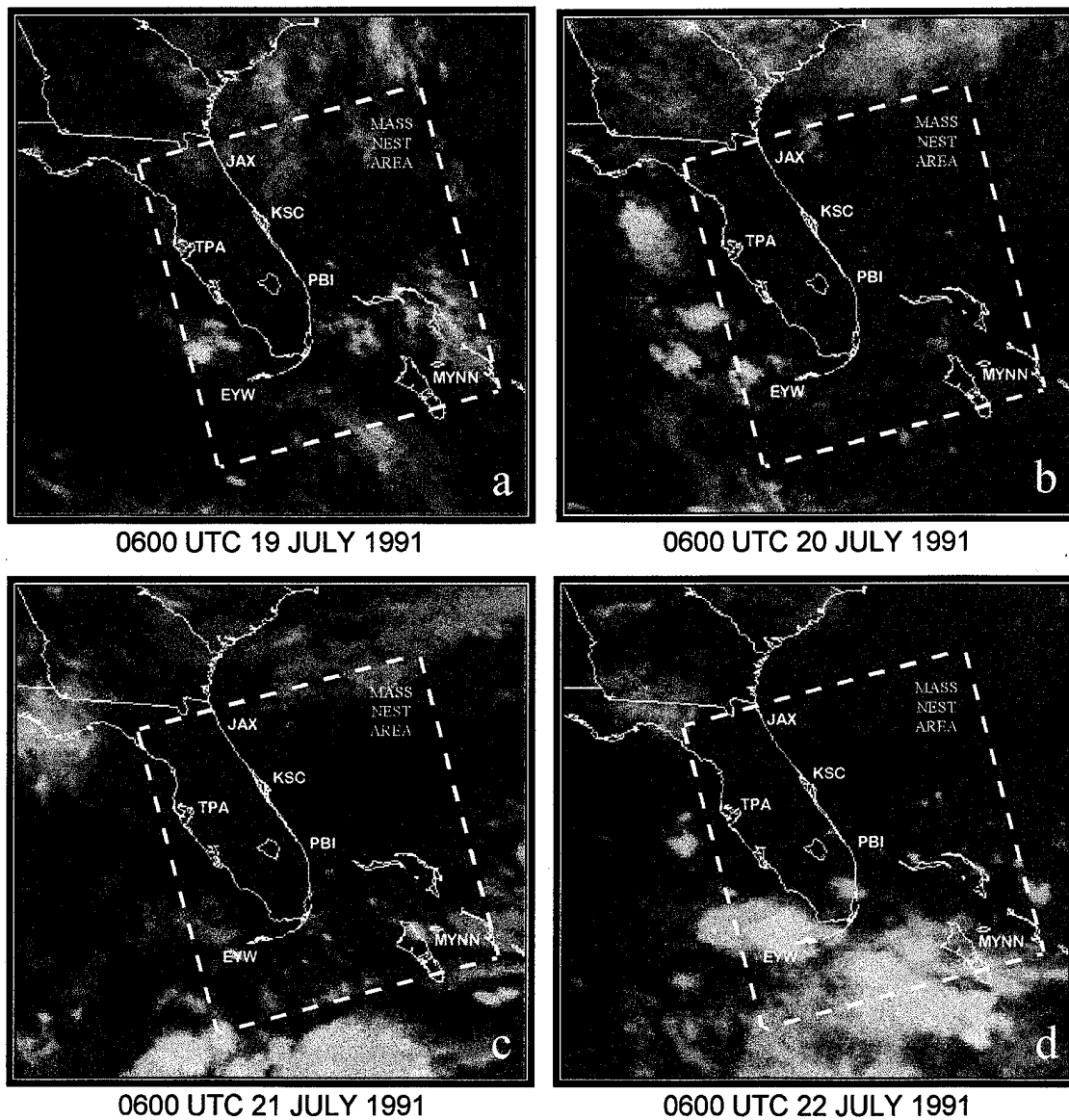


Figure 4.17. GOES-7 infrared satellite imagery with 4 km resolution enhanced into MASS NCSU nest run for (a) 0600 UTC 19 July 1991, (b) 0600 UTC 20 July 1991, (c) 0600 UTC 21 July 1991, and (d) 0600 UTC 22 July 1991. Nest grid domain is outlined in white dashed box.

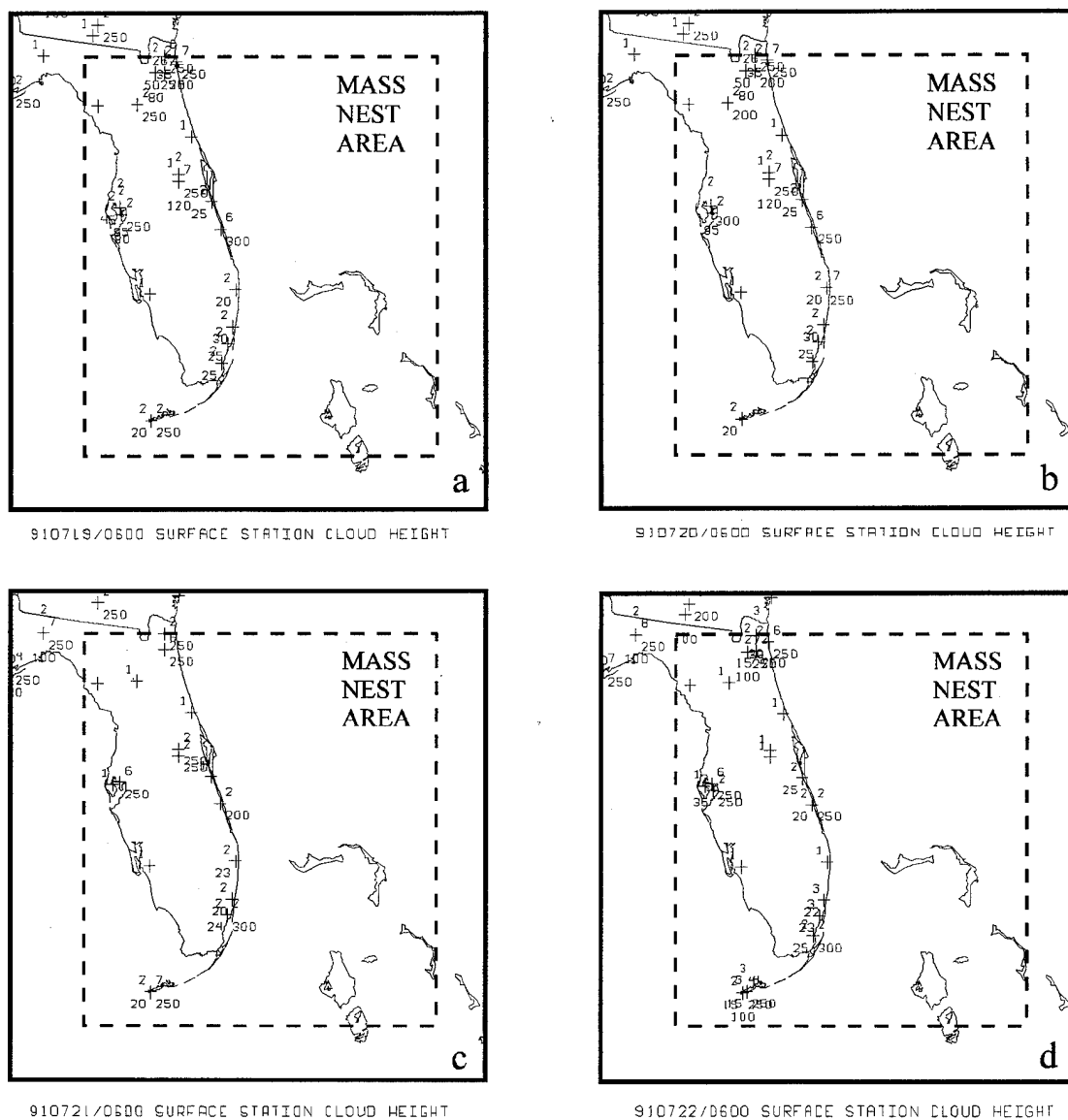


Figure 4.18. Surface cloud observations enhanced into MASS NCSU nest run for (a) 0600 UTC 19 July 1991, (b) 0600 UTC 20 July 1991, (c) 0600 UTC 21 July 1991, and (d) 0600 UTC 22 July 1991. Nest grid domain is shaded light yellow. Cloud observations are plotted as: amount of low cloud in tenths to upper left of station and height of low cloud bases in hundreds of feet to lower left of station, amount of middle cloud in tenths above center of station and height of middle cloud bases in hundreds of feet below center of station, amount of high cloud in tenths to upper right of station and height of high cloud bases in hundreds of feet to lower right of station.

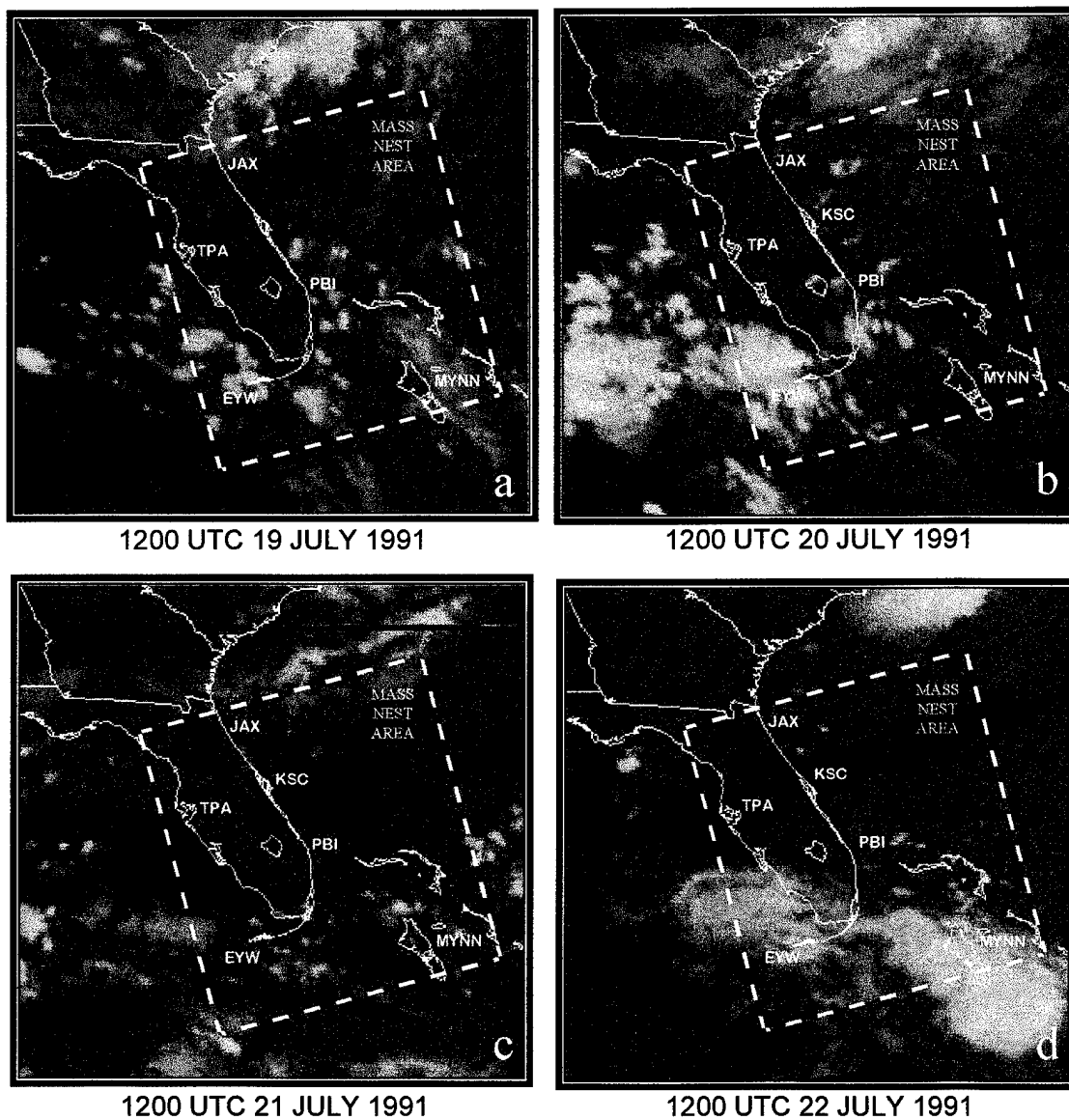


Figure 4.19. GOES-7 infrared satellite imagery with 4 km resolution for (a) 1200 UTC 19 July 1991, (b) 1200 UTC 20 July 1991, (c) 1200 UTC 21 July 1991, and (d) 1200 UTC 22 July 1991. Nest grid domain is outlined in white dashed box.

On the suppressed day at KSC (22 July), the satellite image shows most of Florida to be convection-free except for the southwest corner and over the open waters southwest and south of Florida (Fig. 4.19d). Very strong convection is occurring in the southern Bahama Islands south of Nassau (MYNN). MASS shows general agreement with the satellite observations and there is little moisture at 700 mb over most of Florida (Fig. 4.20d). There are some values of $RH > 70\%$ south of Florida and near the Bahama Islands but no high RH southwest of Florida. The model did well for the KSC vicinity but missed the high moisture over the water. Without any moisture enhancement into the model it might be expected to perform relatively poorly where there is no moisture data with which to initialize the model.

The vertical cross sections from the basic run (Fig. 4.21a, b, c, and d) indicate the relative humidity is greater than 70% every day in the boundary layer, a result which is confirmed by the analysis (see Figs. 2.9a, b, c, and d vertical cross sections). Also, the cross sections clearly show significant deep moisture on both of the active days (Figs. 4.21a and b).

On 19 July (Fig. 4.21a), the cross section shows the moisture layer is quite deep from COF northward to JAX but more shallow south of PBI. The satellite image for this time (Fig. 4.19a) shows active convection from COF south which indicates MASS probably did not simulate a deep enough moist layer representative of this convection.

The cross section on 20 July (Fig. 4.21b), clearly stands out from the rest as having deep moisture throughout the entire cross section. Although the relative

humidity is not depicted as bands of convection as in the cross sections of vertical velocity, it does show this day had the greatest extent of moisture both vertically and horizontally which is in general agreement with the analysis (Fig. 2.9) and the satellite image at the same time (Fig. 4.19b).

The cross sections for the passive and suppressed days (Fig. 4.21c and d) show a significant reduction in moisture throughout the model depth. The relative humidity on 21 July (Fig. 4.21c) is extremely shallow but still maintains a significant horizontal extent along the cross section axis. This follows the perception that this was a transition day with some shallow weak convection in the morning followed by drying and suppression of the convection a few hours later.

Finally, on 22 July (Fig. 4.21d), the model atmosphere has become significantly drier with relative humidities $\geq 70\%$ confined to about 600 mb and below. It is interesting to note the increase in moisture from about PBI south at 450 mb ($\geq 60\%$) as well as the area $\geq 70\%$ at the southern most portion of the cross section. The satellite image (Fig. 4.19d) shows some convection east of PBI and significant convection associated with the 150 mb cold low from offshore southern Florida into the Bahama Islands (through the southern part of the cross section).

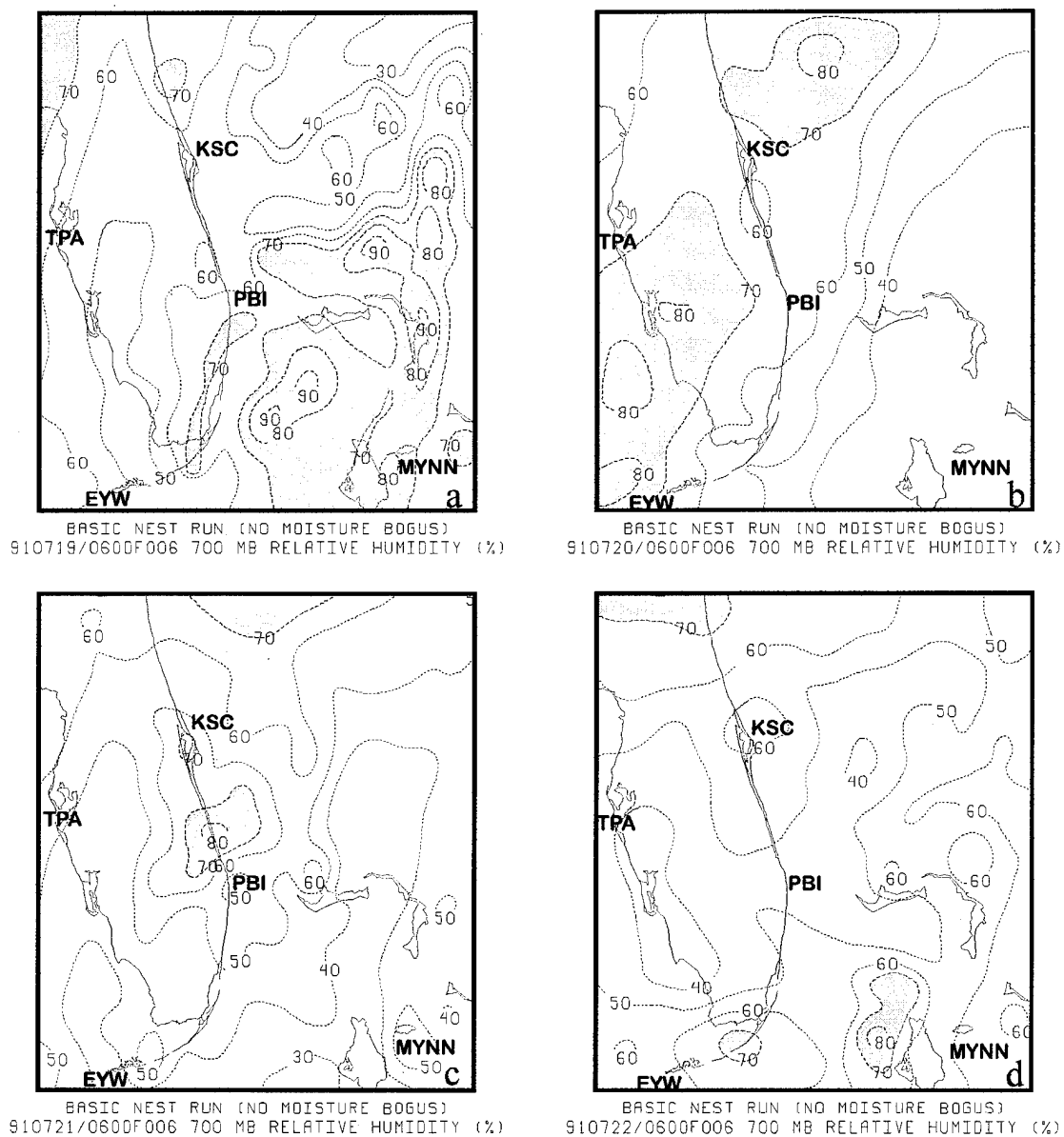


Figure 4.20. MASS 700 mb 6 h forecasts of relative humidity (RH) from the basic (no moisture enhancement) of the NCSU nest grid for (a) 1200 UTC 19 July 1991, (b) 1200 UTC 20 July 1991, (c) 1200 UTC 21 July 1991, and (d) 1200 UTC 22 July 1991. Dashed black contours and green shaded regions denote relative humidity at 10% intervals (shaded above 70%).

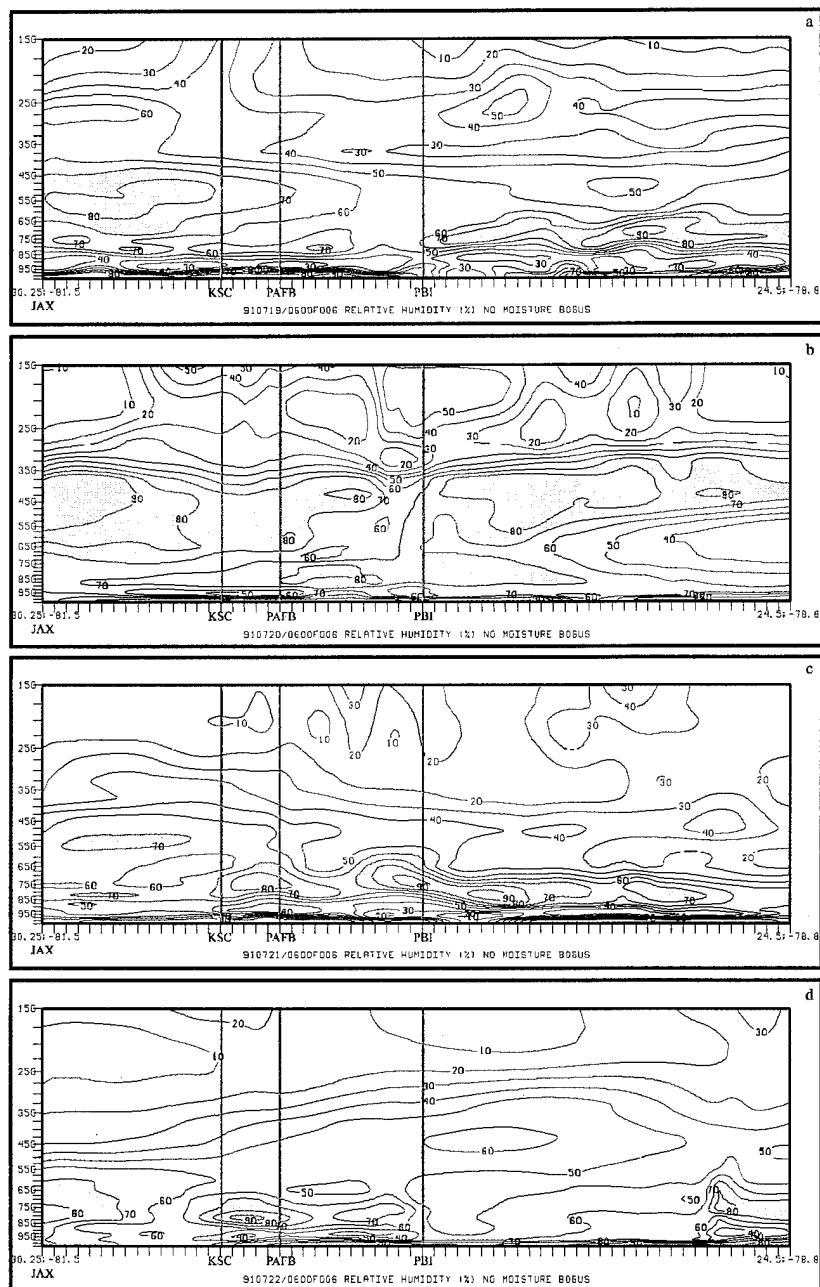


Figure 4.21. MASS nest grid 6 h forecasts of vertical cross sections from the basic (no moisture enhancement) of the NCSU nest grid for (a) 1200 UTC 19 July 1991, (b) 1200 UTC 20 July 1991, (c) 1200 UTC 19 July 1991, and (d) 1200 UTC 20 July 1991. The cross sections were taken from Jacksonville, FL (JAX) through KSC, Patrick Air Force Base (COF), and West Palm Beach, FL (PBI) to just west of the Bahama Islands orthogonal to the 150 mb jet streak and convective rainbands. Solid black contours and green shaded regions denote relative humidity at 10% intervals (shaded above 70%).

4.7.4.2 Manually Digitized Radar (MDR) Moisture Enhancement - MDR Run

The MDR moisture enhancement shows only subtle differences compared to the basic run on 19 July and does a slightly better job depicting convective activity as shown in the 700 mb MASS 6 h forecast of the relative humidity field (Fig. 4.22a). There are two main areas of interest where the MDR moisture enhancement did better. The first area is off the southwest coast of Florida near EYW where convection is observed on the 1200 UTC satellite image (Fig. 4.19a). The second area is along the Florida east coast from just south of KSC to south of PBI which has an expanded area of 60% relative humidity and three areas of relative humidity $> 70\%$. This is in much better agreement with the convection shown on the satellite image (Fig. 4.19a) than without the MDR moisture enhancement.

On 20 July (Fig. 4.22b), the MDR enhancement was not much different than the basic run. The general pattern of moisture distribution at 700 mb was about the same except the MDR data resulted in the higher values of relative humidity covering a slightly larger area north, east, and west of KSC. As in the basic run, the MDR enhancement did not result in a depiction of high relative humidity at 700 mb associated with the convection south of PBI (Fig. 4.19b). This could be because the MDR data assimilated into MASS at 0635 UTC (Fig. 4.16b) only showed two isolated and weak areas of precipitation from just southeast of Florida to the Bahama Islands.

There was little difference between the basic run and MDR assimilated run on 21 July (Fig. 4.22c) except for increased levels of relative humidity from PBI south and

west to EYW which was a result of convection detected by radar in that area at 0635 UTC (Fig. 4.16c).

On 22 July (Fig. 4.22d), the 700 mb relative humidity field is significantly enhanced across the southern part of the nest grid. This is in good agreement with the satellite image from the same time (Fig. 4.19d) where there is a large convective area associated with the 150 mb cold low. The basic run (Fig. 4.20) only showed a couple isolated pockets of high relative humidity associated with this convection. The MDR from 0635 UTC (Fig. 4.16d) clearly showed a large convective complex in the southern region of the nest grid which would account for the increased relative humidity depicted by MASS with the MDR enhancement. There was no change in 700 mb moisture in the KSC vicinity between the basic run and the MDR run.

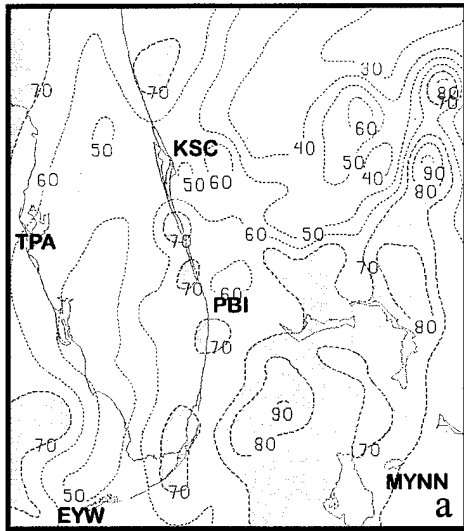
The vertical cross sections from the MDR run (Fig. 4.23a, b, c, and d) are very similar to the basic run with the exception of some greater resolution in the relative humidity distribution including some higher values of relative humidity in some of the higher concentrations of moisture.

On 19 July (Fig 4.23a), there is virtually no difference due to MDR enhancement except for an expanded area of higher relative humidity between COF and PBI between 800 mb and 650 mb which is a result of the convection depicted by the MDR at 0635 UTC (Fig. 4.16a) offshore east Florida. As in the basic run cross section, most of the relative humidity is shallow (below 600 mb) except north of KSC where there was no convection at 1200 UTC.

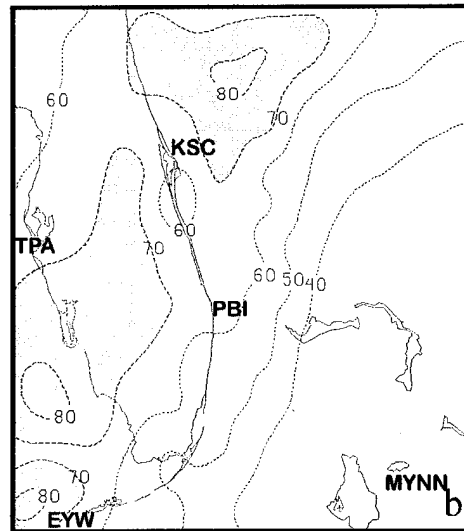
On 20 July (Fig. 4.23b) the MDR run significantly enhanced the relative humidity distribution depicting three distinct cores of relative humidity exceeding 80%. A more banded-like structure can be inferred from this vertical cross section compared to the basic run. This could be due to the banded appearance of the radar data from 0635 UTC (Fig. 4.16a) that was assimilated into MASS. The structure of the rainbands aligned from southwest to northeast is evident in the radar imagery as well as the 1200 UTC satellite imagery (Fig. 4.19b).

The cross section for 21 July (Fig. 4.23c) is also very similar to the basic run cross section as far as placement of the relative humidity regions $\geq 70\%$. The only influence the radar data had on the relative humidity field output by MASS is to depict a slightly deeper extent of the moisture south of PBI associated with the convection detected in that region at 0635 UTC (Fig. 4.16c).

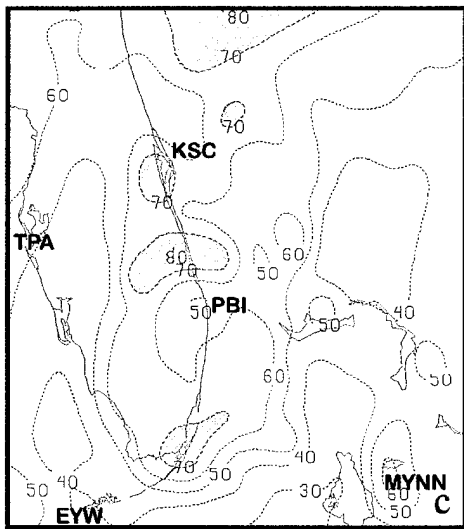
Inclusion of the radar data on 22 July made a significant difference in depicting higher relative humidities in the cross section south of PBI (Fig. 4.23d) associated with the large convective complex seen on the satellite image at 1200 UTC (Fig. 4.19d) and detected by radar at 0635 UTC (Fig. 4.16d). The weaker area of convection shown on the 0635 UTC radar between Florida and the Bahama Islands may be influencing the high relative humidities in the KSC vicinity. As shown previously, the convection was suppressed in the KSC vicinity all day and MASS is generating unrealistically high values of relative humidity here.



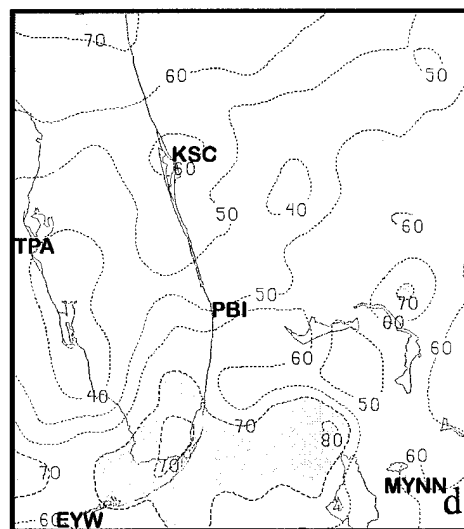
NEST RUN WITH MDR MOISTURE BOGUS
910719/0600F006 700 MB RELATIVE HUMIDITY (%)



NEST RUN WITH MDR MOISTURE BOGUS
910720/0600F006 700 MB RELATIVE HUMIDITY (%)



NEST RUN WITH MDR MOISTURE BOGUS
910721/0600F006 700 MB RELATIVE HUMIDITY (%)



NEST RUN WITH MDR MOISTURE BOGUS
910722/0600F006 700 MB RELATIVE HUMIDITY (%)

Figure 4.22. As in Fig. 4.20 except for the manually digitized radar (MDR) moisture enhancement of the NCSU nest grid.

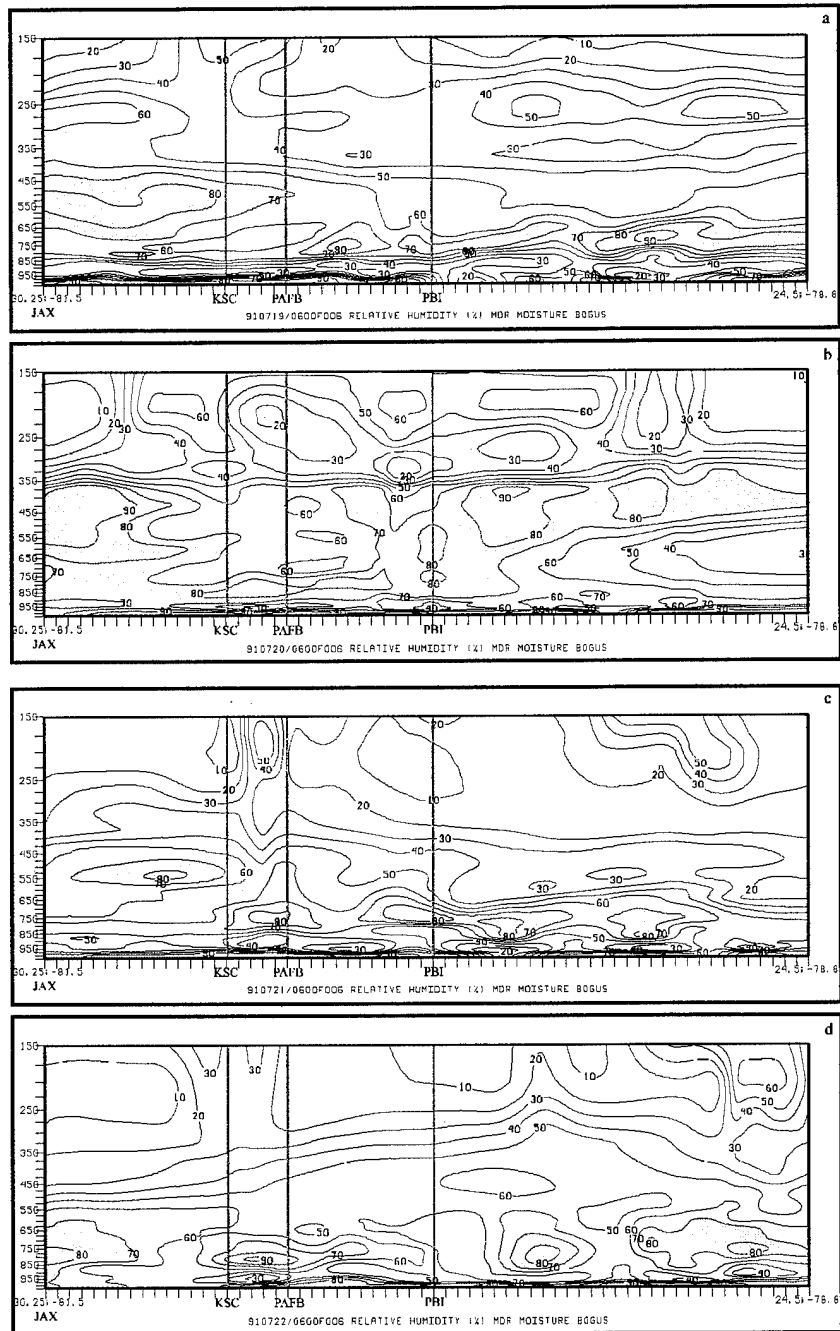


Figure 4.23. As in Fig. 4.21 except for the manually digitized radar (MDR) moisture enhancement of the NCSU nest grid.

4.7.4.3 Infrared Satellite Imagery Moisture Enhancement - Satellite Run

The effect of the satellite imagery enhancement was very significant each day but the model results were mixed. On 19 July, there was a considerable amount of existing convection northeast of KSC and south of PBI into the Bahama Islands (Fig. 4.17a) which was assimilated into the model initialization. This resulted in model relative humidities covering a larger area and with higher values at 700 mb (Fig. 4.24a) compared to the basic and MDR runs. It is also much closer to the depiction of convection in the 1200 UTC satellite imagery (Fig. 4.19a) which shows convection south of PBI into the Bahama Islands. But there is also convection which has developed south of KSC at 1200 UTC which is missed by the model. MASS 700 mb relative humidities in the vicinity of this convection ranges from $< 40\%$ to about 55% . This region of existing convective activity is much drier in the satellite run than either the basic run or the MDR run. This is because the scheme MASS uses to enhance satellite imagery can cause drying in the model atmosphere when no cloud is detected at the initial time (see section 4.6.2).

The scheme that causes the drying of the model atmosphere is very evident in the relative humidity field at 700 mb on 22 July (Fig. 4.24b). Almost the entire nest grid domain has relative humidity values $< 70\%$ except for an isolated area northeast of KSC and west of EYW. This moisture field is totally unrepresentative of the convective activity seen in the satellite image at 1200 UTC (Fig. 4.19b) but it is also obvious why this occurred. The satellite image used to enhance the moisture into the model (Fig.

4.17b) is almost completely void of convective cloud at 0600 UTC which would tend to dry the model atmosphere from its state before the data enhancement. This clearly had a detrimental effect on the model forecast for this most convectively active day by grossly underestimating the water vapor.

The model forecast of 700 mb relative humidity for 21 July (Fig. 4.24c) was about as good as the basic and MDR runs. This was the transition or passive day and the 0600 UTC satellite image (Fig. 4.17c) used in the data enhancement looked about the same as the 1200 UTC satellite image (Fig. 4.19c). Most of the convection at both times was confined to the southern part of the nest grid and although the relative humidity values are generally $< 70\%$ at 700 mb, there are large areas of relative humidity $> 60\%$ indicating the satellite imagery helped moisten a larger area in the model forecast compared to both the basic run and MDR run.

On 22 July (Fig. 4.24d), the satellite enhancement increased the relative humidity in the model simulation over south Florida and into the Bahama Islands compared to the basic run. This is the same region where moisture was enhanced by the MDR run. This region of high relative humidities at 700 mb represents the large convective area in this vicinity associated with the 150 mb cold low and can be seen on the satellite image at 1200 UTC (Fig. 4.19d). This convection was present when the satellite imagery was assimilated into the model initialization at 0600 UTC (Fig. 4.17d). The KSC area relative humidity was unchanged from the basic and MDR runs indicating relatively dry air at this level.

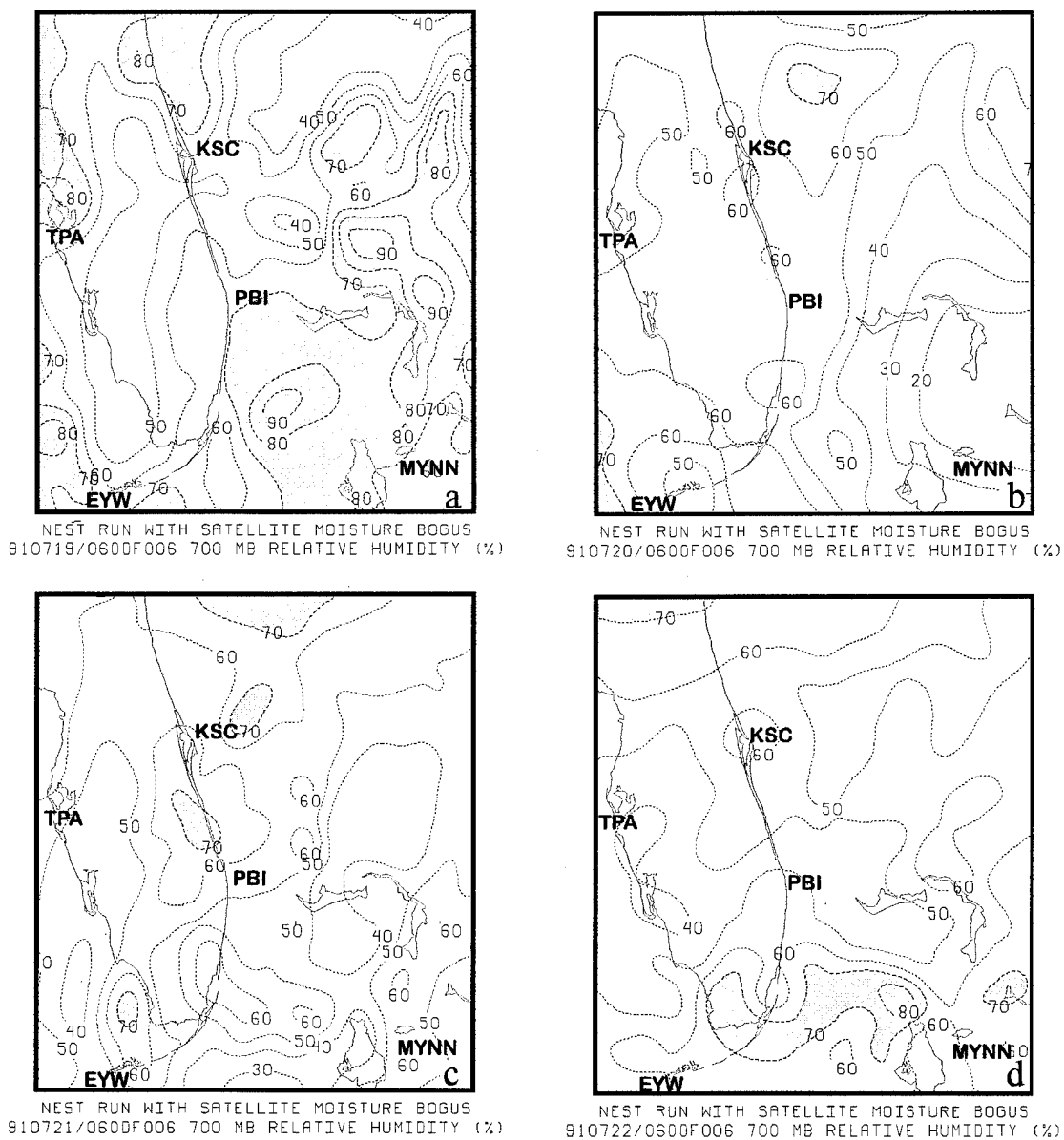


Figure 4.24. As in Fig. 4.20 except for the infrared satellite imagery moisture enhancement of the NCSU nest grid.

The vertical cross sections from the satellite run are shown in Fig. 4.25a, b, c, and d. The 19 July cross section shows more widespread moisture distribution both horizontally and vertically compared to the basic and MDR runs. The relative humidity

exceeds 90% near JAX at about 600 mb which is unlike the other runs and the regions of relative humidity $\geq 70\%$ are deeper. The moisture south of PBI also has larger coverage of higher values ($\geq 80\%$) in the satellite run. This pattern would be expected after examination of the 0600 UTC satellite image (Fig. 4.17a) which indicates middle to high cloud between KSC and JAX as well as some convection south of PBI into the Bahamas. MASS failed to correctly position the moisture since the convection at the model forecast time was mostly occurring south of KSC and also south of PBI at 1200 UTC (Fig. 4.19a).

Because of the lack of clouds at 0600 UTC 20 July (Fig. 4.17b), the satellite data enhanced into MASS acted to dry the model atmosphere which can clearly be seen in the cross section for this day at 1200 UTC (Fig. 4.25b). There is a significant lack of high relative humidities anywhere in the cross section on the most convectively active day. Even though it was previously shown that the most significant upward vertical motion was occurring at this time and the jet streak dynamics supported convection, the satellite data enhancement proved to seriously adversely affect the model solution of water vapor distribution.

On 21 and 22 July the satellite run cross sections (Figs. 25c and d) are nearly the same as in the basic and MDR runs which indicates shallow moisture (below 650 mb) generally from KSC southward on 21 July and shallow but scattered moisture on 22 July.

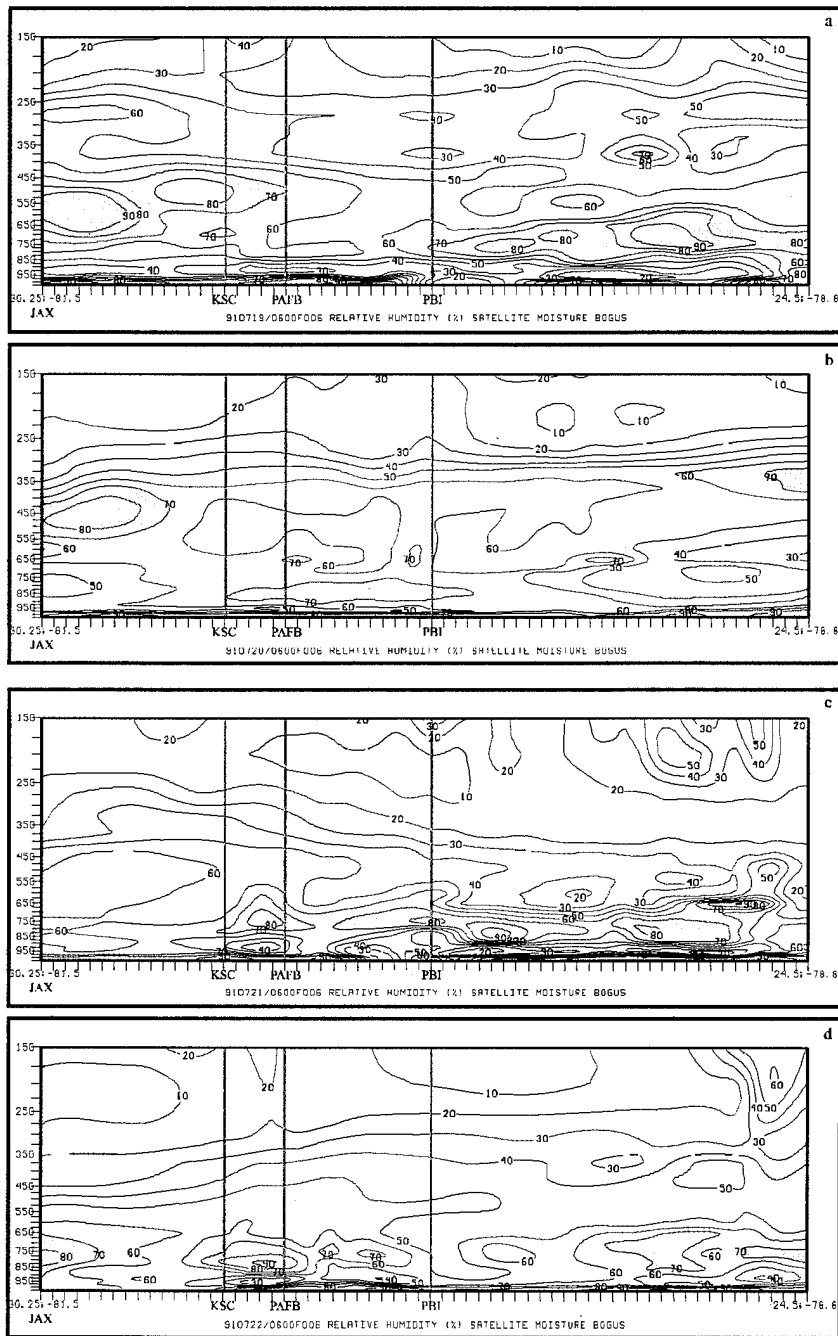


Figure 4.25. As in Fig. 4.21 except for the infrared satellite imagery moisture enhancement of the NCSU nest grid.

4.7.4.4 Surface Cloud Observation Moisture Enhancement - Surface Run

As discussed in section 4.6.3, the data from the surface observations are not directly assimilated into MASS but are incorporated through a fairly complex scheme including a classification system, dataset comparison, and statistical prediction equations to interpolate the surface data to a co-located sounding. Examination of the relative humidity fields in both the 700 mb forecast (Figs. 4.26a, b, c, and d) and the vertical cross section forecast (Figs. 4.27a, b, c, and d) show little difference from the basic run with no moisture enhancement. There are minor differences in relative humidity values (within 10%) but the placement of the relative maximum and minimum values are nearly identical.

4.7.4.5 MDR, Satellite, and Surface Cloud Observation Moisture Enhancement Combined - Combined Run

The last sensitivity test was to enhance all three synthetic moisture sources into the model together to see if the results would be superior to only using one of the sources at a time. Singularly, the MDR run gave the best results and the surface run had the least effect while the satellite run rendered mixed results.

On 19 July (fig. 4.28), the combined run produced the best results compared to the 1200 UTC satellite image (Fig. 4.19a). The highest values of relative humidity correspond very well with the main convective areas in the Bahama Islands and

southeast, south, and southwest of Florida. MASS still simulated very low relative humidity fields at 700 mb where convection was occurring southeast of KSC and high humidity fields at 700 mb where convection was occurring southeast of KSC and high

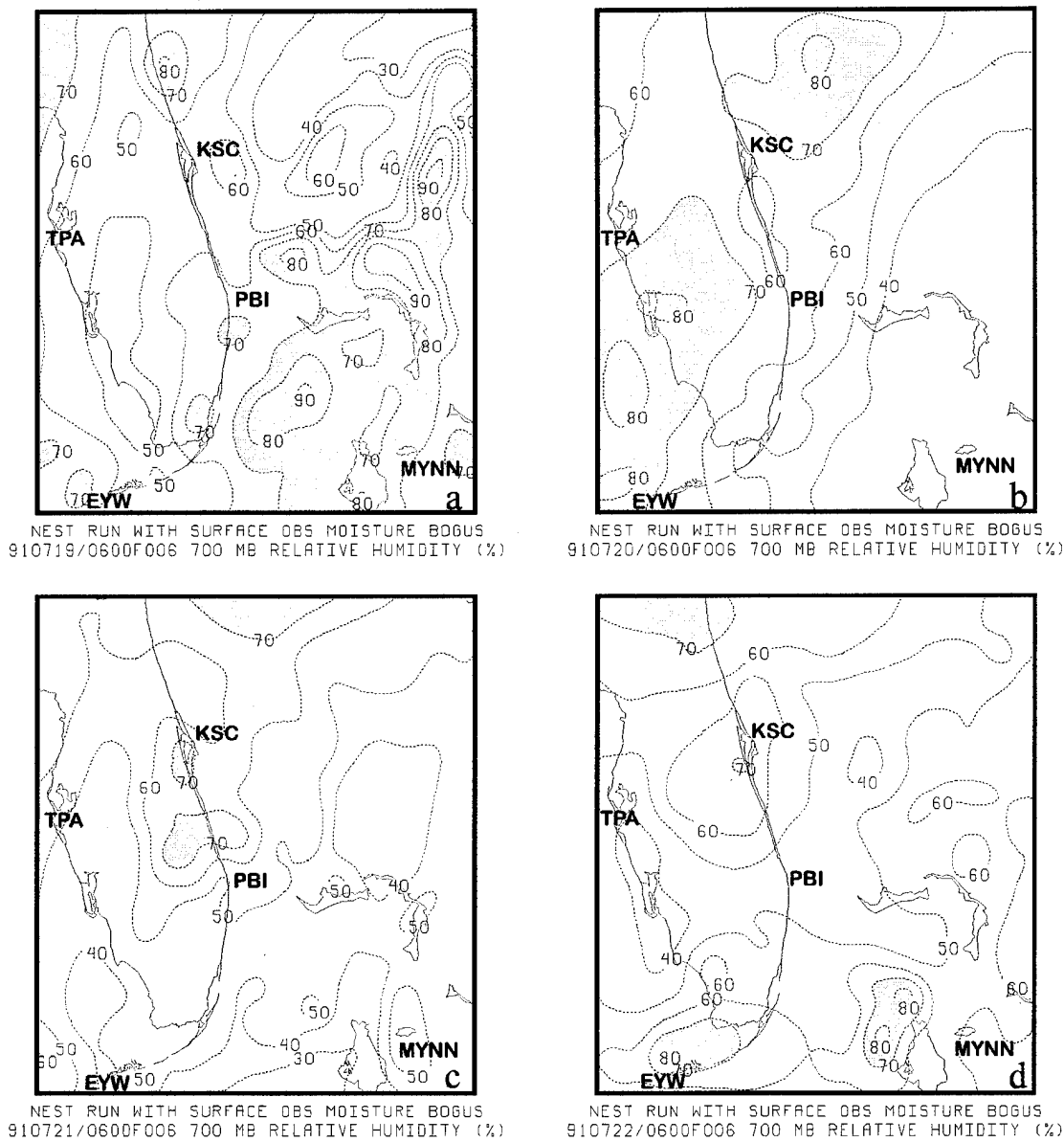


Figure 4.26. As in Fig. 4.20 except for the surface cloud observation moisture enhancement of the NCSU nest grid.

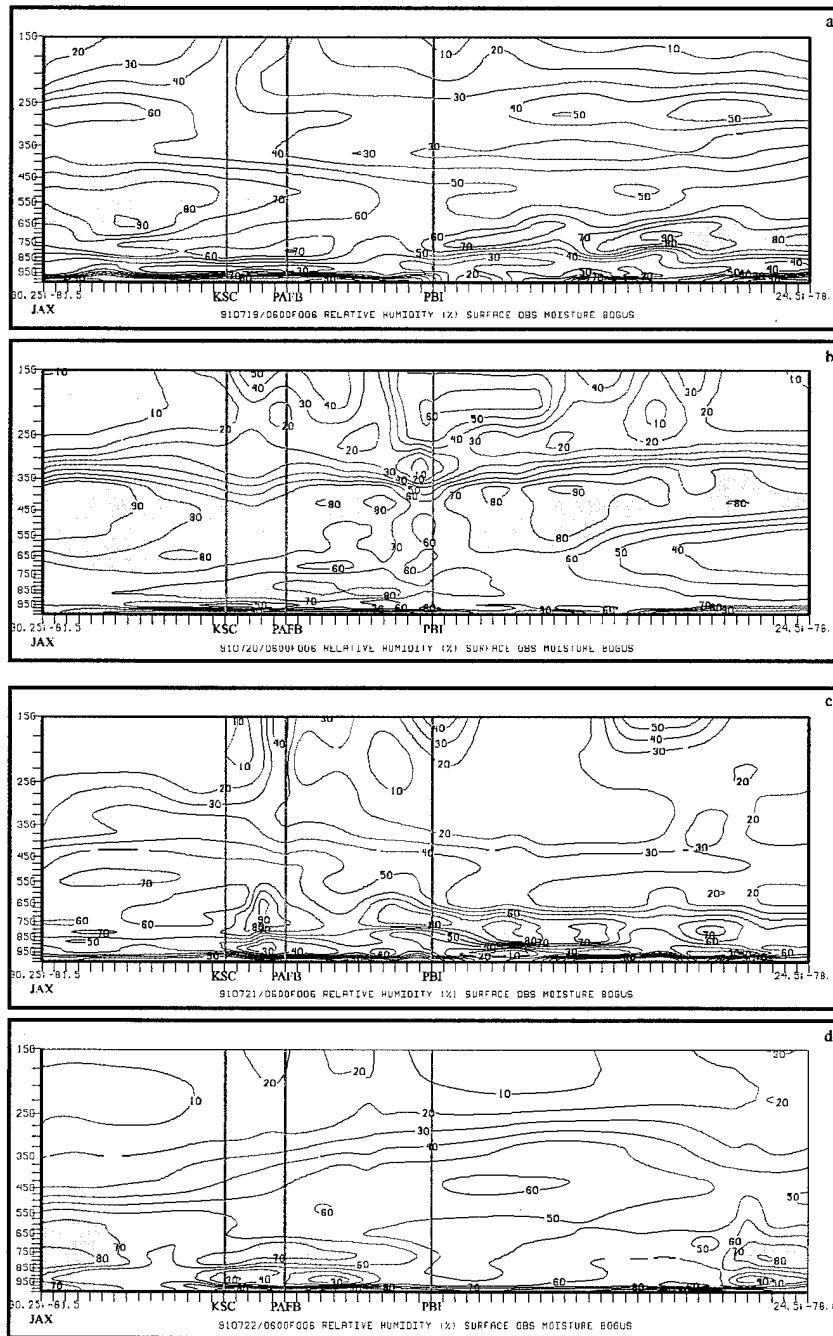


Figure 4.27. As in Fig. 4.21 except for the surface cloud observation moisture enhancement of the NCSU nest grid.

relative humidities north of KSC where convection was not occurring. These two regions of error appear to be most similar to the satellite run and correspond with the moisture distribution seen in the 0600 UTC satellite image (Fig. 4.17a).

On 20 July (Fig. 4.28b), the 700 mb relative humidity was very similar to the convection pattern seen in the satellite image at 1200 UTC (Fig. 4.19b). The relative humidity pattern most closely matches the MDR run but the higher moisture over southeast Florida may have been enhanced by the satellite data.

The 21 July combined run also showed promising results (Fig. 4.28c). The 700 mb relative humidities were considerably lower than any of the single parameter runs which was much more representative of the 1200 UTC satellite image (Fig. 4.19c). MASS depicted a few small regions of relative humidity $\geq 70\%$ south of KSC but some weak convection did occur around 1200 UTC. Each of the other runs depicted either higher relative humidities or larger coverage of similar values of relative humidity. On this day the three different sources complimented each other well.

On 22 July (Fig. 4.28d), similar results were obtained as the moisture distribution was better than any single moisture enhancement run. The KSC vicinity remained relatively dry at 700 mb but the large area of convection in the southern part of the grid domain was very well represented. This is mainly due to the MDR and satellite data combined which, individually, did not cover as large an area with high moisture content at 700 mb.

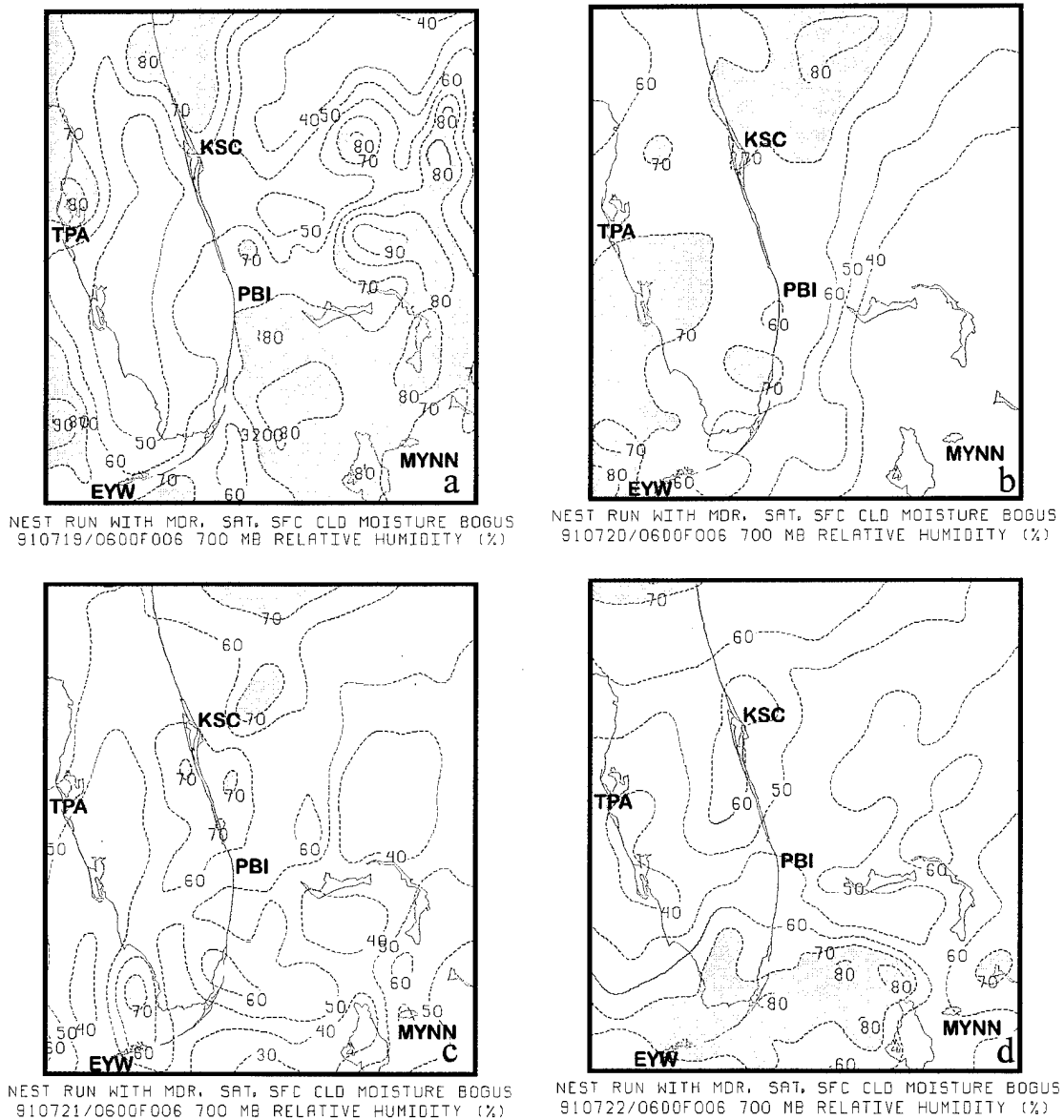


Figure 4.28. As in Fig. 4.20 except for the combined MDR, satellite, and surface cloud observation moisture enhancement of the NCSU nest grid.

Finally, the vertical cross sections for the four days from the combined run (Figs. 4.29a, b, c, and d) did very well representing the vertical (as well as horizontal) moisture distribution.

On 19 July (Fig. 4.29a), the moisture associated with convection south of PBI was deeper and of greater magnitude over a larger area than any of the other runs. This is indicative of the MDR and satellite schemes working together. With infrared satellite data available, the MDR cloud height relationship is not used and the cloud base and top height determination defaults to the satellite imagery data, but the magnitude of the relative humidity is obtained from both sets of data. As in all the runs, there was a large and deep area of high relative humidity from COF to JAX but the only convection at 1200 UTC was just at the northern edge of the grid domain near JAX. However, looking at the water vapor satellite imagery (Fig. 2.10a) indicates relatively high moisture content north of KSC which may account for the mid-level moisture generated by MASS based on rawinsonde data used in the coarse grid run.

The 20 July cross section (Fig. 4.29b) is most interesting as it is the only cross section from this day to clearly indicate the existence of four distinct rainbands. Although the MASS forecast does not place the depicted rainbands in the same location as shown in the satellite image (Fig. 4.19b), there are three individual rainbands located north of KSC, between KSC and PBI and adjacent to PBI with some weak convection near JAX.

The cross sections for 21 and 22 July (Figs. 4.29c and d) also were the most representative model forecasts indicating shallow moisture on 21 July, mostly south of PBI, and mostly dry above 550 mb except for the relatively deep moisture at the southern end of the cross section depicting convection associated with the 150 mb low.

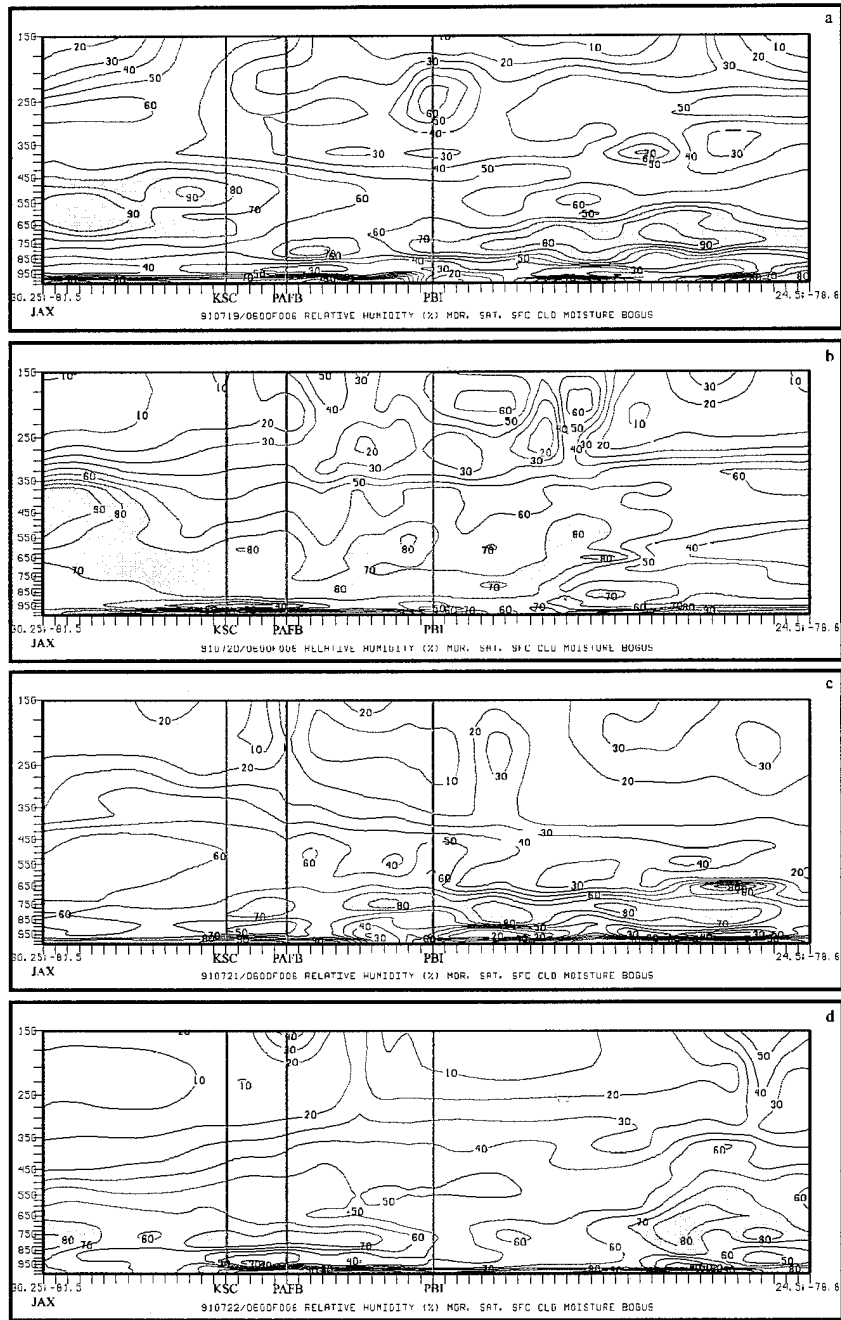


Figure 4.29. As in Fig. 4.21 except for the combined MDR, satellite, and surface cloud observation moisture enhancement of the NCSU nest grid.

4.8 Model Precipitation Results

The precipitation fields generated in MASS come from the grid scale moisture physics module using the prognostic moisture scheme. By using the prognostic moisture scheme, conservation equations for cloud water and cloud ice (q_c) and rain water and snow (q_r) added to the MASS basic set of prognostic equations. These equations are:

$$\frac{\partial q_c}{\partial t} = m \left(\underbrace{-u \frac{\partial q_c}{\partial x} - v \frac{\partial q_c}{\partial y}}_{\text{Horizontal Advection}} \right) - \underbrace{\dot{\sigma}_p \frac{\partial q_c}{\partial \sigma_p}}_{\text{Vertical Advection}} + \underbrace{P_{gci} - P_{ced} - P_{aut} - P_{acr}}_{\text{Cloud Microphysics Effects}} + \underbrace{(Q_c)_{diff}}_{\text{Lateral Diffusion}} \quad (4.5)$$

$$\frac{\partial q_r}{\partial t} = m \left(\underbrace{-u \frac{\partial q_r}{\partial x} - v \frac{\partial q_r}{\partial y}}_{\text{Horizontal Advection}} \right) - \underbrace{\dot{\sigma}_p \frac{\partial q_r}{\partial \sigma_p}}_{\text{Vertical Advection}} - \underbrace{g \frac{\partial (\rho q_r v_t)}{\partial p}}_{\text{Fallout Term (Precipitation)}} + \underbrace{P_{aut} + P_{acr} - P_{red}}_{\text{Cloud Microphysics Effects}} + \underbrace{(Q_r)_{diff}}_{\text{Lateral Diffusion}} \quad (4.6)$$

Equation (4.6) simulates the amount of precipitation from the fourth term (fallout term). The mass-weighted mean of the terminal velocity (v_t) must be parameterized and is based on whether or not the temperature of a layer is above or below 0°C. The fallout term is integrated from the top of the model atmosphere downward and any condensate reaching the bottom of the model's lowest layer (the surface) is accumulated as precipitation (MESO, Inc. 1995).

Since it was shown in previous sections that the enhancement of moisture by combining the MDR, satellite, and surface observations produced the best moisture distribution results, only precipitation results from the combined run are shown.

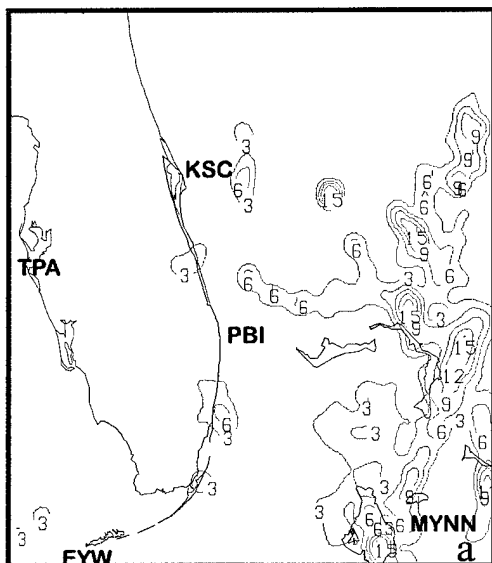
The cumulative convective precipitation is shown in Figs. 4.31a, b, c, and d. The precipitation was totaled over six hours \pm 3 h of 1200 UTC on each of the four days. Most of the simulated precipitation is located over the Bahama Islands on 19 July (Fig. 4.31a) with an area extending westward towards Florida north of PBI. This is in good agreement with the 1200 UTC satellite image (Fig. 4.19a) which shows convection widespread over the Bahama Islands with an area of convective showers extending northwestward to north of PBI as well as some isolated convection near the southeast Florida coastline. Offshore KSC and between KSC and PBI MASS simulated three small areas of convective precipitation which is representative of the shower activity shown on the reflectivity display from the CP-4 radar (Fig. 4.32a). As previously shown, the convection was not quite as organized as on the most active day, yet convection did develop offshore KSC as small convective cells which is what the MASS simulated precipitation emulates offshore KSC.

On 20 July the MASS simulated precipitation clearly shows an organized pattern in the form of two rainbands east and northeast of KSC (Fig. 4.31b). This is an excellent simulation based on the convective cloud structure seen in the satellite image (Fig. 4.19b) as well as the CP-4 radar reflectivity (Fig. 4.32b). Although not well developed at this time, there is one obvious rainband indicated on radar with a second one

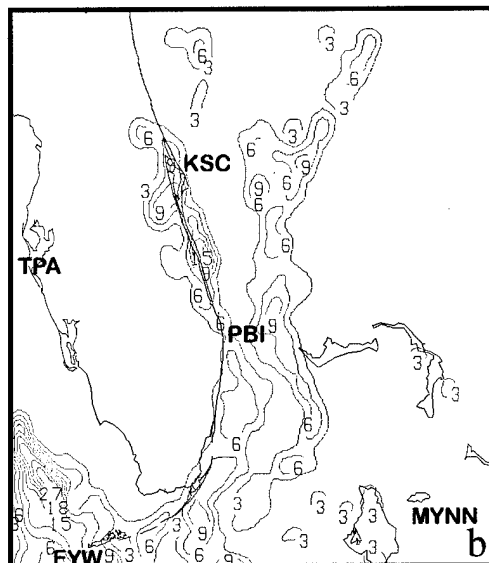
developing as shown in the figure. MASS also correctly simulated the convection along the southeast Florida coast plus the large convective region northwest of EYW. MASS simulated 27 mm of precipitation over 6 hours in the core of the convective complex northwest of EYW where MDR indicated a maximum of VIP 5 with 49,000 ft echo tops between 0935 UTC and 1335 UTC.

On the transition or passive day, MASS simulated considerably less precipitation than either of the two active days. Fig. 4.31c shows the MASS simulated convective precipitation scattered through the Florida Keys, Bahama Islands, and along and just offshore the east-central Florida coastline. The satellite image (Fig. 4.19c) confirms the convection in the southern part of the nest grid domain but does not show convection where MASS simulated precipitation from KSC south to near PBI nor offshore east-central Florida. The CP-4 radar reflectivity does show some very small showers near and just north of KSC plus offshore. These showers are so small the 4 km infrared satellite image could not detect them. But MASS did simulate an area much larger in coverage over east-central Florida and on the order of the larger convection occurring elsewhere at the same time, concluding MASS produced too much precipitation in the KSC vicinity.

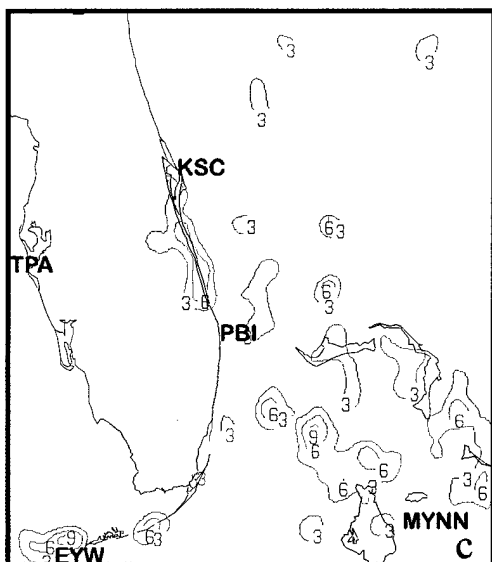
On 22 July (Fig. 4.31d), MASS simulated a few small pockets of precipitation in the KSC vicinity yet there was no precipitation on this suppressed day, confirmed by CP-4 radar (Fig. 4.32d). MASS did correctly simulate the precipitation occurring between southeast Florida and the Bahama Islands associated with the 150 mb cold low.



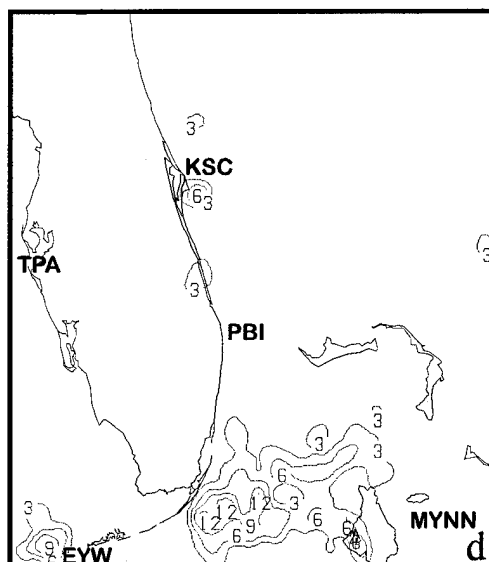
910719/0600F003 : 910719/0600F009 NEST
MDR, SAT & SFC MOISTURE BOGUS
6 HOUR CONV PRECIP (MM)



910720/0600F003 : 910720/0600F009 NEST
MDR, SAT & SFC MOISTURE BOGUS
6 HOUR CONV PRECIP (MM)



910721/0600F003 : 910721/0600F009 NEST
MDR, SAT & SFC MOISTURE BOGUS
6 HOUR CONV PRECIP (MM)



910722/0600F003 : 910722/0600F009 NEST
MDR, SAT & SFC MOISTURE BOGUS
6 HOUR CONV PRECIP (MM)

Figure 4.31. MASS 3-6 h forecasts of cumulative convective precipitation from the combined moisture enhancement (MDR, satellite, and surface observation data) of the NCSU nest grid for (a) 09-15 UTC 19 July 1991, (b) 09-15 UTC 20 July 1991, (c) 09-15 UTC 21 July 1991, and (d) 09-15 UTC 22 July 1991. Contours of simulated precipitation accumulation are drawn and labeled every 3 mm.

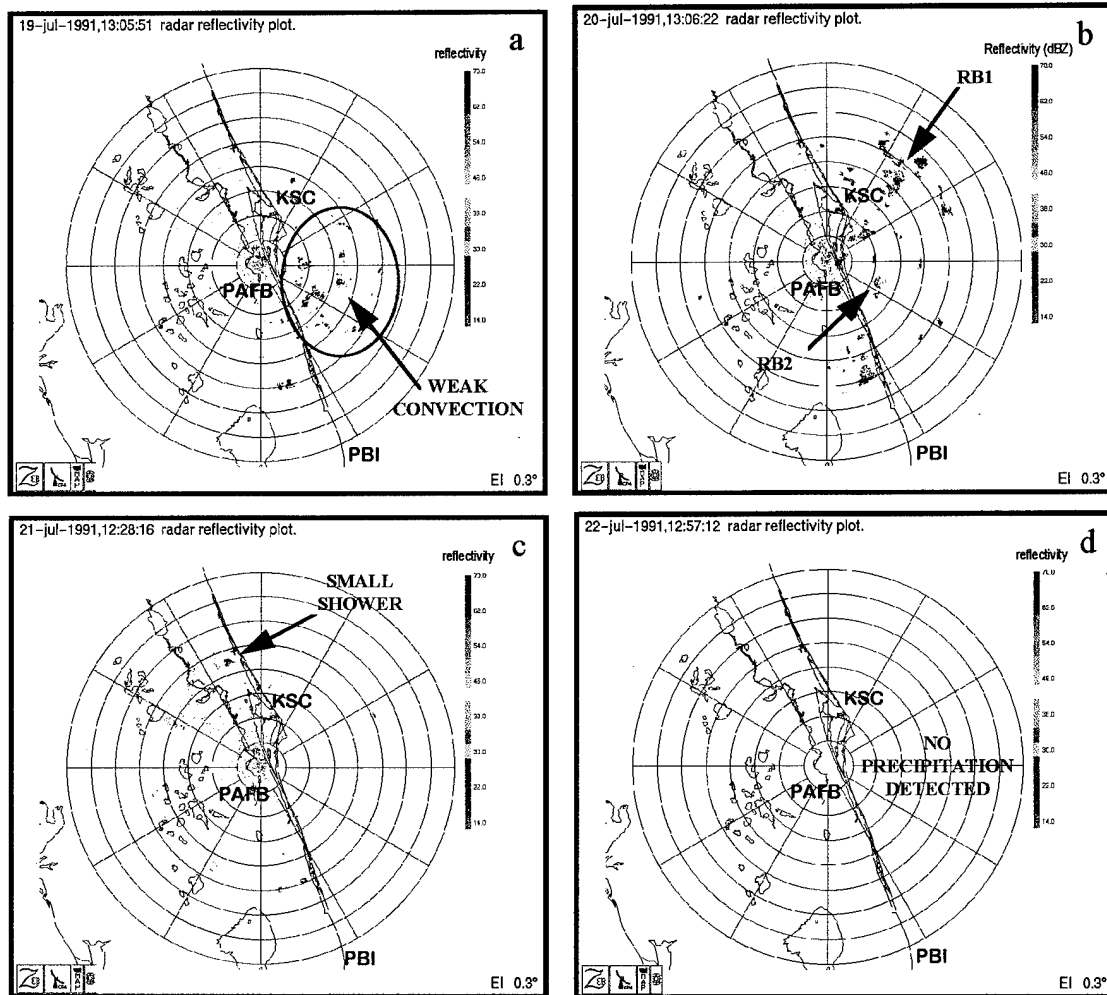


Figure 4.32. Plan Position Indicator (PPI) view of the 0.3° elevation angle scan of reflectivity from the CP-4 Doppler radar for (a) 1305 UTC 19 July 1991, (b) 1306 UTC 20 July 1991, (c) 1228 UTC 21 July 1991, and (d) 1257 UTC 22 July 1991. Reflectivity scale (dBZ) is shown.

5. VISUALIZATION

Traditional meteorological data analysis has been two-dimensional, black and white hardcopy. Only within the past few years have meteorologists moved from the traditional analyses to full color graphics on computer systems. However, for the most part, the data is still viewed in two dimensions. Significant skill is required to take the two-dimensional horizontal or vertical cross sections of isolines and put the information together to develop a "mental picture" of the atmosphere.

Use of visualization in meteorology is generally limited to research applications because the hardware and software required for visualization has been, until recently, cost prohibitive for most users. As the cost of high power computer graphics workstations drops and more user-friendly software is developed, this powerful tool will be more accessible to operational users.

The Application Visualization System (AVS) (Advanced Visual Systems, Inc. 1992) was used for three-dimensional (3-D) graphics visualization in this research. AVS is a state-of-the-science tool that has been used to help meteorologists examine numerical model output including both analysis and verification (Schmidt and Snook 1992), quality control three dimensional data fields (Hartsough 1992), and visualize complex circulations in the Earth's atmosphere in four dimensions (Wylie 1993).

Since the key features presented in this research have been development of the subtropical upper tropospheric jet streak and water vapor distribution, the visualization will focus on these fields as well. MASS model output from both the coarse and nested

simulations will be shown using the same grids as the other MASS output shown in Section 4.

The GEMPAK grids produced from MASS are ingested into AVS via a software package called GEMPAK Visualization System (GEMVIS) (Hagedorn 1993). GEMVIS was designed for interactive analysis and three-dimensional visualization of atmospheric data.

Once the grids have been ingested into AVS, the user has the capability to view the data from any perspective by rotating the image on the screen via a mouse and keyboard controls. Two examples of different perspectives are from the MASS coarse grid for 20 and 22 July 1991. The first view is from the south side of the grid domain looking north (Figs. 5.1a and b). The upper tropospheric jet streak is depicted as a 15 ms^{-1} isosurface. Everywhere the gray shaded surface is observed indicates winds $\geq 15 \text{ ms}^{-1}$. This view clearly shows the depth and orientation of the developing jet streak between the active (20 July) and suppressed (22 July) days. It also shows that the left exit region of the jet streak is above the KSC vicinity on 20 July (Fig. 5.1a) and the left entrance region of the jet streak is above the KSC vicinity on 22 July (Fig. 5.1b). This view is far superior to a two-dimensional vertical cross section because it gives the meteorologist the opportunity to see the vertical extent and orientation of the jet streak from any perspective without having to choose a cross section which may or may not capture the feature of most interest.

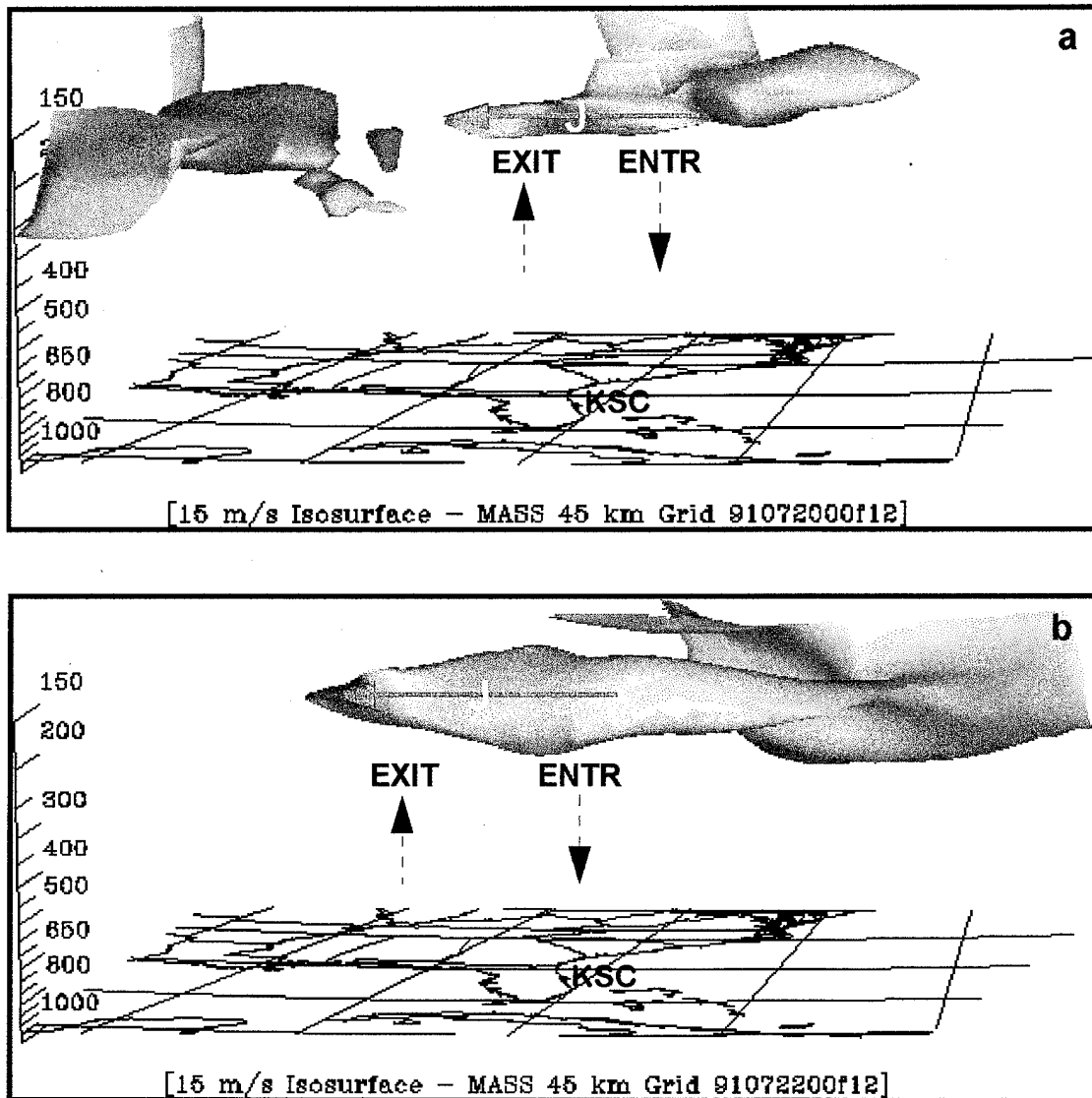


Figure 5.1 MASS coarse grid 12 h forecast visualized with the Application Visualization System (AVS) for (a) 1200 UTC 20 July 1991 and (b) 1200 UTC 22 July 1991. The gray shaded areas represent the 15 ms^{-1} isosurface. The cyan arrow represents the jet streak. The jet streak maxima is shown by the “J” and “EXIT” depicts the jet streak left (south) exit region while “ENTR” depicts the jet streak left (south) entrance region. The vertical scale (mb) is shown on the left. The red dashed arrow indicates upward vertical motion and the blue dashed arrow represents downward vertical motion based on the jet streak model presented in this research.

A perspective from above the grid domain better shows the horizontal extent of the jet streak (Figs. 5a and b). This view also helps the meteorologist better see what region of the map lies under jet streak to better discern how the transverse circulations and vertical motions are situated relative to the location of interest. As in the previous figure, it is evident that the KSC vicinity is under the influence of the left exit region of the jet on 20 July and the left entrance region on 22 July. This agrees with the conventional analyses presented in the previous sections but it is easier and faster to view the 3-D fields as presented here.

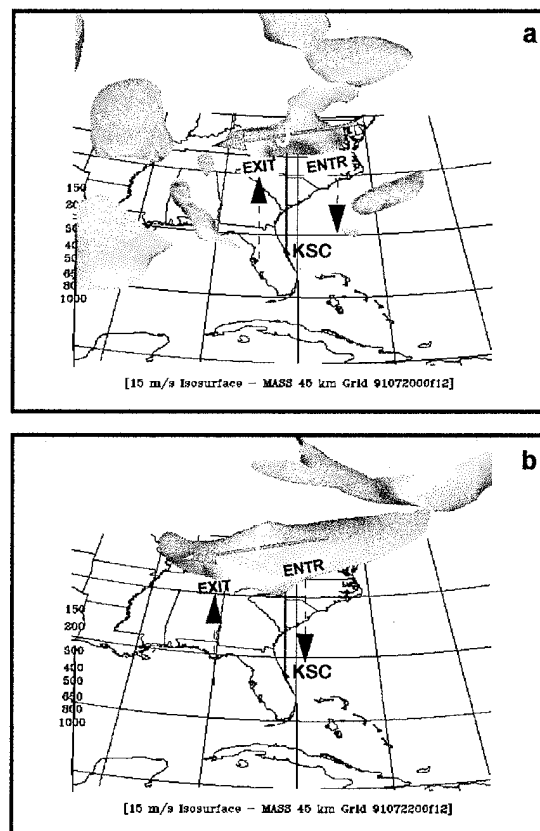


Figure 5.2 As in Fig. 5.1 except the view is now from a higher angle looking down on the grid domain. The dark red line is drawn vertically to help show position of KSC relative to the jet streak.

The nested grid is first shown as a side view from the south side of the domain looking north (Figs. 5.3a and b). The 6 h MASS nested grid forecast of the 75% relative humidity isosurface shows how significantly deeper and more widespread the moisture was distributed on the active day (Fig. 5.3a) versus the suppressed day (Fig. 5.3b). From this perspective it shows the deepest moisture east of KSC over the Atlantic Ocean

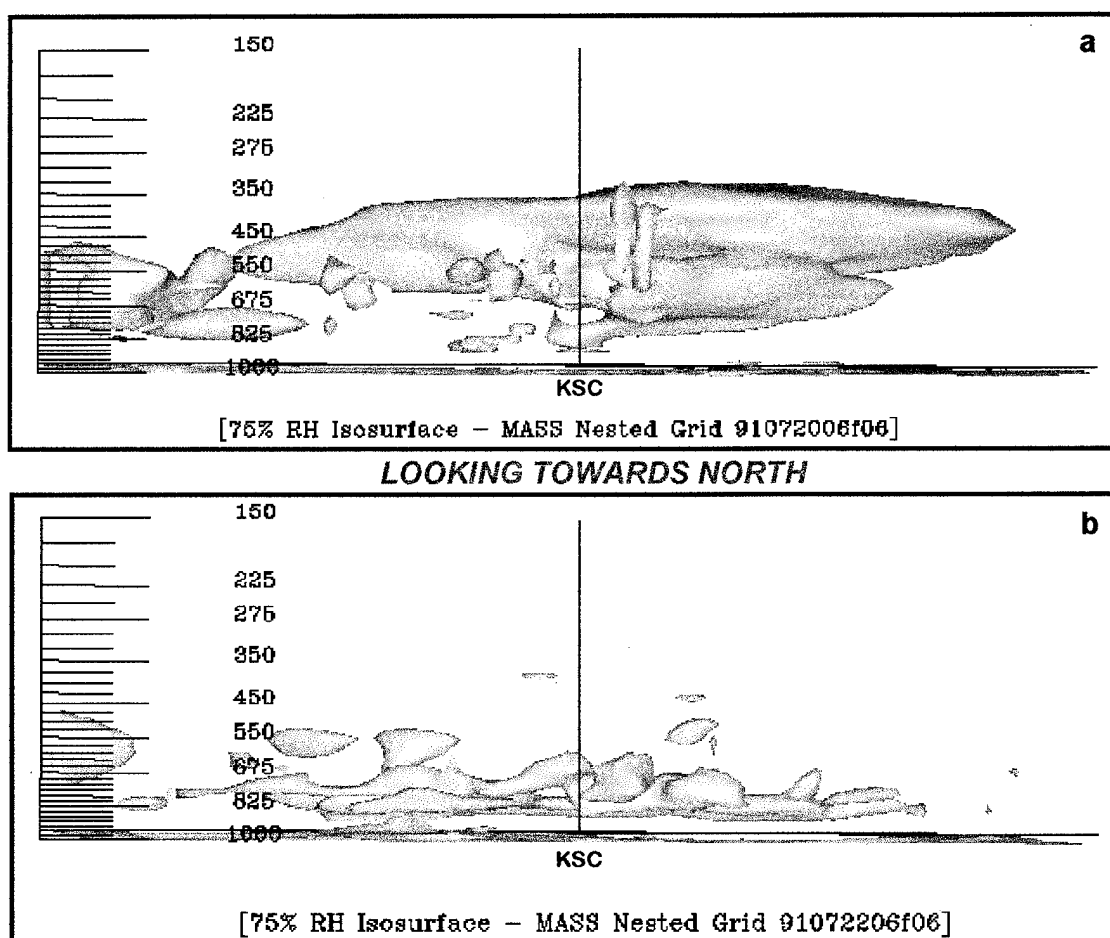


Figure 5.3 MASS nested grid 6 h forecast visualized with the Application Visualization System (AVS) for (a) 1200 UTC 20 July 1991 and (b) 1200 UTC 22 July 1991. The gray shaded areas represent the 75% relative humidity isosurface. The dark red line is drawn vertical to help show position of KSC on the grid. The vertical scale (mb) is shown on the left.

on 20 July with mid-level moisture (about 800-350 mb) west of KSC. On 22 July, the moisture appears to be more evenly distributed throughout the lower troposphere.

A top-down perspective will help determine the horizontal extent of the moisture distribution. It is obvious that the greatest expanse of moisture on 20 July (Fig. 5.4a) extends from the southwest corner of the grid domain through central Florida and offshore KSC. However, a very large area of moisture in the lowest part of the troposphere can also be seen in the eastern most part of the grid domain from the Bahama Islands northward. This view also shows the breadth and depth of the moisture is most significant from KSC eastward implying this region is most likely to experience convection, as it did. On 22 July, (fig. 5.4b) shows most of the moisture is confined to the southern part of the grid domain. As previously noted, this area experienced a significant amount of convective precipitation due to the proximity of the upper tropospheric cold low.

Any gridded meteorological field can be displayed with AVS. These few examples demonstrate the effectiveness of 3-D visualization to allow quick interpretation of meteorological fields. Forecasters would significantly benefit from the availability of real-time 3-D visualization capabilities to use as an analysis tool. This, in turn, could help provide a better nowcast in support of Space Shuttle launch and landing operations.

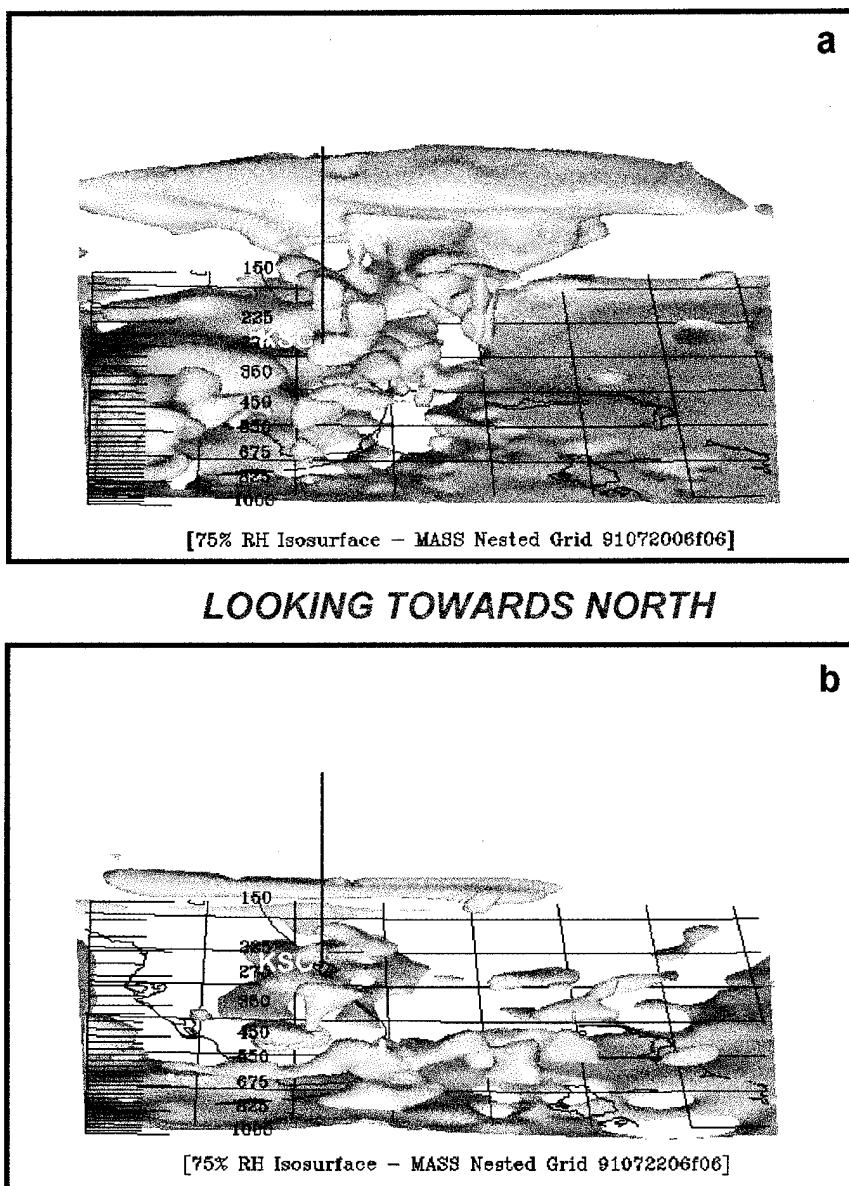


Figure 5. 4 As in Fig. 5.3 except the view is now from a higher angle looking down on the grid domain.

6. SUMMARY AND CONCLUSIONS

To ensure safe landings of the Space Shuttle, flight rules demand very accurate nowcasts (0-2 h forecasts) of clouds, precipitation, lightning, turbulence, and winds at the Shuttle Landing Facility at KSC for Space Shuttle launches and for landings at mission end. Rapid small scale development and dissipation of convection caused by the mesoscale impact of Cape Canaveral's geography result in a forecast challenge.

The general pattern of convection over the Florida Peninsula is directly related to the synoptic wind field and the interaction of sea breeze fronts. Experience has shown that short term forecasting of convective activity in the vicinity of KSC during onshore flow is a particularly challenging problem since it is frequently not associated with sea breeze and land breeze activity. Seemingly similar synoptic regimes are present in cases that produce conditions ranging from clear skies to heavy showers.

Through analysis of four days of onshore flow data taken during the CaPE experiment, this research has shown that the onset of convective activity can be particularly difficult to predict without looking at some very specific parameters. The data presented has shown that, in general, similar synoptic environments are present in the KSC vicinity on all four days that produce two active, one passive, and one suppressed convective day at KSC. To discern the critical features that show there are some significant dissimilarities between each of the four days a careful regional analysis was required.

Low-level convection is initiated at the apex of Rayleigh-Bernard cells and most likely organized into longitudinal rainbands by mixed mode wave-CISK. The orientation of the rainbands is determined by the shear in the rainband layer and buoyancy is the primary energy source to maintain the rainbands.

The dynamics of a developing subtropical jet streak at 150 mb were precipitated by an increased pressure gradient in the upper troposphere due to the northwestward movement of an upper-level cold core low into Florida from the Bahamas Islands which was associated with the tropical upper tropospheric trough. This led to a shift from an upper-level divergent pattern to an upper-level convergent pattern. Based on these dynamics, the total column mass adjustment over central Florida supported upper-level divergence with coupled low-level convergence on the convectively active days of 19 and 20 July. On 21 and 22 July convection was suppressed and the regime was opposite of the two active days. Rawinsonde observations supported the regional analysis and showed that early in the period the flow at low levels was more predominantly southeasterly while later in the period it was more easterly or east-northeasterly. This reflected a more confluent lower branch of the deep circulation early in the period gradually transforming into a more diffluent lower branch of the deep circulation later in the period. It is the transverse circulations associated with the upper tropospheric jet streak that distinguishes between the active and passive days.

The use of water vapor imagery supported the observed wind maxima aloft and resulting upper level convergence and downward vertical motion. Although water vapor

imagery should not be used as a stand-alone tool, it can be used in conjunction with the other analysis methods identified and discussed to help predict location and timing of convection during easterly flow regimes.

The need for improved measurement of water vapor downstream from KSC was discussed. It was shown that the Global Positioning System can provide accurate all-weather measurements of atmospheric water vapor with higher temporal and horizontal resolution. It may be possible to improve KSC nowcasts by placing GPS receivers at fixed locations downstream of KSC to measure water vapor.

The MASS model was used to simulate the large scale dynamics by running the model with a 45 km (coarse) grid. MASS correctly simulated the movement of the upper tropospheric cold low which was responsible for development of the 150 mb jet streak. The jet streak-associated transverse ageostrophic circulations were well simulated by the model.

Nested MASS model simulations successfully simulated the patterns of convective precipitation and distinguished active and passive days. Enhancing the initialization of the nested simulations with synthetic relative humidity sources showed that:

- (i) manually digitized radar data increased the moisture in the model atmosphere every day.

(ii) infrared satellite imagery increased the moisture in the model atmosphere only when cloud was present but (incorrectly) decreased the moisture when cloud was not present.

(iii) surface cloud observations showed little change in the moisture distribution.

(iv) all synthetic relative humidity sources combined provided the best moisture initialization.

Three-dimensional visualization techniques allow quick interpretation of any meteorological field. The fields can be easily rotated and viewed from any angle on a computer screen with a mouse and keyboard controls. This can eliminate the necessity for numerous horizontal and vertical cross sections which may or may not correctly show the meteorologist the correct area of interest. By using 3-D visualization, the meteorologist can see an entire domain at once and focus attention immediately on the region of primary concern to the forecast.

7. RECOMMENDATIONS AND FUTURE RESEARCH

It is recommended that a climatological study of onshore flow days at KSC be undertaken. Using this research as a guide, the climatological study should verify the role of the subtropical jet during weak summertime regimes and the resulting trends in water vapor distribution on active and suppressed convection. A climatology of onshore flow will test the hypothesis that subtropical wind maxima must be scrutinized and related to the water vapor distribution when assessing convective instability triggers and static stability indices.

Installation of GPS receivers downstream of KSC will improve data analysis as well as a mesoscale model. The convective rainbands that formed during the easterly flow event investigated were on a scale much smaller than normally resolved by current hydrostatic mesoscale models. Mesoscale data are currently limited in horizontal resolution to the spacing of the rawinsonde network which is used to initialize mesoscale models like MASS. Kuo et al. (1993) indicated that assimilating precipitable water vapor observations into mesoscale models significantly improves precipitation forecasts (Businger et al., 1995).

To make continued progress in short-term forecasting for Shuttle activity, ongoing research in the application of new data sources (GOES-8, WSR-88D Doppler radar) in operational forecasting is recommended. Integrated moisture data and refractivity profiles from ground and space-based Global Positioning System (GPS)

receivers represent promising new data resources (Businger et al. 1995). Assimilation of GOES-8, Doppler radar and GPS data into mesoscale numerical models of increasing resolution (e.g., Zack et al. 1988) may result in tangible improvement in our ability to nowcast convective activity in the vicinity of KSC.

Further development of visualization techniques should be undertaken to help meteorologists view atmospheric data in 3-D. Interpretation of 3-D data can allow the meteorologist to more quickly determine areas and parameters to focus on. Software needs to be developed to provide meteorologists with a more "user friendly" interface to access 3-D visualization.

8. LIST OF REFERENCES

- Adler, R. F. and A. J. Negri, 1988: A satellite infrared technique to estimate tropical convective and stratiform rainfall. *J. Appl. Meteor.*, **27**, 30-51.
- Advanced Visual Systems, Inc., 1993: AVS User's Guide. Advanced Visual Systems, Inc. Waltham, MA. 375 pp.
- Anderson, R., J. Gurka, and S. Steinmetz, 1982: Applications of VAS multispectral imagery to aviation forecasting. *Preprints to the 9th Conference on Weather Forecasting and Analysis*, Seattle, Washington, American Meteorological Society, Boston.
- Arritt, R. W., 1993: Effects of the large-scale flow on characteristic features of the sea breeze. *J. Appl. Meteor.*, **32**, 116-125.
- Barnes, S. L., 1964: A technique for maximizing details in numerical weather map analysis. *J. Appl. Meteor.*, **3**, 396-409.
- Barnes, S. L., 1973: Mesoscale objective analysis using weighted time-series observations. NOAA Tech. Memo. ERL NSSL-62, Norman, OK, 60 pp.
- Bauman, W. H., J. T. Madura, and B. F. Boyd, 1992: Near real-time high resolution upper air balloon measurements for space launch support, Paper 92-0721, *American Institute of Aeronautics and Astronautics 30th Aerospace Sciences Meeting*, 11-14 January 1992, Reno, NV.
- _____ and S. Businger, 1995: Nowcasting for Space Shuttle landings at Kennedy Space Center, Florida. *Bull. Amer. Meteor. Soc.*, In review.
- Bennetts, D. A. and B. J. Hoskins, 1979: Conditional symmetric instability - a possible explanation for frontal rainbands. *Quart. J. Roy. Meteor. Soc.*, **105**, 945-962.
- Blanchard, D. O. and R. E. López, 1985: Spatial patterns of convection in south Florida. *Mon. Wea. Rev.*, **113**, 1282-1299.
- Boybeyi, Z. and S. Raman, 1992: A three-dimensional numerical sensitivity study of convection over the Florida peninsula. *Boundary-Layer Meteorol.*, **60**, 325-359.

- Brody, F. C., 1993: Operations of the Spaceflight Meteorology Group. *Preprints from the 13th Conference on Weather Analysis and Forecasting including Symposium on Flash Floods*. 2-6 August 1993, Vienna, VA, American Meteorological Society, Boston, MA.
- Brown, R. A., 1980: Longitudinal instabilities and secondary flows in the planetary boundary layer: a review. *Rev. Geophys. Space Phys.*, **18**, 683-697.
- Businger, S. and B. Walter, 1988: Comma cloud development and associated rapid cyclogenesis over the Gulf of Alaska: A case study using aircraft and operational data. *Mon. Wea. Rev.*, **116**, 1103-1123.
- _____, S. R. Chiswell, M. Bevis, J. Duan, C. Rocken, R. Ware, T. VanHove, and F. Solheim, 1995: The promise of GPS in atmospheric monitoring. *Bull. Amer. Meteor. Soc.*, In review.
- Byers, H. R. and H. R. Rodebush, 1948: Causes of thunderstorms of the Florida peninsula. *J. Meteor.*, **5**, 275-280.
- Chiswell, S. R., S. Businger, M. Bevis, J. Duan, C. Rocken, R. Ware, F. Solheim, and T. VanHove, 1995: Application of GPS water vapor data in analysis of severe weather. *Bull. Amer. Meteor. Soc.*, In review.
- desJardins, M. L., K. F. Brill, S. Jacobs, S. S. Schotz, P. Bruehl, 1992: GEMPAK5 Users Manual Version 5.1, NASA/GSFC, National Meteorological Center, and Unidata Program Center/UCAR. 267 pp.
- Durrant, D. and D. B. Webber, 1988: An investigation of the poleward edges of cirrus clouds associated with midlatitude jetstreams. *Mon. Wea. Rev.*, **116**, 702-714.
- Emanuel, K. A., 1994: Atmospheric Convection. Oxford University Press, New York, NY. 580 pp.
- Estoque, M. A., 1962: The sea breeze as a function of the prevailing synoptic situation. *J. Atmos. Sci.*, **19**, 24-25.
- Fitzpatrick, P. J., J. A. Knaff, C. W. Landea, and S. V. Finley, 1995: Documentation of a systematic bias in the Aviation Model's forecast of the Atlantic Tropical Upper-Tropospheric Trough: Implications for tropical cyclone forecasting. *Wea. Forecasting*, **10**, 433-446.

- Foote, G. B., 1991: Scientific Overview and Operations Plan for the Convection and Precipitation/Electrification Program, National Center for Atmospheric Research. Boulder, CO 80307, 145 pp.
- Frank, N. L., P. L. Moore and G. E. Ficher, 1967: Summer shower distribution of the Florida peninsula as deduced from digitized radar data. *J. Appl. Meteor.*, **6**, 309-316
- Gray, B.M., 1991: CaPE experiment proceeds in Florida. *Bull. Amer. Meteor. Soc.*, **72**, 1287.
- Galway, J. G., 1956: The lifted index as a predictor of latent instability. *Bull. Amer. Meteor. Soc.*, **37**, 528-529.
- Hamill, T. M., R. P. D'Entremont, and J. T. Bunting, 1992: A description of the Air Force realtime nephanalysis model. *J. Atmos. Sci.*, **41**, 2581-2594.
- Hartsough, C. S., 1992: Quality contro procedures in the Local Analysis and Prediction System (LAPS), *Preprints from the Fourth AES/CMOS Workshop: Forecasting in the Ninties*, 196-203, Whistler, British Columbia, Canada.
- Hazen, D. S., W. P. Roeder, B. F. Boyd, J. B. Lorens, and T. L. Wilde, 1995: Weather impact on launch operations at the Eastern Range and Kennedy Space Center, *Preprints to the Sixth Conference on Aviation Weather Systems*, 15-20 Jan 95, Dallas, TX, American Meteorological Society, Boston, MA.
- Houze, R. A., 1993: Cloud Dynamics. Academic Press, Inc., San Diego, CA. 573 pp.
- Kaplan, M. L., J. W. Zack, V. C. Wong, and J. J. Tuccillo, 1982: Initial results form a mesoscale atmospheric simulation system and comparisons with the AVE-SESAME I data set. *Mon. Wea. Rev.*, **110**, 1564-1590.
- Koch, S. E., M. L. desJardins, and J. P. Kocin, 1983: An interactive Barnes objective map analysis scheme for use with satellite and conventional data. *J. Climat Appl. Meteor.*, **22**, 1487-1503.
- Kocin, P. J., and L. W. Uccellini, 1990: *Snowstorms Along the Northeastern Coast of the United States: 1955 to 1985*. *Meteor. Monogr.*, **22**, No. 44, 280 pp.
- Kuo, Y.-H., Y.-R. Guo, and E. R. Westwater, 1993: Assimilation of precipitable water measurements into mesoscale numerical models. *Mon. Wea. Rev.*, **121**, 1215-1238.

- LeMone, M. A., 1973: The structure and dynamics of horizontal roll vortices in the planetary boundary layer. *J. Atmos. Sci.*, **30**, 1077-1091.
- Lilly, D. K., 1966: On the stability of Ekman boundary flow. *J. Atmos. Sci.*, **23**, 481-494.
- Lindzen, R. S., 1974: Wave-CISK in the tropics. *J. Atmos. Sci.*, **31**, 156-179.
- Manobianco, J., S. Koch, V. M. Karyampudi, and A. J. Negri, 1994: The impact of assimilating satellite-derived precipitation rates on numerical simulations of the ERICA IOP 4 cyclone. *Mon. Wea. Rev.*, **122**, 341-365.
- MESO, Inc., 1995: MASS Reference Manual Version 5.8, MESO, Inc., Troy, NY. 120 pp.
- Miller, R. C., 1975: Notes on analysis and severe storm forecasting procedures of the Air Force Global Weather Central. AFGWC Technical Report 200 (Rev), Air Weather Service (MAC), Scott Air Force Base, IL. 190 pp.
- National Oceanic and Atmospheric Administration, U. S. Department of Commerce, 1982: National Weather Service Radar Code User's Guide, Federal Meteorological Handbook No. 7, 184 pp.
- National Research Council, 1988: Meteorological Support for Space Operations: Review and Recommendations, National Research Council, Washington, DC. 77 pp.
- National Space Transportation System News Reference Manual, Volume 1 - Systems and Facilities, June 1988, 804 pp.
- Neuman, C. J., 1971: The thunderstorm forecasting system at the Kennedy Space Center. *J. Appl. Meteor.*, **10**, 921-936.
- NOAA Technical Publication Bulletin #355, 1985: NMC models and automated operations.
- Peppler, R.A., 1988: A review of static stability indices and related thermodynamic parameters. Illinois State Water Survey Miscellaneous Publication 104, Climate and Meteorology Section, Illinois State Water Survey, Champaign, IL 61820. 87 pp.
- Pielke, R., 1974: A three-dimensional numerical model of the sea breeze over south Florida. *Mon. Wea. Rev.*, **102**, 115-139.

- _____, 1975: Influence of the sea breeze on weather and man. *Weather*, **30**, 208-221.
- Roadcap, J. R. and G. V. Rao, 1993: An analytical study of the dependence of orientation and propagation of the Arabian Sea convection bands on wind shear, static stability, and preexisting convection. *Mon. Wea. Rev.*, **121**, 1656-1670.
- Reap, R. M., 1994: Analysis and prediction of lightning strike distributions associated with synoptic map types over Florida. *Mon. Wea. Rev.*, **122**, 1698-1715.
- Report of the Presidential Commission on the Space Shuttle Challenger Accident, 1986: Washington, DC.
- Scofield, R. A. and J. F. W. Purdom, 1993: The use of satellite data for mesoscale analysis and forecasting applications. Mesoscale Meteorology and Forecasting. American Meteorological Society, Boston, MA. 118-150 (793 pp.).
- Snook, J. S., 1992: Current techniques for real-time evaluation of conditional symmetric instability. *Wea Forecasting*, **7**, 430-439.
- Space Shuttle Operational Flight Rules Volume I, 1995: All Flights Mission Operations Directorate PCN-22, Lyndon B. Johnson Space Center, Houston, TX.
- Sun, W.-Y., 1978: Stability analysis of deep cloud streets. *J. Atmos. Sci.*, **35**, 466-483.
- Uccellini, L. W., and D. R. Johnson, 1979: The coupling of upper and lower tropospheric jet streaks and implications for the development of severe convective storms. *Mon. Wea. Rev.*, **107**, 682-703.
- Wakimoto, R. M. and N. T. Atkins, 1993: Observations of the sea-breeze front during CaPE. Part I: Single-Doppler, satellite, and cloud photogrammetry analysis. *Mon. Wea. Rev.*, **122**, 1092-1114.
- Wallace, J. M. and P. V. Hobbs, 1977: Atmospheric Science An Introductory Survey. Academic Press, New York, NY. 467 pp.
- Watson, A. I., R. L. Holle, R. E. Lopez, R. Ortiz, and J. R. Nicholson, 1991: Surface wind convergence as a short-term predictor of cloud-to-ground lightning at Kennedy Space Center. *Wea. Forecasting*, **6**, 49-64.

- Whitfield, M. B. and S. W. Lyons, 1992: An upper-tropospheric low over Texas during summer. *Wea. Forecasting*, **7**, 89-106.
- Williams, E. and N. Renno, 1993: An analysis of the conditional instability of the tropical atmosphere. *Mon. Wea. Rev.*, **121**, 21-36.
- Wylie, J. L., T. K. Rodgers, M. J. Papaik, E. R. Talpey, and B. L. Miller, 1993: Project Gibraltar: Fusion of GOES full disk cloud animation with high resolution earth background. *Preprints from Ninth International Conference on Interactive Information and Processing System for Meteorology, Oceanography, and Hydrology*, 88-90.
- Zack, J. W., V. M. Karyampudi, C. A. Mattocks and G. D. Coats, 1988: Meso-beta scale simulations of convective cloud systems over Florida utilizing synthetic data derived from GOES satellite imagery. *Preprints of the 8th Conference on Numerical Weather Prediction*, Baltimore, MD, American Meteorological Society, Boston. 293-300.
- Zack, J. W., C. A. Mattocks and M. D. Bousquet, 1991: A statistical-dynamical mesoscale thunderstorm forecast system for the Kennedy Space Center. *Preprints to the 9th Conference on Numerical Weather Prediction*, Denver, Colorado, American Meteorological Society, Boston, MA. 447-450.